High Order Finite Element Solution of Elastohydrodynamic Lubrication Problems

by

Hongqiang Lu

Submitted in accordance with the requirements
for the degree of Doctor of Philosophy.

The University of Leeds
School of Computing

September 2006

Abstract

In this thesis, a high-order finite element scheme, based upon the Discontinuous Galerkin (DG) method, is introduced to solve one- and two-dimensional Elastohydrodynamic Lubrication (EHL) problems (line contact and point contact). This thesis provides an introduction to elastohydrodynamic lubrication, including some history, and a description of the underlying mathematical model which is based upon a thin film approximation and a linear elastic model. Following this, typical nondimensionalizations of the equations are discussed, along with boundary conditions. Two families of problems are considered: line and point contacts. Following a review of existing numerical methods for EHL problems, a different numerical technique, known as the Discontinuous Galerkin method is described. This is motivated by the high accuracy requirement for the numerical simulation of EHL problems. This method is successfully applied to steady-state line contact problems. The free boundary is captured accurately using the moving-grid method and the penalty method respectively. Highly accurate numerical results are obtained at a low expense through the use of h-adaptivity methods based on discontinuity and high-order components respectively. Combined with the Crank-Nicolson method and other implicit schemes for the temporal discretization, highly accurate solutions are also obtained for transient line contact problems using the high order DG method for the spatial discretization. In particular, an extra pressure spike is captured, which is difficult to resolve when using low order schemes for spatial discretization. The extension of this high order DG method to the two-dimensional case (point contact) is straightforward. However, the computation in the two-dimensional case is more expensive due to the extra dimension. Hence p-multigrid is employed to improve the efficiency. Since the free boundary in the two-dimensional case is more complicated, only the penalty method is used to handle the cavitation condition. This thesis is ended with the conclusions and a discussion of future work.

Acknowledgements

I gratefully thank my two supervisors, Prof M Berzins and Prof PK Jimack. Prof M Berzins led me to this research area and has always been ready to give me advice on this research project. Many thanks to Prof PK Jimack for his guidance and support. I am very grateful for his patience and enthusiasm. Their help has made this work possible.

I would also like to thank to Dr CE Goodyer and Dr M Walkley for their valuable comments and assistance. Many thanks to all the members of the PDE group of the School of Computing for their help.

My grateful thanks to my parents who encouraged me to do research and have been supporting me throughout my life. Special thanks to my wife, Mrs Xuejun Liu, who has been always standing with me.

Declarations

Some parts of the work presented in this thesis have been published in the following articles:

Lu, H, Berzins, M and Jimack, P K, “Application of the Adaptive Discontinuous Galerkin Method to Problems in Elastohydrodynamic Lubrication”, to appear *Proceedings of the Fifth International Conference on Engineering Computational Technology, Las Palmas de Gran Canaria, Spain*, (September 2006).

Lu, H, Berzins, M, Goodyer, C E, Jimack, P K and Walkley, M A, “Adaptive High-Order Finite Element Solution of Transient Elastohydrodynamic Lubrication Problems”, *Proc. IMechE Part J: J. Engrg. Tribology*, 220 (2006) 215-225.

Lu, H, Berzins, M, Goodyer, C E and Jimack, P K, “High Order Discontinuous Galerkin Method for Elastohydrodynamic Lubrication Line Contact Problems”, *Comm. Num. Meth. Eng.*, 21 (2005) 643-650.

Contents

1 Introduction **1**

1.1 Overview . . . 1
1.1.1 Elastohydrodynamic Lubrication . . . 1
1.1.2 Outline of this Thesis . . . 4
1.2 Governing Equations . . . 5
1.2.1 Line Contact . . . 5
1.2.1.1 Dimensional Equations . . . 6
1.2.1.2 Nondimensional Equations . . . 7
1.2.2 Point Contact . . . 10
1.2.2.1 Dimensional Equations . . . 10
1.2.2.2 Nondimensional Equations . . . 10
1.3 A Brief History of the EHL problem . . . 12

2 Computational EHL Methods **14**
2.1 Numerical Methods for EHL . . . 14
2.1.1 Inverse Method . . . 14
2.1.2 Newton-Raphson Method . . . 16
2.1.3 Coupled Method . . . 16
2.1.4 Multigrid Methods . . . 19
2.1.4.1 Full Approximation Scheme . . . 19
2.1.4.2 Multilevel Multi-Integration . . . 22
2.2 Finite Difference Method . . . 25
2.3 Finite Element Method . . . 28
2.4 Conclusion . . . 33

3 Discontinuous Galerkin Method **34**
3.1 Introduction . . . 34
3.2 History of Discontinuous Galerkin . . . 34

3.3 Advantages of Discontinuous Galerkin 36
3.4 High Order and Super-Convergence 37
3.4.1 Diffusion Problems 37
3.4.2 Convection-Diffusion Problems 40
3.5 Adaptivity 42
3.6 Conclusion 44

4 DG for steady-state Line Contact 46
4.1 Introduction 46
4.2 Discretization 47
4.2.1 The Reynolds Equation 47
4.2.2 The Film Thickness Equation 49
4.2.3 The Force Balance Equation 53
4.3 Relaxation Method 53
4.4 Cavitation 58
4.4.1 Moving Boundary 59
4.4.2 Penalty Method 62
4.5 Adaptivity 63
4.5.1 H-adaptivity Based on Discontinuity 64
4.5.2 H-Adaptivity Based on High-Order Components 65
4.5.3 Data Transfer 68
4.6 Numerical Results 71
4.7 Conclusion 75

5 DG for Transient Line Contact 77
5.1 Introduction 77
5.2 Governing Equations 78
5.3 Discretization 80
5.3.1 Spatial Discretization 80
5.3.2 Temporal Discretization 80
5.4 Relaxation 82
5.5 Adaptivity 83
5.5.1 Overall Solution Procedure 84
5.6 Numerical Results 85
5.7 Conclusion 99

6 DG for Steady-State Point Contact 102

6.1 Introduction 102
6.2 Discretization 103
  6.2.1 The Reynolds Equation 103
  6.2.2 The Film Thickness Equation 107
  6.2.3 The Force Balance Equation 112
6.3 Penalty Method 112
6.4 Relaxation 113
6.5 P-multigrid 116
  6.5.1 FAS for P-multigrid 116
  6.5.2 Transfer Operators 118
6.6 Adaptivity 121
  6.6.1 Adaptive Strategy 121
  6.6.2 Data Transfer 122
6.7 Overall Solution Procedure 124
6.8 Numerical Results 125
6.9 Conclusion 135

7 Conclusion and Future Work 137

7.1 Conclusion 137
7.2 Future Work 139

Bibliography 141

List of Figures

1.1 A schematic of hydrodynamic lubrication between two cylindrical surfaces . . . 3
1.2 A schematic of elastohydrodynamic lubrication between two deformed surfaces . . . 3
1.3 Line contact, left, and point contact, right . . . 4

2.1 Restriction operators . . . 21
2.2 Prolongation operators . . . 21
2.3 V cycle for 4 grid levels . . . 22
2.4 W cycle for 4 grid levels . . . 22
2.5 Pressure profiles, left, and pressure spikes, right ($W = 2.0 \times 10^{-11}$, $U = 4.0 \times 10^{-5}$ and $G = 5000$) . . . 28
2.6 FE solution, left, and FD solution, right ($W = 2.0 \times 10^{-11}$, $U = 4.0 \times 10^{-5}$ and $G = 5000$) . . . 32
2.7 FE solution, left, and FD solution, right ($U = 1.0 \times 10^{-11}$, $W = 1.0 \times 10^{-4}$ and $G = 5000$) . . . 33

3.1 L^2-norm of the error when solving the diffusion problem using high-order DG with uniform meshes . . . 41
3.2 L^2-norm of the error when solving the convection problem using high-order DG . . . 43
3.3 L^2-norm of the error when solving the convection-diffusion problem using high-order DG . . . 43

4.1 One-dimensional basis functions when $p = 5$ . . . 48
4.2 Coordinate mapping between the reference element and the local element e 51
4.3 Possible pressure profiles on the rightmost element . . . 60
4.4 Desired pressure profile on the rightmost element . . . 60

4.5 Initial pressure distribution based upon a linear interpolant of the Hertz dry contact profile. 62
4.6 Refinement and coarsening 64
4.7 History of the h-adaptivity based on the discontinuities in the spike region when $U = 1.0 \times 10^{-11}$, $W = 1.0 \times 10^{-4}$ and $G = 5000$ 66
4.8 Data transfer between grids 68
4.9 Pressure distributions obtained using DG and FD methods across the entire contact, left, and around the pressure spike, right 71
4.10 Initial guess for pressure, left, and the resulting pressure profile, right . . 73
4.11 Comparison of the cavitation boundaries obtained using the moving-grid method and the penalty method 73
4.12 Comparison of the cavitation boundaries obtained using the moving-grid method and the refined penalty method 74
4.13 Pressure profile when $p = 6$, left, and pressure profile when $p = 12$, right 74
4.14 Pressure profile when $p = 12$, $U = 1.0 \times 10^{-11}$, $W = 1.0 \times 10^{-4}$ and $G = 5000$, left, and pressure profile when $p = 12$, $U = 2.0 \times 10^{-11}$, $W = 4.0 \times 10^{-5}$ and $G = 5000$, right 75

5.1 H-adaptivity 84
5.2 Non-dimensional pressure and film thickness when X_d = -2.0 86
5.3 Non-dimensional P and H obtained using the DG simulation for the first transient problem 88
5.4 Comparison of the fine details of the pressure computed via the new Discontinuous Galerkin (DG) method and using the standard multilevel Finite Difference (FD) solver on a mesh of 1025 points 89
5.5 Non-dimensional P and H obtained using the DG simulation for the second transient test problem 92
5.6 Some fine details of the pressure computed using the new Discontinuous Galerkin (DG) method 93
5.7 Pressure profile when $X_d = 1.0$ for the second transient test problem . . . 94
5.8 Comparison of the pressure profiles obtained using different θ and $\triangle T$. 0, initial guess. 1, $\theta = 0.5$ and $\triangle T = 0.0001$. 2, $\theta = 0.45$ and $\triangle T = 0.0001$. 3, $\theta = 0.25$ and $\triangle T = 0.0001$. 4, $\theta = 0.0$ and $\triangle T = 0.0001$. 5, $\theta = 0.5$ and $\triangle T = 0.001$. 6, $\theta = 0.45$ and $\triangle T = 0.001$. 7, $\theta = 0.25$ and $\triangle T = 0.001$. 8, $\theta = 0.0$ and $\triangle T = 0.001$. 95

5.9 Non-dimensional P and H obtained for the first roughness model but with different spatial degree and different time-stepping to the results in Figure 5.3 96
5.10 Three roughness models 97
5.11 Non-dimensional P and H obtained using the DG simulation with “Roughness 3” 98
5.12 Non-dimensional P and H obtained using the DG simulation with “Roughness 4” 100

6.1 Computational domain used for the DG discretization of equations ((1.20), (1.21) and (1.22)) 104
6.2 Nodal modes for the hierarchical basis 105
6.3 Side modes for the hierarchical basis 105
6.4 Internal modes for the hierarchical basis 106
6.5 Coordinate mapping between the reference element and the local element e 109
6.6 Singular quadrature is used when $(x,y) \in e$ 110
6.7 Two-dimensional singular quadrature 111
6.8 Singular quadrature is used to calculate $K_i^e(x,y)$ and $K_i^f(x,y)$ when $(x,y) \in \Gamma_{ef}$ 111
6.9 A simple adaptive grid 113
6.10 Four level V-cycles for p-multigrid 118
6.11 H-adaptivity in two dimensions 122
6.12 Initial grid 127
6.13 Initial pressure profile 127
6.14 Final grid (a): $W = 0.2 \times 10^{-7}$, $U = 0.1 \times 10^{-11}$ and $G = 5000$ 128
6.15 Converged pressure profile (a): $W = 0.2 \times 10^{-7}$, $U = 0.1 \times 10^{-11}$ and $G = 5000$ 128
6.16 Converged pressure profile (a): $W = 0.2 \times 10^{-7}$, $U = 0.1 \times 10^{-11}$ and $G = 5000$ 129
6.17 Final grid (b): $W = 0.5 \times 10^{-7}$, $U = 0.2 \times 10^{-11}$ and $G = 5000$ 129
6.18 Converged pressure profile (b): $W = 0.5 \times 10^{-7}$, $U = 0.2 \times 10^{-11}$ and $G = 5000$ 130
6.19 Converged pressure profile (b): $W = 0.5 \times 10^{-7}$, $U = 0.2 \times 10^{-11}$ and $G = 5000$ 130
6.20 Final grid (c): $W = 0.6 \times 10^{-7}$, $U = 0.2 \times 10^{-11}$ and $G = 5000$ 131

6.21 Converged pressure profile (c): $W = 0.6 \times 10^{-7}$, $U = 0.2 \times 10^{-11}$ and $G = 5000$ 131

6.22 Converged pressure profile (c): $W = 0.6 \times 10^{-7}$, $U = 0.2 \times 10^{-11}$ and $G = 5000$ 132

6.23 Final grid (d): $W = 0.7 \times 10^{-7}$, $U = 0.3 \times 10^{-11}$ and $G = 5000$ 132

6.24 Converged pressure profile (d): $W = 0.7 \times 10^{-7}$, $U = 0.3 \times 10^{-11}$ and $G = 5000$ 133

6.25 Converged pressure profile (d): $W = 0.7 \times 10^{-7}$, $U = 0.3 \times 10^{-11}$ and $G = 5000$ 133

6.26 Final grid when $Tol_{penalty} = 0.05$ (a): $W = 0.2 \times 10^{-7}$, $U = 0.1 \times 10^{-11}$ and $G = 5000$ 134

6.27 Final grid when $Tol_{penalty} = 0.001$ (a): $W = 0.2 \times 10^{-7}$, $U = 0.1 \times 10^{-11}$ and $G = 5000$ 135

List of Tables

4.1 Values of u_e^i . . . 67

4.2 Comparison of Pressure Peak Position and Free Boundary Values . . . 72

4.3 Comparison of Pressure Peak Position and Free Boundary Values . . . 73

4.4 Comparison of Pressure Peak Position and Peak Pressure when using different orders . . . 74

4.5 Results obtained using the second h-adaptivity method when $p = 12$ . . . 75

5.1 Comparison of friction at particular times . . . 88

6.1 Comparison of Pressure Peak Position and Peak Pressure . . . 126

6.2 Comparison of Pressure Peak Position and Peak Pressure . . . 134

Chapter 1

Introduction

1.1 Overview

In this chapter, a brief introduction to Elastohydrodynamic Lubrication problems and the outline of this thesis are given. The dimensional and non-dimensional governing equations of line contact (1d) and point contact problems (2d) are also described.

1.1.1 Elastohydrodynamic Lubrication

In everyday life, friction exists everywhere, and in many respects it is an essential force. For example, it makes cars both run and stop. However, sometimes friction is not welcome. For example, it can cause power loss in engines and reduce the lifetime of contacting elements (due to wear). In these situations, friction is required to be minimized. The most common way to reduce friction and prevent wear is through lubrication, for which lubricants are used to separate contacting surfaces. Friction can be reduced to a small fraction of the unlubricated case. The efficiency of the components will therefore be significantly enhanced and the lifetime of the machine elements will also be dramatically extended.

Since lubrication is such an effective way to reduce power loss and prevent wear, and since the behaviour of the lubricant film between contacting elements is of great importance in determing its performance, understanding this behaviour is of great interest to researchers. In many cases, the film thickness is determined exclusively by the shapes of the contacting surfaces. This situation is called hydrodynamic lubrication, which is illustrated in Figure 1.1 where the lubricant flows from left to right. However, when the pressure is sufficiently high, compared to the stiffness of the running surfaces, the elastic deformation of the contacting surfaces can not be ignored, and this can heavily affect the shape of the lubricant film. The lubrication of such, more complicated, situations is referred to as *Elastohydrodynamic Lubrication* (EHL), which is shown in Figure 1.2.

The EHL problem is not only characterized by the interaction between the film thickness and the elastic deformation. At such high pressures, the lubricant viscosity also depends heavily on pressure and the lubricant is compressible. A very interesting feature of the flow is a steep pressure spike that appears in the outlet region at high loads. Both the shape and the position of the spike vary with the load case. The spike is a physical property that is smoothly varying, despite being very steep. Another important characteristic element of EHL is the outlet free boundary (or cavitation position) where the pressure of the lubricant becomes equal to the vapour pressure (conventionally taken to be zero). All of these facts increase the complexity of EHL problems, as compared to hydrodynamic lubrication problems for example. For a typical EHL contact problem, the desired information includes the pressure profile, the film thickness profile and the cavitation position.

Elastohydrodynamic lubrication often happens when a large pressure is applied over a very small surface area, such as in journal bearings and gears, but the EHL theory is not restricted just to very highly loaded cases. It is applicable to all situations where the interaction between the elastic deformation of the contacting elements and the lubricant film formation can not be neglected. With such a large range of loaded cases, it is expensive to investigate all possible lubricated contacts by physical experiments. Furthermore, at high loads the film thickness is usually very thin, the pressure in the contact region is extremely high and the lubricant passes through the contact in as little as a hundredth of a second. All of these facts make it difficult to undertake measurement through physical experiments. With the increase of computational ability in recent years, numerical simulation has been widely used to study the behaviour of EHL contacts.

A contact between a paraboloid and a flat surface is often used to undertake EHL theoretical analysis since the film thickness and the contact region are generally quite small compared to the local radius of curvature of the contacting surfaces. According to the dimension of the contact, EHL problems are divided into two types: the line contact problem (1d) and the point contact problem (2d) [25]. Figure 1.3 shows the reduced geometry employed in the these two theoretical analyses, where

R, R_x and R_y are the radii of curvature,

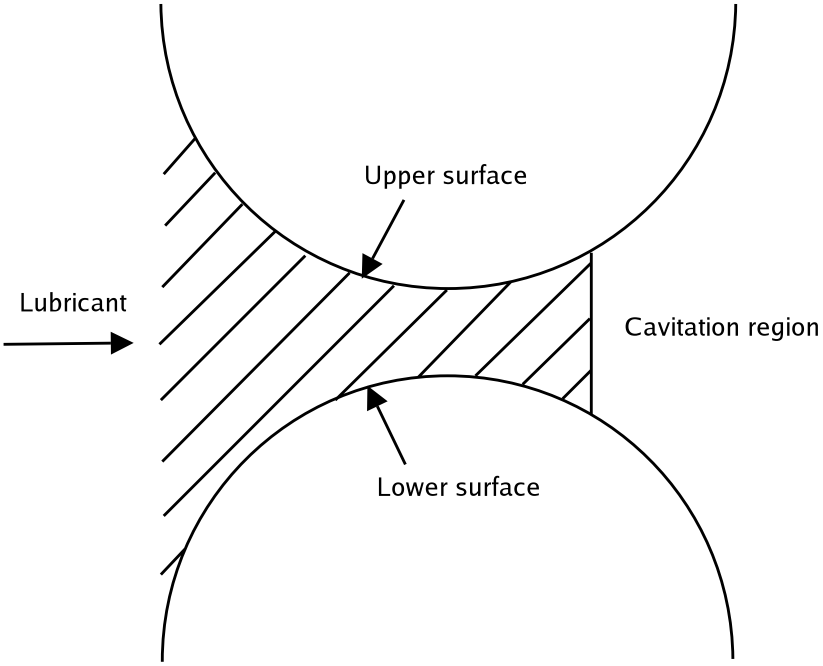

Figure 1.1: A schematic of hydrodynamic lubrication between two cylindrical surfaces

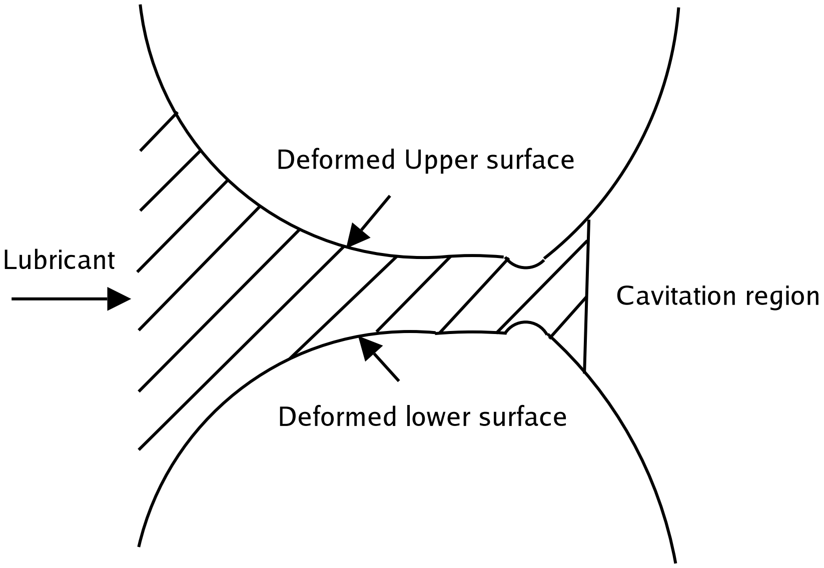

Figure 1.2: A schematic of elastohydrodynamic lubrication between two deformed surfaces

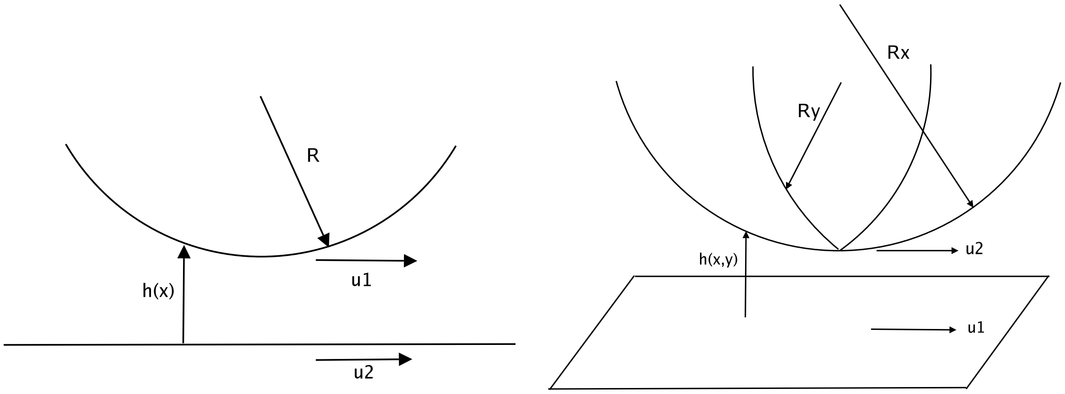

Figure 1.3: Line contact, left, and point contact, right

$h(x)$ and $h(x,y)$ are the film thickness,

U_1 and U_2 are the velocities of the upper surface and the lower surface respectively.

1.1.2 Outline of this Thesis

In this thesis, a high order Discontinuous Galerkin (DG) method is used to solve EHL problems. To the author's knowledge this is the first time that DG has been applied to this problem and the method is found to be both stable and accurate across a wide range of loads. Furthermore, DG is shown to permit accurate solutions using just a small number of degrees of freedom provided suitable grids are used. The pressure spike and the cavitation position can be captured more accurately than with alternative, lower order, methods.

In the following sections of this chapter, the governing equations [60] for the line and point contact problems are introduced and then a brief introduction to the history of the EHL problem is given. Chapter 2 describes the most widely used numerical methods for the solution of EHL problems. An overview of the development of finite difference and continuous finite element methods are given. The Discontinuous Galerkin method is briefly introduced in Chapter 3. The detailed description of the application of high order DG to EHL problems starts in Chapter 4. The high order DG discretization of the line contact governing equations is first described. A nonlinear smoother is then developed to solve the highly nonlinear discrete algebraic system and an h-adaptive method is used to obtain appropriately spaced grids for differently loaded cases. In this 1-d case, two different methods (a free boundary approach and a penalty method) are used to handle the cavitation condition. Chapter 4 ends by presenting a comparison between results obtained using high order DG and those from conventional finite differences in order to demonstrate excellent accuracy for highly loaded line contact problems. In order to further demonstrate the high accuracy of the proposed method, a typical transient line contact problem is described and solved in Chapter 5. This leads to some very interesting numerical results in which some new details of the pressure profile are captured. In Chapter 6, the high order DG method is applied to point contact problems. The h-adaptivity method used in 1d is extended to 2d. In this case only the penalty method is adopted to capture the outlet free boundary and the work so far is restricted to steady-state examples. In order to accelerate the convergence, the p-multigrid method is applied to point contact problems in Chapter 7. Chapter 8 summarizes the contribution of this thesis and presents a discussion of future work that should be undertaken.

1.2 Governing Equations

The isothermal EHL contact can be described using two groups of equations. One group of equations describes the physical properties of the lubricant and the other is concerned with the EHL problem itself. The second group of equations consists of three equations:

- The Reynolds equation. This describes the flow of a Newtonian fluid between contacting elements. The Reynolds equation is derived from the Navier-Stokes equations [52]. Assuming a narrow gap and a Newtonian lubricant behaviour, the Navier-Stokes equations can be significantly simplified, from which the velocities in the flow can be solved. Substitution of the velocities in the equation of continuity yields an equation for pressure in the lubricant film, which is referred to as the Reynolds equation.

- The film thickness equation. This gives the shape of the lubricant film which includes the elastic deformation given a pressure distribution.

- The force balance equation. This describes the fact that the lubricant should balance the applied load.

In the following sections, the detailed line contact equations and point contact equations will be given respectively.

1.2.1 Line Contact

For the line contact problem, the contacting elements are assumed to be infinite in the y direction. As a result, it becomes a one-dimensional problem.

1.2.1.1 Dimensional Equations

The line contact Reynolds equation reads:

$$\frac{\partial}{\partial x}\left(\frac{\rho h^3}{\eta}\frac{\partial p}{\partial x}\right) - 6u_s\frac{\partial(\rho h)}{\partial x} - 12\frac{\partial(\rho h)}{\partial t} = 0, \tag{1.1}$$

where

p is the pressure,

h is the film thickness,

ρ is the density of the lubricant,

η is the viscosity of the lubricant,

$u_s = u_1 + u_2$ is the sum velocity, where u_1 and u_2 are the velocities of the upper surface and the lower surface respectively.

Given a pressure distribution, the film thickness can be calculated according to the film thickness equation:

$$h(x) = h_{00} + \frac{x^2}{2R} - \frac{4}{\pi E'}\int_{-\infty}^{\infty} ln\left|\frac{(x-x^{'})}{x_0}\right| p(x^{'})\,\mathrm{d}x^{'}, \tag{1.2}$$

where

h_{00} is the central offset film thickness,

R is the reduced radius of curvature: $R^{-1} = R_1^{-1} + R_2^{-1}$ where R_1 and R_2 are the curvatures of the upper surface and the lower surface respectively,

$E^{'}$ is the reduced elastic modulus of the contact.

Note that the global integral in equation (1.2) describes the elastic deformation at a single point and it depends on the entire pressure distribution.

Since the lubricant film separates the contacting elements, the integral over the pressure must be equal to the applied load. This leads to the force balance equation:

$$\int_{-\infty}^{\infty} p(x)\,\mathrm{d}x = w, \tag{1.3}$$

where w is the external load per unit width.

Since the pressure in the lubricant varies rapidly over a small distance, changes of the physical properties of the lubricant, such as density and viscosity, have to be considered. The other group of equations modelling the lubricant must also be defined therefore. First the lubricant needs to be considered as compressible since the pressure is usually very high. The following density-pressure relation proposed by Dowson and Higginson [16] is used in this thesis:

$$\rho(p) = \rho_0 \frac{0.59 \times 10^9 + 1.34p}{0.59 \times 10^9 + p}, \tag{1.4}$$

where ρ_0 is the density at ambient pressure. The viscosity is the other important property of the lubricant, which increases rapidly with increasing pressure. Barus' equation [2] is widely used to describe the viscosity-pressure relation:

$$\eta(p) = \eta_0 e^{\alpha p}, \tag{1.5}$$

where

η_0 is the viscosity at ambient pressure,

α is the pressure-viscosity coefficient, typically $\alpha \approx 2 \times 10^{-8}$.

However Barus' equation is only accurate for relatively low pressure. A more accurate viscosity-pressure relation was introduced by Roelands [54]:

$$\eta(p) = \eta_0 e^{\left\{ \frac{\alpha p_0}{z} \left[-1 + \left(1 + \frac{p}{p_0} \right)^z \right] \right\}}, \tag{1.6}$$

where

z is pressure viscosity index, typically $0.5 \leq z \leq 0.7$,

p_0 is a constant: $p_0 = 1.98 \times 10^8$.

The relation (1.6) is assumed throughout this thesis.

1.2.1.2 Nondimensional Equations

Since the magnitude of the variables varies a lot (up to $\mathscr{O}(10^9)$ Pa for the pressure and down to $\mathscr{O}(10^{-8})$ metres for the film thickness), nondimensionalization has to be performed. This is based on the Hertzian dry contact parameters [60]. In the one-dimensional case (line contact), the Hertzian pressure profile is:

$$p(x) = \begin{cases} p_h \sqrt{1 - \left(\frac{x}{b}\right)^2} & \text{if } x < b \\ 0 & \text{otherwise} \end{cases},$$

where p_h refers to the maximum Hertzian pressure:

$$p_h = \frac{2w}{\pi b} \tag{1.7}$$

and b is the half width of the Hertzian contact:

$$b = \sqrt{\frac{8wR}{\pi E'}}. \tag{1.8}$$

By substituting the following dimensionless variables into the dimensional Reynolds equation:

$$\begin{aligned}
\bar{\rho} &= \rho/\rho_0, \\
\bar{\eta} &= \eta/\eta_0, \\
X &= x/b, \\
P &= p/p_h, \\
H &= hR/b^2, \\
T &= tu_s/(2b),
\end{aligned}$$

the non-dimensional Reynolds equation is obtained as follows:

$$\frac{\partial}{\partial X}\left(\varepsilon \frac{\partial P}{\partial X}\right) - \frac{\partial(\bar{\rho}H)}{\partial X} - \frac{\partial(\bar{\rho}H)}{\partial T} = 0, \tag{1.9}$$

where

$$\varepsilon = \frac{\bar{\rho}H^3}{\bar{\eta}\lambda}, \tag{1.10}$$

$P(X)$ and $H(X)$ are the dimensionless pressure and film thickness, $\bar{\rho}(P)$ and $\bar{\eta}(P)$ are the dimensionless density and viscosity, and λ is a dimensionless speed parameter. Neglecting the time-dependent term yields the steady-state non-dimensional Reynolds equation:

$$\frac{\partial}{\partial X}\left(\varepsilon \frac{\partial P}{\partial X}\right) - \frac{\partial(\bar{\rho}H)}{\partial X} = 0. \tag{1.11}$$

The nondimensionalized film thickness equation reads:

$$H(X) = H_{00} + \frac{X^2}{2} - \frac{1}{\pi}\int_{-\infty}^{\infty} \ln\left|X - X'\right| P(X')\,\mathrm{d}X', \tag{1.12}$$

where H_{00} is the dimensionless central offset film thickness and the integral describes the elastic deformation.

The dimensionless force balance equation is given by:

$$\int_{-\infty}^{\infty} P(X)\,\mathrm{d}X - \frac{\pi}{2} = 0. \tag{1.13}$$

The viscosity and the density equations are also written in the following dimensionless forms:

$$\bar{\eta}(P) = e^{\left\{\frac{\alpha p_0}{z}\left[-1+\left(1+\frac{Pp_h}{p_0}\right)^z\right]\right\}}, \tag{1.14}$$

and

$$\bar{\rho}(P) = \frac{0.59 \times 10^9 + 1.34Pp_h}{0.59 \times 10^9 + Pp_h}. \tag{1.15}$$

For physical reasons, all pressures should be larger than or equal to the vapour pressure of the lubricant (taken to be zero for simplicity). This is not accounted for in the Reynolds equation, hence, in the outlet region, the calculated solution may have negative pressures. Consequently the Reynolds equation is only valid in the pressurised region and the cavitation position, X_{cav}, is therefore treated as a free boundary. Furthermore, in order to ensure that the model domain is finite the inlet boundary is fixed at a position X_{in}, that is sufficiently far from the contact region not to affect the nature of the flow. With this finite domain the associated boundary conditions are:

$$P(X_{in}) = 0, \quad P(X_{cav}) = 0 \quad \text{and} \quad \frac{\partial P}{\partial X}(X_{cav}) = 0. \tag{1.16}$$

Dowson and Higginson [16] introduced a set of three dimensionless parameters to characterize each loaded case in 1d:

$$\begin{aligned} W &= \frac{w}{E'R} && (1.17)\\ G &= \alpha E' && (1.18)\\ U &= \frac{1}{2}\frac{\eta_0 u_s}{E'R}. && (1.19) \end{aligned}$$

In this thesis, these three parameters are used to describe our loaded cases.

1.2.2 Point Contact

1.2.2.1 Dimensional Equations

The point contact problem also consists of three equations. In dimensional form the two-dimensional Reynolds equation reads:

$$\frac{\partial}{\partial x}\left(\frac{\rho h^3}{\eta}\frac{\partial p}{\partial x}\right)+\frac{\partial}{\partial y}\left(\frac{\rho h^3}{\eta}\frac{\partial p}{\partial y}\right)-6u_s\frac{\partial(\rho h)}{\partial x}-12\frac{\partial(\rho h)}{\partial t}=0. \tag{1.20}$$

The film thickness equation is given by:

$$h(x,y)=h_{00}+\frac{x^2}{2R_x}+\frac{y^2}{2R_y}+\frac{2}{\pi E'}\int_{-\infty}^{\infty}\int_{-\infty}^{\infty}\frac{p(x',y')\mathrm{d}x'\mathrm{d}y'}{\sqrt{(x-x')^2+(y-y')^2}}. \tag{1.21}$$

The two-dimensional force balance equation also balances the applied load:

$$\int_{-\infty}^{\infty}\int_{-\infty}^{\infty}p(x,y)\,\mathrm{d}x\mathrm{d}y=F, \tag{1.22}$$

where F is the external load.

1.2.2.2 Nondimensional Equations

Similar to the line contact problem, the above equations can be nondimensionalized using the two-dimensional Hertzian dry contact parameters [60]. In the two-dimensional case, the Hertzian pressure profile is given by:

$$p(x,y)=\begin{cases} p_h\sqrt{1-\left(\frac{x}{a}\right)^2-\left(\frac{y}{a}\right)^2} & \text{if } \left|x^2+y^2\right|<a^2 \\ 0 & \text{otherwise}\end{cases},$$

where p_h refers to the maximum Hertzian pressure:

$$p_h=\frac{3F}{2\pi a^2} \tag{1.23}$$

and a is the radius of the contact circle:

$$a^2=\frac{3FR_x}{2E'}, \tag{1.24}$$

where R_x is the reduced radius of curvature in x direction ($R_x = R_y$ for a circular contact assumed here) and E' is the reduced elastic modulus of the contacting bodies.

Using the following dimensionless variables:

$$
\begin{aligned}
\bar{\rho} &= \rho/\rho_0, \\
\bar{\eta} &= \eta/\eta_0, \\
X &= x/a, \\
Y &= y/a, \\
P &= p/p_h, \\
H &= hR/a^2, \\
T &= tu_s/(2a),
\end{aligned}
$$

dimensionless equations can be obtained. The dimensionless Reynolds equation reads:

$$
\frac{\partial}{\partial X}\left(\varepsilon \frac{\partial P}{\partial X}\right) + \frac{\partial}{\partial Y}\left(\varepsilon \frac{\partial P}{\partial Y}\right) - \frac{\partial(\bar{\rho} H)}{\partial X} - \frac{\partial(\bar{\rho} H)}{\partial T} = 0, \tag{1.25}
$$

where $\varepsilon = \frac{\bar{\rho} H^3}{\eta \lambda}$. The steady-state 2d dimensionless Reynolds equation is obtained by neglecting the time-dependent term:

$$
\frac{\partial}{\partial X}\left(\varepsilon \frac{\partial P}{\partial X}\right) + \frac{\partial}{\partial Y}\left(\varepsilon \frac{\partial P}{\partial Y}\right) - \frac{\partial(\bar{\rho} H)}{\partial X} = 0. \tag{1.26}
$$

The film thickness is given by:

$$
H(X,Y) = H_{00} + \frac{X^2}{2} + \frac{Y^2}{2} + \frac{2}{\pi} \int_{-\infty}^{\infty} \int_{-\infty}^{\infty} \frac{P(X^{'},Y^{'})}{\sqrt{(X-X^{'})^2 + (Y-Y^{'})^2}} \mathrm{d}X^{'} \mathrm{d}Y^{'}, \tag{1.27}
$$

where H_{00} is the central offset film thickness. The two parabolic terms define the undeformed shape of the surface and the elastic deformation is also a global integral. The applied force is balanced in the following way:

$$
\int_{-\infty}^{\infty} \int_{-\infty}^{\infty} P(X,Y)\, dX^{'} dY^{'} - \frac{2\pi}{3} = 0. \tag{1.28}
$$

For point contacts we may still use the viscosity-pressure relationship of Roelands [54]:

$$
\bar{\eta}(P) = e^{\left\{ \frac{\alpha p_0}{z} \left[-1 + \left(1 + \frac{P p_h}{p_0}\right)^z \right] \right\}}, \tag{1.29}
$$

and the density model of Dowson and Higgison is employed to describe the compressibility of the lubricant [16]:

$$\bar{\rho}(P) = \frac{0.59 \times 10^9 + 1.34 P p_h}{0.59 \times 10^9 + P p_h}. \tag{1.30}$$

Similar to the 1D case, the inlet boundary of the computational domain X_{in} is located far from the contact centre. The outlet cavitation boundary is more complicated since it is a curve on which $P(X_{cav}) = 0$ and $\frac{\partial P}{\partial n}(X_{cav}) = 0$ where n is the unit outward normal.

In the 2d case, Hamrock and Dowson [30] introduced the following set of dimensionless parameters to describe a circular loaded case:

$$W = \frac{w}{E' R_x^2} \tag{1.31}$$

$$G = \alpha E^{'} \tag{1.32}$$

$$U = \frac{1}{2} \frac{\eta_0 u_s}{E' R}. \tag{1.33}$$

1.3 History of the EHL problem

Following Tower's (1883) experimental investigation of friction in lubricated journal bearings, Osborne Reynolds (1886) [52] established the foundations of fluid film lubrication theory, now known as "The Reynolds Equation". The application of Reynolds' theory to journal and thrust bearings was successful. In 1916 Martin [43] solved the Reynolds equation for gear lubrication, assuming the contacting surfaces to be rigid and the lubricant to be isoviscous. But the predicted film thicknesses were much smaller than the surface roughness. There had not been any significant progress before Ertel (1939) [19] and Grubin (1949) [28] took account of both elastic deformation and pressure-viscosity effects. The predicted thicknesses in the central region were more than one order larger than Martin's results and much larger than the surface roughness, which indicates the great importance of the elastic deformation and the pressure-viscosity effects.

In 1951, Petrusevich [50] obtained the first numerical solution of the line contact problem which simultaneously satisfied both the Reynolds equation and the film thickness equation. In his results, the second maximum in the pressure profile was first obtained, which now is referred to as "the Petrusevich spike" or "the pressure spike", and a corresponding dip in film thickness was also observed. These are regarded as the two major features of EHL solutions. Following this, numerous researchers devoted attention to developing numerical methods to solve EHL problems. In 1959, Dowson and Higginson [15] introduced the inverse method which is mainly suitable for highly loaded cases.

Evans and Snidle [22, 23] extended the inverse approach to point contact problems. Okamura introduced the Newton-Raphson algorithm [47] which is based on the linearization of the system of equations around some approximate solution. Further improvements were made by Houpert and Hamrock [33] and Chang [9]. Another simple forward algorithm, Gauss-Seidel relaxation, was used by Hamrock and Dowson [29, 31] for both line contact and point contact. Unfortunately, both the Newton-Raphson and the Gauss-Seidel relaxation schemes are not sufficiently stable because of the high nonlinearity of EHL problems, particularly for highly loaded cases. To improve the relaxation stability, Elcoate et al. [17] coupled the Reynolds equation and the film thickness equation together and solved for the pressure and the thickness simultaneously. To improve the efficiency, the differential deflection method [21] was then introduced. In order to accelerate convergence the multigrid method, based on Gauss-Seidel relaxation, was first employed by Lubrecht in 1986 [42]. For the fast calculation of the elastic deformation Brandt and Lubrecht [7] developed a multilevel multi-integration algorithm which significantly reduces the computational complexity in approximating deformations at each point in the contact. Venner [60, 61] contributed further improvements on relaxation robustness. Based on the above achievements, the finite difference method combined with multigrid has become the most popular method for EHL problems since it is both efficient and stable. For many problems the coupled scheme combined with the differential deflection formulation is also very competitive. For compressible EHL problems, most of the methods mentioned above are based on finite difference discretization. As an alternative to finite differences, continuous finite element methods were also used to solve incompressible EHL problems [1, 34, 35, 44, 46, 55, 59, 64]. However, for stability reasons, it is not straightforward to apply continuous finite element methods to compressible EHL problems. Most of these approaches are described in the following chapter.

Chapter 2

Computational EHL Methods

In this chapter, various existing numerical methods developed for EHL problems are discussed. For simplicity, we only focus on steady-state line contact problems. We will also give an introduction to our implementation of the “finite difference+multigrid” method [60, 63] and a simple upwind linear finite element method [48].

2.1 Numerical Methods for EHL

Over the last few decades, many numerical methods have been developed to solve EHL problems. During several early attempts [15, 29], people found that it is difficult to solve highly loaded cases. As research progressed, people began to focus on developing robust numerical methods such as those described in this section.

2.1.1 Inverse Method

In highly loaded cases, ε in (1.10) varies several orders of magnitude over the computational domain because of the elastic deformation and the viscosity-pressure relation (1.6). Outside the contact region ε is very large, hence the diffusion term dominates and the Reynolds equation (1.11) behaves like an elliptic equation with respect to pressure. In the contact region, where ε is very small, the convection term of the Reynolds equation dominates and the Reynolds equation looks more like a hyperbolic equation with respect to film thickness. With the inverse method [15, 22, 23], the Reynolds equation is used to calculate the film thickness (hydrodynamic film thickness) in this region where the convection term dominates. Based on the difference between the hydrodynamic film thickness and the film thickness calculated from the film thickness equation, the approximation of the pressure profile is corrected. Outside the contact region, the Reynolds equation is usually used to calculate the pressure directly. The overall iterative procedure for this combined direct-inverse method therefore proceeds as follows for a line contact problem:

1. Give initial pressure distribution P_s.
2. Calculate the elastic film thickness H_e from the elasticity equation (1.2).
3. Calculate the hydrodynamic film thickness H_{hydro} from the Reynolds equation (1.9).
4. In the contact region, calculate the inverse pressure P_{inv} according to the difference between H_e and H_{hydro}.
5. Outside the contact region, calculate the hydrodynamic pressure P_{hydro} from the Reynolds equation.
6. Relax P_s towards P_{inv} and P_{hydro} in the contact region and the noncontact region respectively.
7. Repeat from 2. until convergence.

The inverse method is very suitable for highly loaded cases and many successful highly loaded results have been presented [15,22,23]. However, there are some significant drawbacks.

1. The inverse method is only suitable for highly loaded cases. That is why it is only employed in the contact region.
2. The application of the inverse method to rough contact problems may be difficult because the inverse pressure is calculated based on the difference between the hydrodynamic film thickness and the elastic film thickness which is not sensitive to any local change in pressure.
3. A very good initial guess is generally required to obtain convergence.
4. The robustness of the overall combined direct-inverse relaxation is relatively sensitive to the choice made for the position of the high-low pressure boundary.

2.1.2 Newton-Raphson Method

A well-known method for the solution of nonlinear systems of algebraic equations is the Newton-Raphson approach. The discretization of the Reynolds equation may be linearized and the resulting Jacobian matrix, which consists of the derivatives of all discrete equations with respect to all variables, is used to update the solution. The values of film thickness included in the Reynolds equation are evaluated from the film thickness equation using the current pressure. One significant advantage is that it is maybe possible to obtain a converged solution quickly if the initial guess is good enough. But two major drawbacks have limited the application of the Newton-Raphson method to *EHL* problems.

1. With increasing load, the Jacobian matrix tends to become closer and closer to singular, which can make the relaxation fail [55].

2. The other major difficulty comes in the implementation of the cavitation condition since all pressures are updated simultaneously in each sweep. In the 1D case, the cavitation position may be treated as a single additional unknown. However in the 2D case the free boundary is more complicated, which prevents the application of this method to point contact problems since the free boundary can not easily be defined to be an unknown or set of unknowns.

2.1.3 Coupled Method

A very important feature of any *EHL* problem is that the elastic deformation is a global integral which has limited sensitivity to local changes in pressure. This fact makes the Reynolds equation so highly nonlinear that normal relaxation methods do not work in highly loaded cases. Based on this feature, a coupled method was introduced to improve the relaxation robustness [17, 36, 37, 47].

The discrete 1d steady-state Reynolds equation can be represented by the matrix equation:

$$[A]\{P_i\} = \{0\} - [B]\{H_i\}, \tag{2.1}$$

where the square brackets represent an $n \times n$ square matrix and curly brackets represent vectors of length n. The entries P_i and H_i are the values of the pressure and the film thickness at the ith node. Entries of A are the coefficients of nodal pressure in the discrete Reynolds equation and entries of B are the coefficients of the nodal film thickness. Both A and B are banded and the bandwidth depends on the discretization.

The film thickness equation can be written as follows [60]:

$$\begin{aligned} H_i &= \hat{H}_i + D(X_i) \\ &= \hat{H}_i + \sum_{k=1}^{n} g_{k-i} P_k, \end{aligned} \tag{2.2}$$

where $D(X_i)$ represents the elastic deformation at the ith node and

$$\hat{H}_i = H_{00} + \frac{X^2}{2}, \tag{2.3}$$

and

$$\begin{aligned} g_{k-i} &= \left(k-i+\frac{1}{2}\right) h \left(ln \left(\left| k-i+\frac{1}{2} \right| h \right) - 1 \right) \\ &- \left(k-i-\frac{1}{2}\right) h \left(ln \left(\left| k-i-\frac{1}{2} \right| h \right) - 1 \right). \end{aligned} \tag{2.4}$$

Equation (2.2) can also be written in matrix form:

$$\{H_i\} = \{\hat{H}_i\} - [F]\{P_i\}, \tag{2.5}$$

where $[F]$ is a square full $n \times n$ matrix.

Combining equation (2.1) and (2.5) yields the following system:

$$\begin{bmatrix} A & B \\ F & E \end{bmatrix}_{ij} \begin{Bmatrix} P_j \\ H_j \end{Bmatrix} = \begin{Bmatrix} 0 \\ \hat{H} \end{Bmatrix}_i \tag{2.6}$$

where the submatrices A and B are banded, F is full and E is the identity matrix.

Instead of calculating the film thickness from the film thickness equation after solving the pressure from the Reynolds equation, the discrete Reynolds equation and the discrete film thickness equation are coupled into one discrete system and both the pressure and the film thickness are treated as active variables and updated simultaneously. The system is solved by elimination, starting at the inlet boundary and working downstream, followed by back substitution. The free outlet boundary is initially located at the downstream limit. During the back substitution, the free boundary is moved to the point where the next upstream node has a negative pressure.

In order to simplify the resulting discrete system, the *Differential Deflection* method [21] was introduced. The second derivative of the deflection at any mesh point is given by:

$$\frac{d^2D(X_i)}{dX^2} = \frac{4}{\pi E'}\sum_{k=1}^{n} f_{k-i}P_k, \tag{2.7}$$

where

$$f_{k-i} = F^{(-)}_{k-i+1} + F_{k-i} + F^{(+)}_{k-i-1} \tag{2.8}$$

with

$$\begin{aligned}
F^{-}_{m} &= \frac{1}{2h}\left[\frac{8m^2+4m-1}{4m^2-1} - (2m+1)ln\left(\frac{2m+1}{2m-1}\right)\right], m \neq 0 && (2.9)\\
F_{m} &= \frac{1}{2h}\left[\frac{10-16m^2}{4m^2-1} + 4mln\left(\frac{2m+1}{2m-1}\right)\right], m \neq 0 && (2.10)\\
F^{+}_{m} &= \frac{1}{2h}\left[\frac{8m^2-4m-1}{4m^2-1} - (2m-1)ln\left(\frac{2m+1}{2m-1}\right)\right], m \neq 0. && (2.11)
\end{aligned}$$

In the above equations, h is the mesh size. The above equation can be written in finite difference form:

$$\frac{D_{i-1}-2D_i+D_{i+1}}{h^2} = \frac{4}{\pi E'}\sum_{k=1}^{n} f_{k-i}P_k, \tag{2.12}$$

where h is the mesh size. The magnitude of f_i (evaluated in [21]) decreases rapidly with increasing $|i|$. Using (2.12) instead of the film thickness equation, a similar coupled system can be obtained. A and B are unchanged. However, E becomes a tridiagonal matrix and F is a band matrix rather than a full matrix since the fact that f_i decreases rapidly with increasing $|i|$ enables the entries that are positioned more than M ($M \geq 2$) entries away from the diagonal of the submatrix F to be moved to the right-hand side. It has been shown that the differential deflection method produces unchanged results with a radical reduction in computing time [21].

Both finite difference and continuous finite elements have been used by Evans et al. [17, 36, 37] to discretize the Reynolds equation. When the continuous quadratic finite element method was used, oscillation was observed in the contact region where the convection term dominates [36]. This is because the Reynolds equation behaves more like a hyperbolic equation when the convection term dominates, for which the continuous finite element discretization needs to be stabilized using techniques such as upwind schemes. To overcome this, in [37], the solution of the first order Reynolds equation which is smooth in the contact region and oscillating elsewhere, was employed in the central region. Mixing the solutions of the first order and the second order Reynolds equations, a smooth pressure profile was obtained over the entire computational domain.

2.1.4 Multigrid Methods

For many problems, standard iterative methods such as Gauss-Seidel relaxation are effective at eliminating the high-frequency or oscillatory components of the error, while leaving the low-frequency or smooth components relatively unchanged. The multigrid method [8] is able to accelerate convergence of the solution to such problems significantly because it is effective at eliminating both high-frequency and low-frequency components through the use of a sequence of grids.

The multigrid method was first applied to EHL problems by Lubrecht in 1986 [42], combined with the Gauss-Seidel relaxation. Venner [60, 61] introduced new relaxation methods which make the multigrid method more robust. The cavitation condition was simply implemented by forcing the negative pressures to be zero [25]. Venner's method can handle a large range of loaded cases and makes it possible to efficiently obtain more accurate numerical solutions by using huge numbers of grid points.

2.1.4.1 Full Approximation Scheme

The scheme used by Venner and Lubrecht is the Full Approximation Scheme (FAS) [8]. Consider the following nonlinear problem:

$$\mathscr{L}(u) = f, \ in \ \ \Omega, \tag{2.13}$$

where $\mathscr{L}$ is a differential operator, u is the solution and f is the right-hand side function. Let v denote a numerical approximation to the solution u. Then the error is:

$$e = u - v \tag{2.14}$$

and the residual is

$$\begin{aligned} r &= f - \mathscr{L}(v) \\ &= \mathscr{L}(v+e) - \mathscr{L}(v). \end{aligned} \tag{2.15}$$

For simplicity, we consider the two-grid correction scheme here. Suppose we have found an approximation, v^h, on the original uniform fine grid, to a solution u^h satisfying

$$\mathscr{L}^h(u^h) = f^h, \tag{2.16}$$

where h is the mesh size of the fine grid. Now the residual equation is used on the coarse grid, for which the mesh size is denoted by H, to approximate e^h

$$\mathscr{L}^H(v^H + e^H) - \mathscr{L}^H(v^H) = r^H, \tag{2.17}$$

where $\mathscr{L}^H$ is the coarse-grid operator, r^H is the coarse-grid residual, v^H is the coarse-grid approximation to v^h, and e^H is the coarse-grid approximation to e^h. Once e^H is computed, e^h can be corrected by

$$v^h \leftarrow v^h + I_H^h e^H, \tag{2.18}$$

where I_H^h is known as the prolongation operator. The coarse-grid residual r^H is calculated from the fine-grid residual r^h:

$$r^H = I_h^H r^h = I_h^H (f^h - \mathscr{L}^h(v^h)), \tag{2.19}$$

where I_h^H is known as the restriction operator. The current approximation v^H is calculated from the fine-grid approximation v^h

$$v^H = \tilde{I}_h^H v^h. \tag{2.20}$$

Note that $\tilde{I}_h^H$ does not have to be the same as I_h^H. The residual equation (2.17) can therefore be written as

$$\mathscr{L}^H(I_h^H v^h + e^H) = f^H = \mathscr{L}^H(I_h^H v^h) + I_h^H (f^h - \mathscr{L}^h(v^h)). \tag{2.21}$$

The goal is to find the solution $u^H = I_h^H v^h + e^H$ to the above system of equations. The coarse-grid error $e^H = u^H - I_h^H v^h$ can then be interpolated to the fine grid and used to correct the fine-grid approximation v^h:

$$v^h \leftarrow v^h + I_H^h e^H. \tag{2.22}$$

Let v^h denote a fine grid function. When transferring v^h from a fine grid to the next coarse grid, the most straightforward restriction operator is *injection*, for which the value of $I_h^H v^h$ on a coarse grid point is simply the value of v^h on the fine grid point coinciding with this coarse grid point. Alternatively, $I_h^H v^h$ can be calculated by taking a weighted average of the values of v^h on the coinciding fine grid point and some neighbouring sites. Figure 2.1 shows the injection operator and the full weighting operator for a one-dimensional problem. When transferring function v^H to the neighbouring fine grid, I_H^h

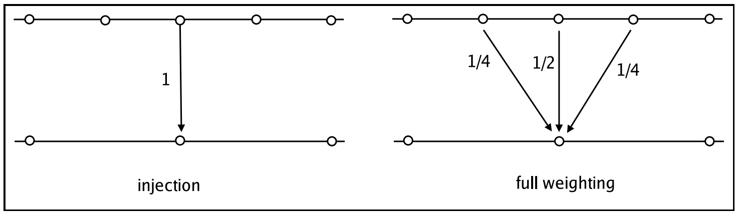

Figure 2.1: Restriction operators

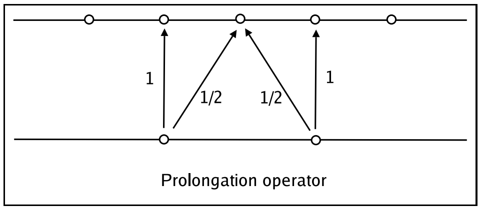

Figure 2.2: Prolongation operators

can be calculated by interpolation of some specified order. The most widely used, and simplest, prolongation operator is linear interpolation, which is shown in 1d in Figure 2.2.

The FAS algorithm on two grids is as follows:

- Restrict the current approximation v^h and the residual r^h on the fine grid to the coarse grid.
- Solve the coarse-grid problem $\mathscr{L}(u^H) = f^H$.
- Compute the coarse-grid approximation to the error: $e^H = u^H - v^H$.
- Interpolate e^H to the fine grid and correct the current fine-grid approximation: $v^h \leftarrow v^h + I_H^h e^H$.

This scheme can also be applied to linear problems [8]. The difference is that e^H can be solved directly on the coarse grid rather than u^H since

$$\mathscr{L}^H(u^H) - \mathscr{L}^H(v^H) = \mathscr{L}^H(e^H) \tag{2.23}$$

when $\mathscr{L}$ is a linear operator.

In order to eliminate various frequency errors effectively, a sequence of coarse grids are needed to eliminate the lower and lower frequency errors on the finest grid. The number of grid points on the coarsest level is usually so small that the coarsest grid equation can be solved exactly or almost exactly in a few sweeps. In this general case, the recursive coarse grid correction for level k is as follows:

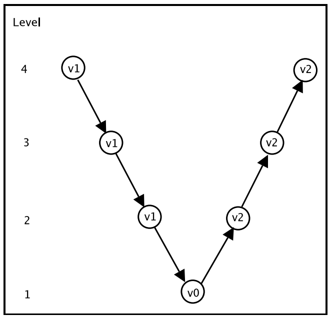

Figure 2.3: V cycle for 4 grid levels

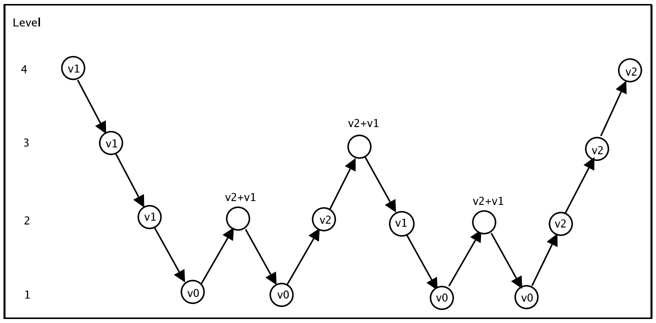

Figure 2.4: W cycle for 4 grid levels

- If level $k = 1$ (the coarsest level), perform ν_0 relaxation sweeps to solve the problem nearly exactly.
- If $k > 1$,
  - Perform ν_1 relaxation sweeps on level k.
  - Perform γ coarse grid correction cycles on level $k-1$.
  - Correct the solution on level k using the results on level $k-1$.
  - Perform ν_2 relaxation sweeps on level k.

When $\gamma = 1$, the coarse grid correction cycle is referred to as the $V(\nu_1, \nu_2)$ cycle. In the case that $\gamma = 2$, it is called $W(\nu_1, \nu_2)$ cycle. Figure 2.3 and 2.4 show the $V(\nu_1, \nu_2)$ cycle and the $V(\nu_1, \nu_2)$ cycle in the situation of 4 grid levels.

2.1.4.2 Multilevel Multi-Integration

It is usually expensive to calculate the film thickness since the film thickness equation consists of a global integral which can generally be written in the following form:

$$w(x) = \int_{\Omega} K(x,y)u(y)\mathrm{d}y, \quad x \in \Omega. \tag{2.24}$$

The discrete form on a uniform grid reads:

$$w_i^h = h \sum_{j=1}^{n} K_{i,j}^{hh} u_j^h, \tag{2.25}$$

where h is the mesh size. Equation (2.25) indicates that the computational complexity is $\mathscr{O}(n^2)$. In order to accelerate this computation, Multilevel Multi-Integration (MLMI) was introduced by Lubrecht [41]. The coarse grid integration of MLMI consists of two steps (here we only focus on line contact problems):

- If K is sufficiently smooth with respect to the y variable, let $\tilde{K}_{i,j}^{hh} \equiv [I_H^h K_{i,\cdot}^{hH}]_j$ be an approximation to $K_{i,j}^{hh}$ where I_H^h is an interpolation operator (typically the full weighting operator is used) and $K_{i,J}^{hH} \equiv K_{i,2J}^{hh}$. Then

  $$w_i^h = h \sum_j \tilde{K}_{i,j}^{hh} u_j^h + h \sum_j (K_{i,j}^{hh} - \tilde{K}_{i,j}^{hh}) u_j^h, \tag{2.26}$$

  where $K_{i,j}^{hh} - \tilde{K}_{i,j}^{hh} = 0$ when $j = 2J$ and $K_{i,j}^{hh} - \tilde{K}_{i,j}^{hh} = \mathscr{O}(h^{2p} K^{(2p)}(\xi))$ otherwise. Here $2p$ is the interpolation order and $K^{(2p)}(\xi)$ is a $2p^{th}$ derivative of K at point ξ. When K is smooth compared to u, the second term on the right hand side in (2.26) is small compared to the discretization error. Then

  $$\begin{aligned} w_i^h &\approx \tilde{w}_i^h \\ &\equiv h \sum_j \tilde{K}_{i,j}^{hh} u_j^h \\ &= h \sum_j [I_H^h K_{i,\cdot}^{hH}]_j u_j^h \\ &= h \sum_j K_{i,J}^{hH} [(I_H^h)^T u_{\cdot}^h]_J \\ &= H \sum_J K_{i,J}^{hH} u_J^H, \end{aligned} \tag{2.27}$$

  where $u^H \equiv 2^{-1} (I_H^h)^T u^h$. So w_i^h can be accurately approximated on the coarse grid.

- If K is sufficiently smooth with respect to the x direction, let $\hat{K}_{i,j}^{hh} \equiv [\hat{I}_H^h K_j^{Hh}]_i$ be an approximation to $K_{i,j}^{hh}$, where $\hat{I}_H^h = I_H^h$ can be used if $K(x,y)$ is symmetric. Then

  $$w_i^h = [\hat{I}_H^h w_{\cdot}^H]_i + h \sum_j (K_{i,j}^{hh} - \hat{K}_{i,j}^{hh}) u_j^h \tag{2.28}$$

where

$$w_I^H \equiv w_{2I}^h = h\sum_j K_{I,j}^{Hh} u_j^h = h\sum_j K_{2I,j}^{hh} u_j^h. \tag{2.29}$$

If I_H^h is of the order $2p$, $K_{i,j}^{hh} - \hat{K}_{i,j}^{hh} = 0$ when $i = 2I$ and $K_{i,j}^{hh} - \hat{K}_{i,j}^{hh} = \mathscr{O}(h^{2p} K^{(2p)}(\xi))$ otherwise. If K is sufficiently smooth with respect to the x direction,

$$w_i^h \approx [\hat{I}_H^h w_.^H]_i, \tag{2.30}$$

where

$$w_I^H \equiv w_{2I}^h. \tag{2.31}$$

Hence, we just need to evaluate w_i^h on the points $i = 2I$, then calculate the values on the intermediate points using interpolation.

Based on the above properties, two-grid MLMI reads:

- Transfer u^h to the coarse grid to obtain u^H.
- Calculate the coarse grid kernel $K_{I,J}^{HH}$ according to $K_{I,J}^{HH} = K_{2I,2J}^{hh}$.
- Compute w_I^H on the coarse grid.
- Inject w_I^H to the coinciding fine grid points $i = 2I$ and calculate the other w_i^h by interpolation.

In order to further accelerate the computation, a sequence of coarser grids are required and the coarse grid multi-summation is repeated recursively until a grid with about $\sqrt{n}$ grid points is reached on which the multi-summation requires $\mathscr{O}(n)$ operations. Further coarsening can not reduce the complexity because the transfer and the interpolation already requires $\mathscr{O}(n)$ operations.

For the elastic deformation integral in the film thickness equation, the kernel $K(x,y)$ has a singularity. Hence, when y and x are relatively close (or $\|j-i\| < m$ in the discrete form) $K_{i,j}^{hh} - \tilde{K}_{i,j}^{hh}$ and $K_{i,j}^{hh} - \hat{K}_{i,j}^{hh}$ can not be neglected. Then (2.27) and (2.30) should be replaced by:

$$w_i^h = H\sum_J K_{i,J}^{hH} u_J^H + \sum_{\|j-i\|\leqslant m} (K_{i,j}^{hh} - \tilde{K}_{i,j}^{hh}) u_j^h \tag{2.32}$$

and

$$w_i^h \approx [I_H^h w_.^H]_i + h\sum_{\|j-i\|\leqslant m} (K_{i,j}^{hh} - \hat{K}_{i,j}^{hh}) u_j^h, \tag{2.33}$$

where $m \propto ln(n)$ [60]. The advantage of this method is that the complexity can be reduced from $\mathscr{O}(n^2)$ to $\mathscr{O}(nln(n))$. For point contact, the generalization of this algorithm maintains its $\mathscr{O}(nln(n))$ efficiency [25], where n is the total number of the grid points on the finest level. In point contact cases, we can benefit very significantly from MLMI since n may be $\mathscr{O}(10^6)$.

2.2 Finite Difference Method

This section provides an explanation and demonstration of how EHL line contact problems are solved using the Finite Difference method. Yang's simplified multigrid [63] is adopted, for which the Gauss-Seidel relaxation is used over the entire domain and the FAS right-hand side in the film thickness equation is deleted since the film thickness is a function of the pressure rather than an independent equation (see below for further details). The free boundary condition is implemented by updating the outlet boundary position based on the current solution. The results indicate that the Gauss-Seidel relaxation is a stable relaxation scheme with good smoothing properties. This significantly simplifies the calculation procedure. However, it should be noted that smaller under-relaxation factors than those used by Venner [60] have to be adopted to ensure convergence.

Discretization of the 1d steady-state Reynolds equation (1.11) on a uniform grid with mesh size h gives:

$$L_i^h(P_i) = \frac{\varepsilon_{i-\frac{1}{2}}P_{i-1} - (\varepsilon_{i-\frac{1}{2}} + \varepsilon_{i+\frac{1}{2}})P_i + \varepsilon_{i+\frac{1}{2}}P_{i+1}}{h^2} - \frac{\bar{\rho}_i H_i - \bar{\rho}_{i-1}H_{i-1}}{h} = 0. \tag{2.34}$$

Discretization of the elastic deformation integral as described in the last section gives the following equation for H_i:

$$H_i = H_{00} + \frac{X_i^2}{2} - \frac{1}{\pi}\sum_{j=0}^{n} K_{ij}^{hh} P_j, \tag{2.35}$$

where K_{ij}^{hh} can be calculated analytically (see [60]):

$$K_{ij}^{hh} = \left(i-j+\frac{1}{2}\right)h\left(ln\left(\left|i-j+\frac{1}{2}\right|h\right)-1\right) - \left(i-j-\frac{1}{2}\right)h\left(ln\left(\left|i-j-\frac{1}{2}\right|h\right)-1\right). \tag{2.36}$$

The dimensionless force balance equation is discretized according to:

$$h\sum_{j=0}^{n-1}\frac{P_j + P_{j+1}}{2} - \frac{\pi}{2} = 0, \tag{2.37}$$

which is used to update H_{00} in the film thickness equation:

$$H_{00} \leftarrow H_{00} - c_2 \left(\frac{\pi}{2} - h \sum_{j=0}^{n-1} \frac{\tilde{P}_j + \tilde{P}_{j+1}}{2} \right), \tag{2.38}$$

where $\tilde{P}$ is the current solution and c_2 is a positive under-relaxation factor.

The P_i are updated using nonlinear Gauss-Seidel relaxation:

$$\bar{P_i} = \tilde{P_i} + c_1 \left(\frac{\partial L_i^h}{\partial P_i} \right)^{-1} r_i \tag{2.39}$$

where c_1 is the under-relaxation factor for pressure and r_i is the dynamic residual of the discrete Reynolds equation at site i:

$$r_i = -\frac{\varepsilon_{i-\frac{1}{2}} \bar{P}_{i-1} - (\varepsilon_{i-\frac{1}{2}} + \varepsilon_{i+\frac{1}{2}}) \tilde{P_i} + \varepsilon_{i+\frac{1}{2}} \tilde{P}_{i+1}}{h^2} + \frac{\tilde{\bar{\rho}}_i \tilde{H}_i - \bar{\rho}_{i-1} \bar{H}_{i-1}}{h}. \tag{2.40}$$

For simplicity, Venner [60] approximated $(\frac{\partial L_i^h}{\partial P_i})$ in (2.39) by

$$\begin{aligned} \frac{\partial L_i^h}{\partial P_i} &= \frac{\partial}{\partial P_i} \left(\frac{\varepsilon_{i-\frac{1}{2}} P_{i-1} - (\varepsilon_{i-\frac{1}{2}} + \varepsilon_{i+\frac{1}{2}}) P_i + \varepsilon_{i+\frac{1}{2}} P_{i+1}}{h^2} - \frac{\bar{\rho}_i H_i - \bar{\rho}_{i-1} H_{i-1}}{h} \right) \\ &\approx -\frac{(\varepsilon_{i-\frac{1}{2}} + \varepsilon_{i+\frac{1}{2}})}{h^2} + \frac{1}{\pi} \frac{\tilde{\bar{\rho}}_i K_{i,i}^{hh} - \tilde{\bar{\rho}}_{i-1} K_{i-1,i}^{hh}}{h}. \end{aligned} \tag{2.41}$$

Yang [63] used the following boundary conditions:

$$\begin{aligned} P(X) &= 0, \text{when } X = X_{in} \text{ and } X = X_{out} \\ P(X) &\geq 0, \text{otherwise} \end{aligned} \tag{2.42}$$

where X_{in} and X_{out} are the inlet and outlet boundary positions respectively. The following convergence criterion is introduced by Yang:

$$err_p = \frac{\sum_{i=0}^{n} |\tilde{P_i} - \bar{P_i}|}{\sum_{i=0}^{n} P_i} < 0.001. \tag{2.43}$$

Satisfactory convergence results can be obtained after 3 W cycles, for which the full-weighting restriction operator and the linear prolongation are used. However, it was found that the residuals r_i were still as large as $\mathscr{O}(10^{-4})$. This indicates that the solution has not been fully converged. Furthermore, since the negative pressures between the cavitation position $X_{cavitation}$ and the fixed outlet boundary are artificially forced to be zero, they do not satisfy the Reynolds equation at all. $X_{cavitation}$ is treated as a free boundary to reflect the fact that the Reynolds equation is only valid in the pressurised region. $X_{cavitation}$ is updated according to the current solution throughout the computation and the residuals r_i in the pressurised region are used as the convergence criterion. This allows the residuals to be driven much lower than with Yang's method alone.

The initial guess for H_{00} is calculated as follows:

$$H_{00} = H_c - E_c, \tag{2.44}$$

where

$$H_c = \frac{\pi}{8W}(11.9U^{0.74}G^{0.4}W^{0.2}) \tag{2.45}$$

is the correlation equation for the central film thickness introduced by Yang [66] and the deformation E_c can be calculated with the known initial pressure distribution [65, 66]. In the above equation, W, G and U are three nondimensional parameters that characterize each load situation [60].

Venner [60] indicated that the FAS should be applied to the film thickness equation. That is to say, the film thickness at nodal point i on a specific level k should be solved from

$$H_i^k = H_{00} + \frac{X_i^2}{2} - \frac{1}{\pi}\sum_{j=0}^{n} K_{ij}^k P_j^k + f_i^k \tag{2.46}$$

where $f_i^k = 0$ on the finest grid, whereas on all coarser grids:

$$f_i^k = [I_{k+1}^k \tilde{H}_.^{k+1}]_i - H_{00} - \frac{X_i^2}{2} + \frac{1}{\pi}\sum_j K_{ij}^{kk}[I_{k+1}^k \tilde{P}_.^{k+1}]_j. \tag{2.47}$$

However Yang [63] treated the film thickness as a function of the active variable P rather than an independent equation. For the coarse-grid film thickness equation, the film thickness is also calculated from the original film thickness equation. Numerical tests show that no significant difference in efficiency can be observed when using these two methods to calculate the film thickness on coarse levels. Here we follow Yang's method when calculating the film thickness for simplicity.

The overall multilevel solution procedure is as follows:

- Give an initial guess for the pressure (Hertzian dry contact) on the finest level and give an initial guess for H_{00}.
- Perform one $W(v_1, v_2)$ cycle to obtain a new pressure distribution. Note that H_{00} is only updated on the finest level and the film thickness is calculated directly rather

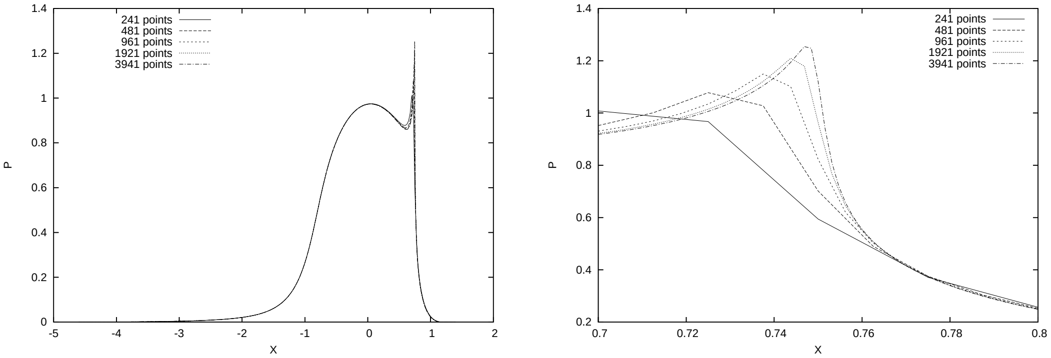

Figure 2.5: Pressure profiles, left, and pressure spikes, right ($W = 2.0 \times 10^{-11}$, $U = 4.0 \times 10^{-5}$ and $G = 5000$)

than using MLMI. Move the outlet boundary $X_{cavitation}$ according to the current solution on the finest level.

- Repeat until $\sqrt{\frac{\sum_{i=1}^{n} r_i^2}{n}} < 10^{-10}$.

The fixed coarsest grid has 31 grid points. Under-relaxation factors for pressure and H_{00} are 0.3 and 0.03, respectively. Numerical experiments show that the under-relaxation factors (c_1 and c_2) are not very sensitive to the load situations if there are not too many grid points on the finest level. However, usually the under-relaxation factors should be reduced as the number of grid levels increases.

A numerical result ($W = 2.0 \times 10^{-11}$, $U = 4.0 \times 10^{-5}$ and $G = 5000$) is shown in Figure 2.5, where W, U and G are the Dowson and Higginson dimensionless parameters [60]. It is clear that the pressure spike becomes better resolved when using more grid points. In EHL problems, the accuracy of pressure spikes is often problematic due to the steep gradient.

2.3 Finite Element Method

The continuous finite element method has been successfully applied to solve incompressible EHL problems [1,34,35,44,46,55,59,64]. However, for compressible case upwinding needs to be implemented for continuous finite element method since the Reynolds equation is convection-dominated in the contact region. In this section, an upwind linear finite element method [48] is used to discretize the Reynolds equation, for stability reasons, and a multigrid method is employed to accelerate the convergence. This upwind scheme can be viewed as a one-node numerical integration of the convection term, in which the node location controls the degree of upwinding.

In the reference element the following standard linear basis functions are used [58]:

$$N_1(\xi) = \frac{1-\xi}{2};\ N_2(\xi) = \frac{1+\xi}{2}, \tag{2.48}$$

where $\xi \in [-1,1]$. Let Ω_h be a partition of the domain $\Omega = [X_{inlet}, X_{outlet}]$ into n elements. In each element e, P is approximated in the following form:

$$P^e(X) = \sum_{i=1}^{2} u_i^e N_i^e(X),\ N_i^e(X) \in V \tag{2.49}$$

where u_i^e are the unknown coefficients and $N_i^e(X)$ are the local finite element basis functions which belong to a finite element space V. Note that in the reference element

$$N_1(-1) = 1;\ N_1(1) = 0;\ N_2(-1) = 0;\ N_2(1) = 1. \tag{2.50}$$

Hence in each element e, u_1^e and u_2^e are the pressures at the grid point e and $e+1$ respectively and

$$u_2^e = u_1^{e+1} = P_{e+1}. \tag{2.51}$$

The steady-state 1D Reynolds equation (1.11) can be discretized into the following form:

$$L(P,v) = a(P,v) - l(P,v) = 0,\ \forall v \in V, \tag{2.52}$$

where

$$a(P,v) = \sum_{e\in\Omega_h} \left(\int_e \varepsilon \frac{\partial P}{\partial X} \frac{\partial v}{\partial X}\,\mathrm{d}X \right) \tag{2.53}$$

and

$$l(P,v) = \sum_{e\in\Omega_h} \left(\int_e \bar{\rho} H \frac{\partial v}{\partial X}\,\mathrm{d}X \right). \tag{2.54}$$

The above discrete system can be written in the following general nonlinear form:

$$L^e(u^e) = A^e(u)u^e - b^e(u)(u^e) = 0, \forall e \in \Omega_h, \tag{2.55}$$

where

$$u^e = (u_1^e, u_2^e)^T, \tag{2.56}$$

$$A_{i,j}^e(u) = \int_e \varepsilon \frac{\partial N_j^e(X)}{\partial X} \frac{\partial N_i^e(X)}{\partial X}\,\mathrm{d}X = \frac{2}{h^e} \int_{-1}^{1} \varepsilon \frac{\partial N_j^e(X(\xi))}{\partial \xi} \frac{\partial N_i^e(X(\xi))}{\partial \xi}\,\mathrm{d}\xi \tag{2.57}$$

and

$$b_i^e(u) = \int_e \bar{\rho} H \frac{\partial N_i^e(X)}{\partial X}\,\mathrm{d}X = \frac{2}{h^e}\int_{-1}^{1} \bar{\rho} H \frac{\partial N_i^e(X(\xi))}{\partial \xi}\,\mathrm{d}\xi. \tag{2.58}$$

Here $i, j = 1, 2$ are the local indices. According to (2.51), the above local equations can be assembled into a global system:

$$L(P) = A(P)P - b(P) = 0, \tag{2.59}$$

where

$$P = (P_1, P_2, \ldots, P_{n+1})^T. \tag{2.60}$$

Here $A(P)$ is a tridiagonal matrix,

$$A_{I,I-1}(P) = A_{2,1}^e \tag{2.61}$$

$$A_{I,I}(P) = A_{2,2}^e + A_{1,1}^{e+1} \tag{2.62}$$

$$A_{I,I+1}(P) = A_{1,2}^{e+1}, \tag{2.63}$$

where $I = e+1$, and $b(P)$ in (2.59) is a vector:

$$b_I(P) = b_2^e(P) + b_1^{e+1}(P), \tag{2.64}$$

where $I = e+1$. In the above equations, $I = 1, 2, \ldots, n+1$ is the global index.

The integral $A_{i,j}^e$ is calculated using Gaussian Quadrature [58]:

$$A_{i,j}^e \approx \frac{2}{h^e}\sum_k \left(\varepsilon \frac{\partial N_j^e}{\partial \xi}\frac{\partial N_i^e}{\partial \xi}\right)_{\xi_k}^e w_k, \tag{2.65}$$

where w_k are the weight factors corresponding to the locations (abscissas) ξ_k where the integrand $\varepsilon \frac{\partial N_j^e}{\partial \xi}\frac{\partial N_i^e}{\partial \xi}$ is evaluated. Given P, it is easy to evaluate $\bar{\eta}(P_{\xi_k}^e)$ and $\bar{\rho}(P_{\xi_k}^e)$ using (1.14) and (1.15), where

$$P_{\xi_k}^e = \sum_{j=1}^{2} u_j^e N_j^e(\xi_k). \tag{2.66}$$

Before computing $H_{\xi_k}^e$, we first evaluate H at each grid point using (2.35). Then $H_{\xi_k}^e$ is calculated using linear interpolation:

$$H_{\xi_k}^e = H_e N_1^e(\xi_k) + H_{e+1} N_2^e(\xi_k), \tag{2.67}$$

where H_e and H_{e+1} are the film thicknesses at the grid points e and $e+1$ respectively.

Finally $\varepsilon^e_{\xi_k}$ can be calculated from (1.10) with $\bar{\eta}(P^e_{\xi_k})$, $\bar{\rho}(P^e_{\xi_k})$ and $H^e_{\xi_k}$.

As is well known, particularly in highly loaded cases, the convection term of the Reynolds equation dominates in the contact region. Therefore, an upwind scheme has to be used for the discretization of the convection term, or numerical oscillation will be observed [36]. Here the upwinding is implemented by using a special one-node numerical integration [48] when evaluating b^e_i:

$$b^e_i = \int_{-1}^{1} \bar{\rho} H \frac{\partial N^e_i}{\partial \xi} \,\mathrm{d}\xi \approx 2.0 \left(\bar{\rho} H \frac{\partial N^e_i}{\partial \xi} \right)_{\xi_{int}}, \tag{2.68}$$

where ξ_{int} can be located between -0.7 and -1.0 [48]. Note that the FE discretization of the convection term would be equivalent to the upwind FD discretization if $\xi_{int} = -1.0$.

Since the linear FE method is used to discretize the Reynolds equation, the actual unknowns are the pressures at the grid points. Furthermore, the employed upwind scheme is very similar to the FD upwinding. Therefore, the resulting nonlinear discrete system (2.59) is similar to (2.34). So here we use a similar relaxation scheme to update the pressure from the Reynolds equation which is discretized on a uniform grid:

$$\bar{P_I} = \tilde{P}_I + \left(\frac{\partial L_I}{\partial P_I} \right)^{-1} r_I \tag{2.69}$$

where r_I is the dynamic residual:

$$r_I = b_I - \sum_{J=1}^{n+1} A_{I,J} P_J \tag{2.70}$$

and $\frac{\partial L^h_I}{\partial P_I}$ is approximated by:

$$\frac{\partial L^h_I}{\partial P_I} \approx A_{I,I} - \frac{\partial b_I}{\partial P_I}. \tag{2.71}$$

Here, $\frac{\partial b_I}{\partial P_I}$ is calculated as follows:

$$\frac{\partial b_I}{\partial P_I} = \frac{\partial b^e_2}{\partial u^e_2} + \frac{\partial b^{e+1}_1}{\partial u^{e+1}_1}, \tag{2.72}$$

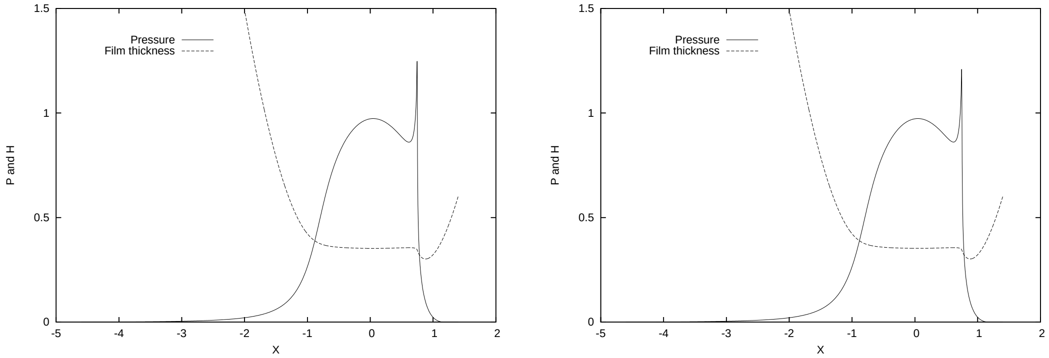

Figure 2.6: FE solution, left, and FD solution, right ($W = 2.0 \times 10^{-11}$, $U = 4.0 \times 10^{-5}$ and $G = 5000$)

where $\frac{\partial b_2^e}{\partial u_2^e}$ and $\frac{\partial b_1^{e+1}}{\partial u_1^{e+1}}$ can be evaluated by:

$$
\begin{aligned}
\frac{\partial b_i^e}{\partial u_i^e} &= \frac{\partial}{\partial u_i^e}\left(2.0\bar{\rho}H\frac{\partial N_i^e}{\partial \xi}\right)_{\xi_{int}} && (2.73)\\
&\approx 2.0\bar{\rho}_{\xi_{int}}\frac{\partial H_{\xi_{int}}}{\partial u_i^e}\frac{\partial N_i^e}{\partial \xi}(\xi_{int}) && (2.74)\\
&= 2.0\bar{\rho}_{\xi_{int}}\frac{\partial}{\partial u_i^e}\left(H_e N_1^e(\xi_{int}) + H_{e+1}N_2^e(\xi_{int})\right)\frac{\partial N_i^e}{\partial \xi}(\xi_{int}) && (2.75)\\
&= 2.0\bar{\rho}_{\xi_{int}}(K_{e,I}^{hh}N_1^e(\xi_{int}) + K_{e+1,I}^{hh}N_2^e(\xi_{int}))\frac{\partial N_i^e}{\partial \xi}(\xi_{int}). && (2.76)
\end{aligned}
$$

Since the discrete system and the relaxation method are quite similar to those for the FD method, the same overall solution procedure is employed here. A very similar convergence rate can be obtained to that for the FD method. Figs 2.6 and 2.7 depict the comparisons of the pressure profiles and thickness profiles calculated using the FD method and the FE method. Here $\xi_{int} = -0.8$ is used for each of the two loaded cases ($W = 2.0 \times 10^{-11}$, $U = 4.0 \times 10^{-5}$, $G = 5000$ and $U = 1.0 \times 10^{-11}$, $W = 1.0 \times 10^{-4}$, $G = 5000$) using 1921 grid points. Since the linear FE discretization is quite similar to the FD discretization, the resulting global pressure profiles are similar. But the height of the pressure spikes are slightly different. In Figure 2.6, the heights of the pressure spikes are 1.24785 on the left and 1.20935 on the right. For the other loaded case in Figure 2.7, the heights of the spikes are 0.77368 on the left and 0.74874 on the right.

Although the application of the linear finite element method is successful since the upwinding can be implemented using one-node integration, it is difficult to implement the upwinding in the same way for higher order continuous finite element methods. Therefore, new upwind schemes are required to stabilize the discretization of the Reynolds

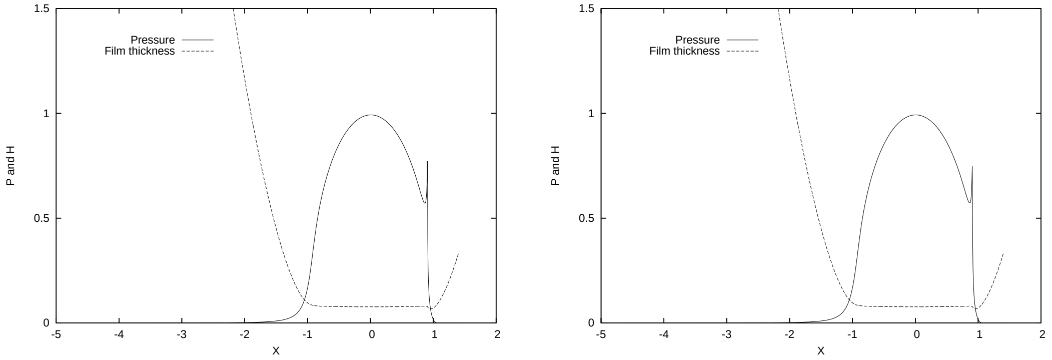

Figure 2.7: FE solution, left, and FD solution, right ($U = 1.0 \times 10^{-11}$, $W = 1.0 \times 10^{-4}$ and $G = 5000$)

equation when using higher order finite elements.

2.4 Conclusion

In this chapter, the most widely used computational methods for EHL problems are briefly summarized. In section 2.3 a much more detailed description is provided for the "FD+multigrid" method [60, 63] since this is the most popular method for EHL problems at present, and it will be used for some comparisons later in this thesis. Although only an implementation for the line contact problem is introduced here, the extension to point contacts is quite straightforward [25, 60]. However, it is difficult to resolve a very good quality spike for highly loaded cases using FD schemes since they are low-order. Hence, particularly for point contacts, huge numbers of grid points must be used [27]. More accurate numerical methods would therefore be desirable. In this chapter, a continuous linear finite element method was implemented, for which the discretization is stabilized through an upwinding which is implemented using one-node integration. This method is stable, but no more accurate than the standard FD scheme. Furthermore, this upwinding implementation can not be generalized to higher-order continuous finite elements. Therefore, a method which is both stable and highly accurate is required. In the next chapter, a new high order numerical method is discussed.

Chapter 3

Discontinuous Galerkin Method

3.1 Introduction

In the preceding chapter, various numerical methods applied to EHL problems have been discussed and our own implementation of the standard FD and linear FE discretization schemes has been presented. However, all methods discussed previously are low order schemes. For highly loaded cases, it is always difficult to capture the pressure spike precisely, unless huge numbers of grid points are used. In practice, the accuracy of the pressure spike dominates many important quantities, such as friction [27]. Hence, it is desirable to improve the accuracy of the numerical solutions of EHL problems. In this thesis, a high order Discontinuous Galerkin (DG) method, which is a class of finite element method, is employed to solve EHL problems. Before going straight to the application of the high order DG to EHL problems, some important properties, such as convergence rate and flexibility in adaptivity, will be discussed briefly in this chapter.

3.2 History of Discontinuous Galerkin

The original Discontinuous Galerkin (DG) method was introduced in 1973 by Reed and Hill [51] for solving the neutron transport equation. The first *a priori* error estimates for the DG method for linear hyperbolic problems were given in 1974 by LeSaint and Raviart [39] and the convergence rate of $\mathcal{O}(h^p)$ in the $L_2(\Omega)$-norm for general triangulations was proved for p^{th} order approximation of smooth solutions. In 1986, Johnson and Pitkaranta [38] proved a rate of convergence of $\mathscr{O}(h^{p+\frac{1}{2}})$ for general triangulations which was proved to be optimal by Peterson [49]. A further optimal rate of convergence, of $\mathscr{O}(h^{p+1})$, was obtained by Richter [53] for some structured non-Cartesian Grids. Later, the super-convergence property of DG methods has been further demonstrated by *a posteriori* error analysis which was introduced by Stroubolis and Oden [57]. Based on the successful application of DG to smooth linear hyperbolic problems, people began to consider the the application of DG to nonlinear hyperbolic problems. Significant progress was made in this regard by Cockburn and Shu, who introduced and developed the Runge-Kutta Discontinuous Galerkin method (RKDG) [11, 12, 14].

Many PDEs of practical interest are of convection-diffusion form rather than being purely hyperbolic. Stimulated by the super-convergence property of DG methods, people began to try to solve convection-diffusion problems using DG methods. A noteworthy attempt was made by Bassi [3]. In that approach, both u and Du were treated as independent unknowns. Then the second-order equation was rewritten to be a first-order system which is easy to discretize using DG. This method was generalized by Cockburn and Shu [13] in 1998 by introducing the local Discontinuous Galerkin method. By carefully defining the numerical flux, high-order accuracy and nonlinear stability can be achieved. But a significant disadvantage is that the number of degrees of freedom doubles since an auxiliary variable is introduced.

In 1998, a new DG method was introduced to discretize second-order problems by Baumann and Oden [5, 45] without introducing any auxiliary unknowns. Over each element boundary, both solution values and fluxes may be discontinuous. The continuity requirements over inter-element boundaries, and the boundary conditions, are imposed in a weak form. This treatment of inter-element boundaries prevents the appearance and spreading of numerical oscillations. For diffusion problems, this method was proved to be stable for polynomial basis functions of degree ≥ 3 and the L^2-rate of convergence found to be $\mathscr{O}(h^{p+1})$ for p odd and $\mathscr{O}(h^p)$ for p even. In convection-dominated cases, no artificial diffusion is introduced to improve the stability, which allows the order of accuracy to grow linearly with the order of the basis functions (assuming the underlying solution is smooth). So this is a high-order scheme which is applicable to both convection-dominated problems and diffusion-dominated problems. Since it is not necessary to impose the continuity restrictions strongly, it is extremely easy to handle h-adaptivity for any type of grid. Furthermore, the degree of the basis functions can be easily changed from one element to another. It is for these reasons that this DG method is employed to solve EHL problems in this thesis.

3.3 Advantages of Discontinuous Galerkin

The key feature of discontinuous Galerkin methods (DG) is that they assume discontinuous approximate solutions, for which DG methods can be viewed as generalizations of finite volume methods [10]. In other words, DG methods combine the advantages of finite element methods and of finite volume methods.

- High order accuracy. Similar to traditional finite element methods, when the solution is smooth DG methods can obtain arbitrarily high order accuracy by suitably choosing the degree of the approximating polynomials.

- Compared to continuous finite element methods, DG methods can easily handle upwinding through carefully defining numerical fluxes, which provides stable numerical discretizations for convection-dominated problems.

- DG methods are well suited to handling complicated geometries and the treatment of the boundary conditions is very simple. DG methods incorporate the boundary conditions in weak form using the property of discontinuity, and 2d complex geometries can be approximated using triangles and quadrilaterals.

- It is very easy for DG methods to be used adaptively. Since the solution is discontinuous over element interfaces, h-adaptivity can be easily performed without the restrictions imposed by the continuity requirements of continuous finite element methods. Furthermore, the order of the approximating polynomial does not have to be the same for different elements. Hence, the implementation of p-adaptivity is very straightforward and natural. Of course, we can adapt the grid concurrently with adjusting the polynomial degree of elements. This approach is called h-p-adaptivity.

- DG methods are easy to implement in parallel. When using DG methods, the mass matrix is block diagonal and the size of blocks is equal to the number of degrees of freedom inside the corresponding elements since the solution over element boundaries is discontinuous.

Based on the above advantages, DG methods have been widely used for some convection-dominated problems [3, 5, 13, 45, 57].

3.4 High Order and Super-Convergence

One important issue for numerical simulation is accuracy. In practice, people prefer high-order schemes because of their high-order accuracy. In this section, we will demonstrate the super-convergence property of Oden's DG scheme [5, 45] through solving several linear problems.

3.4.1 Diffusion Problems

Here we consider a one-dimensional partial differential equation (PDE) [32] that may be used to model isoviscous, incompressible hydrodynamic lubrication. The nondimensional Reynolds equation is

$$\frac{d}{dX}\left(H^3\frac{dP}{dX}\right)-\lambda\frac{dH}{dX}=0 \tag{3.1}$$

where $X\in[X_{inlet},X_{outlet}]$, λ is a given constant and

$$H(x)=H_0+\frac{X^2}{2}. \tag{3.2}$$

In the zero boundary pressure case, $P=0$ at both $X_{inlet}=-\infty$ and $X_{outlet}=X_c$, the cavitation point. The outlet boundary, $X_{outlet}=X_c$, is fixed at a predetermined value, as is H_0.

Let Ω_h be a partition of the domain $\Omega=[X_{inlet},X_{outlet}]$ into N elements. Let $\Gamma_{int}=\cup\Gamma_{ef}$ denote internal interfaces between elements, where Γ_{ef} is the grid point separating elements e and f. D_L (X_{inlet}) and D_R (X_{outlet}) are the left and right Dirichlet boundaries respectively. We define the jump of a function v on the element interface Γ_{ef}

$$[v(x)]_{ef}=\lim_{x\to\Gamma_{ef},x\in e}v(x)-\lim_{x\to\Gamma_{ef},x\in f}v(x),\ e>f, \tag{3.3}$$

and the average

$$\langle v(x)\rangle_{ef}=\frac{1}{2}\left(\lim_{x\to\Gamma_{ef},x\in e}v(x)+\lim_{x\to\Gamma_{ef},x\in f}v(x)\right). \tag{3.4}$$

For two functions v,w we have the formula

$$[vw]_{ef}=[v]_{ef}\langle w\rangle_{ef}+[w]_{ef}\langle v\rangle_{ef}. \tag{3.5}$$

Testing with a function v and integrating by parts we get the following discrete system:

$$L(P,v)=a(P,v)-l(v)=0,\ \forall v\in V. \tag{3.6}$$

The discretization of the diffusion term is:

$$
\begin{aligned}
a(P,v) &= \int_{\Omega} \frac{d}{dx}\left(-H^3\frac{dP}{dx}\right) v\,dx \\
&= \sum_{e=1}^{n}\left(\int_e H^3\frac{dP}{dx}\frac{dv}{dx}\,dx + \left(vH^3\frac{dP}{dx}\right)|_{e^L} - \left(vH^3\frac{dP}{dx}\right)|_{e^R}\right) \\
&= \sum_{e=1}^{n}\left(\int_e H^3\frac{dP}{dx}\frac{dv}{dx}\,dx\right) + \left(vH^3\frac{dP}{dx}\right)|_{D_L} - \left(vH^3\frac{dP}{dx}\right)|_{D_R} + \sum_{\Gamma_{int}}\left[vH^3\frac{dP}{dx}\right] \\
&= \sum_{e=1}^{n}\left(\int_e H^3\frac{dP}{dx}\frac{dv}{dx}\,dx\right) + \left(vH^3\frac{dP}{dx}\right)|_{D_L} - \left(vH^3\frac{dP}{dx}\right)|_{D_R} \\
&+ \sum_{\Gamma_{int}}\left([v]\left\langle H^3\frac{dP}{dx}\right\rangle + \langle v\rangle\left[H^3\frac{dP}{dx}\right]\right)
\end{aligned}
\qquad (3.7)
$$

where $\left[H^3\frac{dP}{dx}\right]$ is the jump in the flux over inter-element boundaries which is zero (assuming that P is the solution of (3.1)). Then

$$
\begin{aligned}
a(P,v) &= \sum_{e=1}^{n}\left(\int_e H^3\frac{dP}{dx}\frac{dv}{dx}\,dx\right) + \left(vH^3\frac{dP}{dx}\right)|_{D_L} \\
&- \left(vH^3\frac{dP}{dx}\right)|_{D_R} + \sum_{\Gamma_{int}}[v]\left\langle H^3\frac{dP}{dx}\right\rangle .
\end{aligned}
\qquad (3.8)
$$

The discrete convection term is:

$$
\begin{aligned}
l(v) &= \int_{\Omega}\frac{d}{dx}(-\lambda H)v\,dx \\
&= \sum_{e=1}^{n}\left(\int_e \lambda H\frac{dv}{dx}\,dx + (\lambda Hv)|e^L - (\lambda Hv)|e^R\right) \\
&= \sum_{e=1}^{n}\left(\int_e \lambda H\frac{dv}{dx}\,dx\right) + (\lambda Hv)|_{D_L} - (\lambda Hv)|_{D_R} + \sum_{\Gamma_{int}}[\lambda Hv] \\
&= \sum_{e=1}^{n}\left(\int_e \lambda H\frac{dv}{dx}\,dx\right) + (\lambda Hv)|_{D_L} - (\lambda Hv)|_{D_R} + \sum_{\Gamma_{int}}\left([v]\langle\lambda H\rangle + \langle v\rangle[\lambda H]\right) \\
&= \sum_{e=1}^{n}\left(\int_e \lambda H\frac{dv}{dx}\,dx\right) + (\lambda Hv)|_{D_L} - (\lambda Hv)|_{D_R} + \sum_{\Gamma_{int}}[v]\langle\lambda H\rangle .
\end{aligned}
\qquad (3.9)
$$

Here e^L and e^R are the left and right boundaries of element e respectively.

In order to weakly enforce the continuity of the solution over element boundaries, the following penalty term is added to the above discrete form [4, 5, 45]:

$$\sum_{\Gamma_{int}}[P]\left\langle -H^3\frac{dv}{dx}\right\rangle = 0. \tag{3.10}$$

On the Dirichlet boundary, the penalty term becomes:

$$\begin{aligned}\left((-H^3\frac{dv}{dx})(P-P_{inlet})\right)|_{D_L} = 0,\\ \left((H^3\frac{dv}{dx})(P-P_{outlet})\right)|_{D_R} = 0.\end{aligned} \tag{3.11}$$

Then the final discrete form is:

$$\begin{aligned} a(P,v) &= \sum_{e=1}^{n}\left(\int_e H^3\frac{dP}{dx}\frac{dv}{dx}dx\right)+\sum_{\Gamma_{int}}([v]\left\langle H^3\frac{dP}{dx}\right\rangle - [P]\left\langle H^3\frac{dv}{dx}\right\rangle)\\ &+ \left(vH^3\frac{dP}{dx}\right)|_{D_L} - \left(vH^3\frac{dP}{dx}\right)|_{D_R}\\ &+ \left(-H^3\frac{dv}{dx}\right)P|_{D_L} + \left(H^3\frac{dv}{dx}\right)P|_{D_R}, \end{aligned} \tag{3.12}$$

and

$$\begin{aligned} l(v) &= \sum_{e=1}^{n}\left(\int_e \lambda H\frac{dv}{dx}dx\right)+\sum_{\Gamma_{int}}[v]\langle\lambda H\rangle\\ &+ (\lambda Hv)|_{D_L} - (\lambda Hv)|_{D_R} + \left(-H^3\frac{dv}{dx}\right)P_{inlet}|_{D_L} + \left(H^3\frac{dv}{dx}\right)P_{outlet}|_{D_R}. \end{aligned} \tag{3.13}$$

In each element e, P is approximated in the following form:

$$P^e(X) = \sum_{i=1}^{p^e+1} u_i^e N_i^e(X),\; N_i^e(X) \in V, \tag{3.14}$$

where p^e is the order of the approximating polynomial, u_i^e are the unknown coefficients and $N_i^e(X)$ are the local finite element basis functions which belong to a finite dimensional finite element space V.

Substitution of (3.14) in (3.6) results in the following linear system:

$$L(U) = AU - b = 0, \tag{3.15}$$

where

$$U = \left(u_1^1, \ldots, u_{p^1+1}^1; \ldots; u_1^N, \ldots, u_{p^N+1}^N\right)^T. \tag{3.16}$$

Since the entries of U are ordered element by element (see 3.16), A is a tridiagonal block matrix and the size of the each block is determined by the degree of the current test functions and basis functions on the corresponding element. Therefore, equation (3.15) can be written in the following form:

$$\begin{bmatrix} A^{1,1} & A^{1,2} & & & & & \\ A^{2,1} & A^{2,2} & A^{2,3} & & & & \\ & \ddots & \ddots & \ddots & & & \\ & & A^{e,e-1} & A^{e,e} & A^{e,e+1} & & \\ & & & \ddots & \ddots & \ddots & \\ & & & & A^{N-1,N-2} & A^{N-1,N-1} & A^{N-1,N} \\ & & & & & A^{N,N-1} & A^{N,N} \end{bmatrix} \begin{bmatrix} U^1 \\ \vdots \\ U^{e-1} \\ U^e \\ U^{e+1} \\ \vdots \\ U^N \end{bmatrix} = \begin{bmatrix} b^1 \\ \vdots \\ b^{e-1} \\ b^e \\ b^{e+1} \\ \vdots \\ b^N \end{bmatrix} \tag{3.17}$$

Here the resulting discrete linear system (3.17) is solved using Gaussian Elimination.

Figure 3.1 plots the errors versus N on a $log - log$ scale where:

$$Error = \sqrt{\int_{X_{inlet}}^{X_{outlet}} (u_{numerical} - u_{analytic})^2 \, dx}. \tag{3.18}$$

The numerical results indicate that the behaviour of this method in L^2 is different for odd or even order polynomial approximations. Figure 3.1 indicates an asymptotic convergence rate of order $O(h^{p+1})$ for p odd and $O(h^p)$ for p even. In [45], it was proved that for polynomial basis functions of $degree > 2$ the DG method used above is stable. However, numerical experiments indicate that the method is stable and convergent for polynomial basis functions of $degree > 1$. Note that the method is not stable for $p_e < 2$.

3.4.2 Convection-Diffusion Problems

Consider the following general linear convection-diffusion equation:

$$-s_1 \frac{d^2P}{dX^2} + s_2 \frac{dP}{dX} = f(X), \tag{3.19}$$

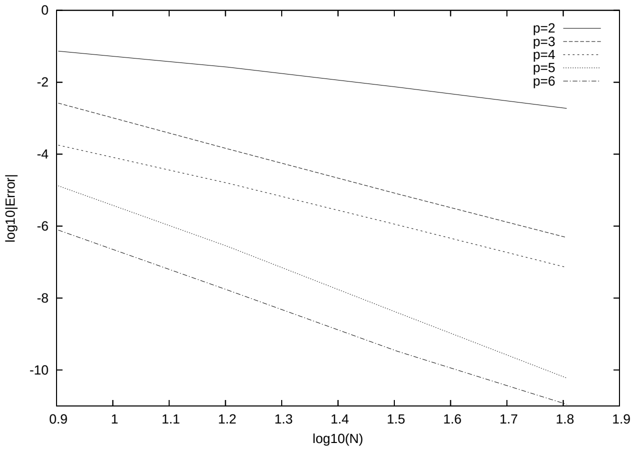

Figure 3.1: L^2-norm of the error when solving the diffusion problem using high-order DG with uniform meshes

with the simple boundary condition:

$$\begin{aligned} P(X_{inlet}) &= P_{analytic}(X_{inlet}), \\ P(X_{outlet}) &= P_{analytic}(X_{outlet}), \end{aligned} \tag{3.20}$$

where s_1 and s_2 are constants. Using Oden's DG scheme [5, 45], the above equation can be discretized into the following system:

$$L(P,v) = a(P,v) - l(P,v) = 0,\ \forall v \in V, \tag{3.21}$$

where

$$\begin{aligned} a(P,v) &= \sum_{e=1}^{n}\left(\int_e s_1 \frac{\partial P}{\partial X}\frac{\partial v}{\partial X}\,\mathrm{d}X\right) + \sum_{\Gamma_{int}}\left([v]\left\langle s_1\frac{\partial P}{\partial X}\right\rangle - [P]\left\langle s_1\frac{\partial v}{\partial X}\right\rangle\right) \\ &+ \left(vs_1\frac{\partial P}{\partial X}\right)|_{X_{inlet}} - \left(vs_1\frac{\partial P}{\partial X}\right)|_{X_{outlet}} \\ &- \left(Ps_1\frac{\partial v}{\partial X}\right)|_{X_{inlet}} + \left(Ps_1\frac{\partial v}{\partial X}\right)|_{X_{outlet}}, \end{aligned} \tag{3.22}$$

and

$$\begin{aligned} l(P,v) &= \sum_{e=1}^{n}(f(X)v) + \sum_{e=1}^{n}\left(\int_e s_2 P\frac{\partial v}{\partial X}\,\mathrm{d}x\right) + \sum_{\Gamma_{int}}[v]\langle s_2 P^-\rangle \\ &+ (s_2 Pv)|_{X_{inlet}} - (s_2 Pv)|_{X_{outlet}} \\ &- \left(P_{inlet}s_1\frac{\partial v}{\partial X}\right)|_{X_{inlet}} + \left(P_{outlet}s_1\frac{\partial v}{\partial X}\right)|_{X_{outlet}}. \end{aligned} \tag{3.23}$$

In the above equations,

$$P^- = \lim_{\sigma \to 0^+} P(x-\sigma), \text{ for } x \in \Gamma_{int}. \tag{3.24}$$

This provides sufficient upwinding to ensure a stable solution [5]. In this example we choose $f(X)$ such that the exact solution is as follows:

$$P_{analytic}(X) = 5X^{12} - 6X^4. \tag{3.25}$$

The value of $f(X)$ can be obtained by substituting the exact solution into (3.19), to give

$$f(x) = -s_1(660X^{10} + 42X^5 - 72X^2) + s_2(60X^{11} + 7X^6 - 24X^3). \tag{3.26}$$

The computational domain is given by:

$$\begin{aligned} X_{inlet} &= -1, \\ X_{outlet} &= 1. \end{aligned} \tag{3.27}$$

Note different s_1 and s_2 result in different types of equation. If $s_1 \neq 0$ and $s_2 = 0$, equation (3.19) is a diffusion equation. It becomes a pure convection equation with $s_1 = 0$ and $s_2 \neq 0$. When $s_1 \neq 0$ and $s_2 \neq 0$, it is a general convection-diffusion problem.

Figure 3.2 and Figure 3.3 show the convergence rates of the DG method for a convection problem ($s_1 = 0$ and $s_2 = 1$) and a convection-diffusion problem ($s_1 = 1$ and $s_2 = 1$) respectively. For the convection problem, a higher-order convergence rate is observed with increasing order. For the diffusion problem, the convergence rate for even and odd orders are different, but high-order convergence is still observed.

3.5 Adaptivity

In the previous section, all numerical results are calculated on uniform grids and the order of the basis functions is the same throughout the domain. As we can see from the above figures, more accurate solutions can be obtained by globally refining the grid or globally increasing the order of the basis functions. However, both of these strategies significantly increase the expense of computation. A more effective way to improve accuracy is often through the use of adaptivity, which is designed to obtain an accurate approximate solution within a preset error tolerance at the least computational cost.

One of the most widely used adaptive methods is h-adaptivity, particularly for low-

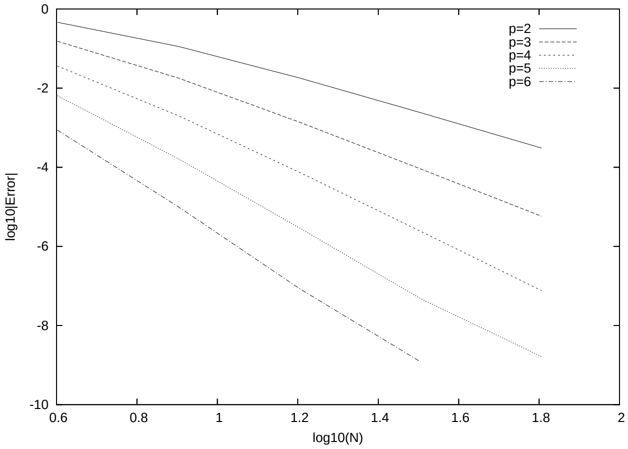

Figure 3.2: L^2-norm of the error when solving the convection problem using high-order DG

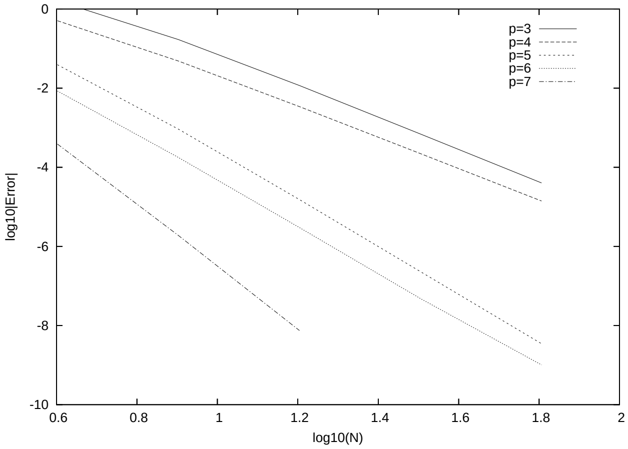

Figure 3.3: L^2-norm of the error when solving the convection-diffusion problem using high-order DG

order schemes, since the only way for low-order schemes to improve accuracy is to refine the grid. Mesh-adaptivity methods need not be be limited to this alone however:

- h-refinement: locally refine the spatial partition in the region where the current solution is not accurate enough.
- r-refinement: relocate the mesh points in order to obtain a better resolution of the solution with a fixed number of unknowns.
- mesh coarsening: coarsen the mesh where the current solution is “over-accurate” to reduce the computational cost.

For some numerical methods, such as continuous finite element, h-adaptivity can introduce additional difficulties. For example, when using continuous finite elements with non-uniform quadrilateral elements in two dimensions, the hanging nodes that appear on some element edges (next to a refined region) need special treatment to avoid discontinuities in the solution. This problem does not exist for DG methods since DG allows discontinuities over element boundaries. Therefore, the application of h-adaptivity to DG methods is very straightforward, even in two dimensions.

For high-order schemes, an alternative to h-adaptivity is p-adaptivity. Instead of refining the local meshes, local accuracy can be improved by increasing the order of the local basis functions. Furthermore, in regions where the solution is “over accurate”, we can reduce the order of the basis functions to reduce the computational complexity. For DG methods, it will not lead to any difficulty to change the order of the approximating polynomial from one element to another.

Combining h-adaptivity and p-adaptivity approaches leads to hp-adaptivity [10, 58] in which both the element size and order of polynomial used per element are varied. That means, we can change the mesh concurrently with increasing the order of the basis functions. The hp-adaptivity will not be considered in this thesis, but it is a natural extension of what follows.

3.6 Conclusion

In this chapter, some important properties of DG methods are discussed. Compared to finite difference and finite volume, DG can give much more accurate solutions. Furthermore, DG is stable in discretization and flexible in adaptivity in contrast with continuous finite element methods. In the following chapters, we will use Oden’s high-order DG scheme to solve EHL problems, for which finite differences may not give sufficiently accurate solutions and higher order continuous finite element methods are not stable.

Chapter 4

High Order DG Solution of Steady State Line Contact Problems

4.1 Introduction

In this chapter, a high order Discontinuous Galerkin method is employed to solve steady-state isothermal line contact problems. The Reynolds equation is discretized using Oden's DG method [5, 45]. Upwinding is simply implemented based on the discontinuity feature of DG. In the film thickness equation, since the pressure is expressed in a high-order form, a new kernel is defined for the convenience of calculating the elastic deformation. The global integral in the force balance equation is evaluated element-by-element using numerical integration. Based on the features of the Reynolds equation and the DG method used, a nonlinear smoother is introduced to relax the resulting nonlinear discrete system, which has been experimentally proven to be stable and robust. In order to obtain accurate numerical solutions at low expense, two simple automatic h-adaptivity methods are introduced based on the discontinuities over element boundaries and the high-order contributions respectively. Furthermore, a specific example is given which indicates that h-p-adaptivity is also feasible.

Numerical experiments show that this method is stable across a wide range of loads and permits accurate solutions using just a small number of degrees of freedom. In highly loaded cases, the captured pressure spike looks steep and smooth. The cavitation condition may be handled by using the penalty method which was introduced by Wu and Oden [64] in 1986. However, other approaches are also possible, such as treating the problem as a free boundary problem, where the cavitation position is captured explicitly [40]. Both techniques are considered in this chapter.

4.2 Discretization

4.2.1 The Reynolds Equation

Let Ω_h be a partition of the domain $\Omega = [X_{inlet}, X_{outlet}]$ into N elements. Let $\Gamma_{int} = \cup\Gamma_{ef}$ denote internal interfaces between elements, where Γ_{ef} is the grid point separating elements e and f. As before, we define the jump of a function v on the element interface Γ_{ef}

$$[v(x)]_{ef} = \lim_{x\to\Gamma_{ef}, x\in e} v(x) - \lim_{x\to\Gamma_{ef}, x\in f} v(x),\ e > f, \tag{4.1}$$

and the average

$$\langle v(x)\rangle_{ef} = \frac{1}{2}\left(\lim_{x\to\Gamma_{ef}, x\in e} v(x) + \lim_{x\to\Gamma_{ef}, x\in f} v(x)\right). \tag{4.2}$$

In each element e, P is approximated in the following form:

$$P^e(X) = \sum_{i=1}^{p^e+1} u_i^e N_i^e(X),\ N_i^e(X) \in V \tag{4.3}$$

where p^e is the order of the approximating polynomial, u_i^e are the unknown coefficients and $N_i^e(X)$ are the local finite element basis functions which belong to a finite element space V. In this thesis, a family of *hierarchical* basis functions is used, which was introduced in [58]. In the reference element the following basis functions are defined:

$$N_1(\xi) = \frac{1-\xi}{2};\ N_2(\xi) = \frac{1+\xi}{2};\ N_i(\xi) = \phi_{i-1}(\xi),\ i = 3,4,\ldots,p+1 \tag{4.4}$$

where p is the polynomial degree of the elements and $\xi \in [-1,+1]$. Here ϕ_j is defined in terms of the *Legendre polynomial* P_{j-1}:

$$\phi_j(\xi) = \sqrt{\frac{2j-1}{2}}\int_{-1}^{\xi} P_{j-1}(t)\,dt,\ j = 2,3,\ldots \tag{4.5}$$

The basis functions N_1, N_2 are called *nodal shape functions or external modes*. The basis functions N_i ($i = 3,4,\ldots,p+1$) are called internal shape functions or internal modes,

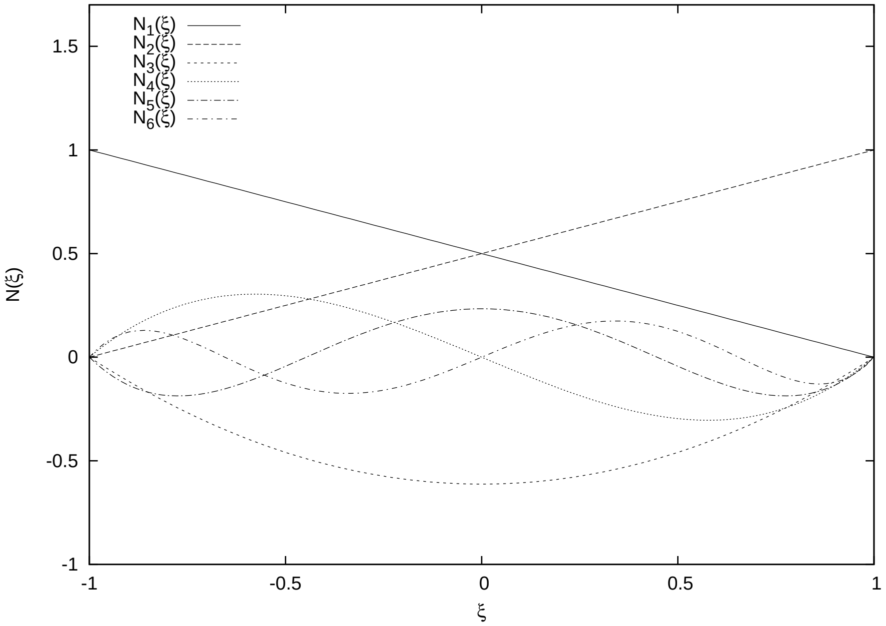

Figure 4.1: One-dimensional basis functions when $p = 5$

sometimes: *bubble modes*. These basis functions are well suited for computer implementation of p-adaptivity because it is easy for us to enhance the accuracy of the solution by adding more hierarchical basis functions on some elements or to reduce the accuracy by dropping several highest order basis functions as appropriate. Some important properties of Legendre polynomials are listed in [58]. In particular, we have:

$$\phi_j(\xi) = \frac{1}{\sqrt{2(2j-1)}}\left(P_j(\xi) - P_{j-2}(\xi)\right). \tag{4.6}$$

With the above formulae, it is easy to evaluate the internal basis functions. Figure 4.1 depicts the first 6 basis functions in the reference element.

As discussed in the previous chapter (see (3.22) to (3.24)), the steady-state 1D Reynolds equation, which is a convection-diffusion equation, can be discretized into the following form using Oden's DG scheme [5]:

$$L(P,v) = a(P,v) - l(P,v) = 0, \ \forall v \in V, \tag{4.7}$$

where

$$a(P,v) = \sum_{e\in\Omega_h}\left(\int_e \varepsilon\frac{\partial P}{\partial X}\frac{\partial v}{\partial X}\,\mathrm{d}X\right) + \sum_{\Gamma_{int}}\left([v]\left\langle\varepsilon\frac{\partial P}{\partial X}\right\rangle - [P]\left\langle\varepsilon\frac{\partial v}{\partial X}\right\rangle\right)$$
$$+\left(v\varepsilon\frac{\partial P}{\partial X}\right)|_{X_{inlet}} - \left(v\varepsilon\frac{\partial P}{\partial X}\right)|_{X_{outlet}} - \left(P\varepsilon\frac{\partial v}{\partial X}\right)|_{X_{inlet}} + \left(P\varepsilon\frac{\partial v}{\partial X}\right)|_{X_{outlet}}, \quad (4.8)$$

and

$$l(P,v) = \sum_{e\in\Omega_h}\left(\int_e \bar{\rho}H\frac{\partial v}{\partial X}\,\mathrm{d}X\right) + \sum_{\Gamma_{int}}[v](\bar{\rho}(P^-)H)$$
$$+(\bar{\rho}Hv)|_{X_{inlet}} - (\bar{\rho}Hv)|_{X_{outlet}} - \left(g_{inlet}\varepsilon\frac{\partial v}{\partial X}\right)|_{X_{inlet}} + \left(g_{outlet}\varepsilon\frac{\partial v}{\partial X}\right)|_{X_{outlet}}. \quad (4.9)$$

In the above equations,

$$P^- = \lim_{\sigma\to 0^+} P(x-\sigma), \text{ for } x\in\Gamma_{int}. \quad (4.10)$$

This provides sufficient upwinding to ensure a stable solution [5]. Note that in equation (4.8) $[v]\langle\varepsilon\frac{\partial P}{\partial X}\rangle$ is nonzero after the integration by parts since v is discontinuous over each element boundary. The continuity condition of P over inter-element boundaries is implemented by weakly imposing

$$\sum_{\Gamma_{int}}[P]\left\langle\varepsilon\frac{\partial v}{\partial X}\right\rangle = 0, \quad (4.11)$$

as part of equation (4.8). Dirichlet boundary conditions are also imposed in a weak form:

$$(P-g_{inlet})\left\langle\varepsilon\frac{\partial v}{\partial X}\right\rangle = 0 \quad (4.12)$$

and

$$(g_{outlet}-P)\left\langle\varepsilon\frac{\partial v}{\partial X}\right\rangle = 0, \quad (4.13)$$

see equations (4.8) and (4.9).

4.2.2 The Film Thickness Equation

The finite difference discretization of the film thickness equation is simple (see Equation (2.35)) and the introduced kernel K_{ij}^{hh} (see Equation (2.36)) can be calculated analytically. However for the high order DG method, things are a little different and a new kernel is introduced for the convenience of calculating the elastic deformation integral. For a given pressure distribution the film thickness may be calculated as follows:

$$\begin{aligned}
H(X) &= H_{00}+\frac{X^2}{2}-\frac{1}{\pi}\int_{X_{in}}^{X_{cav}}\ln|X-X^{'}|P(X^{'})\,\mathrm{d}X^{'} \\
&= H_{00}+\frac{X^2}{2}-\frac{1}{\pi}\sum_{e=1}^{N}\int_{e}\ln|X-X^{'}|P(X^{'})\,\mathrm{d}X^{'} \\
&= H_{00}+\frac{X^2}{2}-\frac{1}{\pi}\sum_{e=1}^{N}\int_{e}\ln|X-X^{'}|\sum_{i=1}^{p^e+1}u_i^eN_i^e(X^{'})\,\mathrm{d}X^{'} \\
&= H_{00}+\frac{X^2}{2}-\frac{1}{\pi}\sum_{e=1}^{N}\sum_{i=1}^{p^e+1}\int_{e}\ln|X-X^{'}|N_i^e(X^{'})\,\mathrm{d}X^{'}u_i^e \\
&= H_{00}+\frac{X^2}{2}-\frac{1}{\pi}\sum_{e=1}^{N}\sum_{i=1}^{p^e+1}K_i^e(X)u_i^e, \qquad (4.14)
\end{aligned}$$

where the kernel values $K_i^e(X)$ are defined by:

$$K_i^e(X)=\int_e\ln|X-X^{'}|N_i^e(X^{'})\,\mathrm{d}X^{'}, \qquad (4.15)$$

which is more complex than the kernel for the finite difference method. These kernels could be calculated analytically though it would be very messy for high order. For this reason, $K_i^e(X)$ is calculated numerically in this work. When X is outside of e, m-point Gaussian quadrature [20, 58] can be used:

$$\begin{aligned}
K_i^e(X) &= \int_e\ln|X-X^{'}|N_i^e(X^{'})\,\mathrm{d}X^{'} \\
&= \frac{h^e}{2}\int_{-1}^{1}\ln|X-X^{'}(\xi)|N_i^e(\xi)\,\mathrm{d}\xi \\
&= \frac{h^e}{2}\sum_{i-1}^{m}(\ln|X-X^{'}(\xi_i)|N_i^e(\xi_i))w_i, \qquad (4.16)
\end{aligned}$$

where $h^e=X_{e+1}-X_e$ is the element size and

$$X^{'}(\xi)=X_e+\frac{h^e}{2}(\xi+1),\ \xi\in[-1,1]. \qquad (4.17)$$

Figure 4.2 indicates the mapping between the reference element and the local element e. When $X\in e$, singular quadrature has to be employed since $\ln|X-X^{'}|$ has a weak

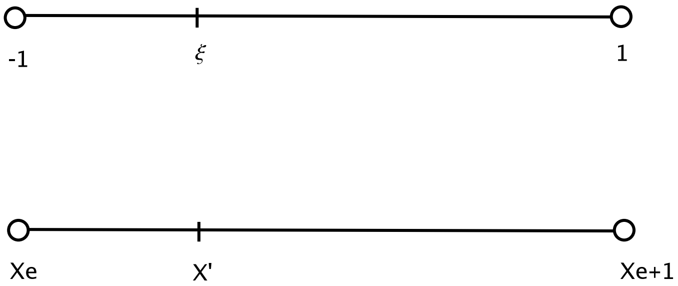

Figure 4.2: Coordinate mapping between the reference element and the local element e

singularity at $X^{'} = X$. We first rewrite $K_i^e(X)$ in the following form:

$$\begin{aligned}
K_i^e(X) &= \int_{X_e}^{X_{e+1}} \ln|X - X^{'}| N_i^e(X^{'})\,\mathrm{d}X^{'} \\
&= \int_{X_e}^{X} \ln|X - X^{'}| N_i^e(X^{'})\,\mathrm{d}X^{'} + \int_{X}^{X_{e+1}} \ln|X - X^{'}| N_i^e(X^{'})\,\mathrm{d}X^{'} \\
&= (X - X_e)\int_0^1 \ln|X - (X + x(X_e - X))| N_i^e(X + x(X_e - X))\,\mathrm{d}x \\
&+ (X_{e+1} - X)\int_0^1 \ln|X - (X + x(X_{e+1} - X))| N_i^e(X + x(X_{e+1} - X))\,\mathrm{d}x \\
&= (X - X_e)\int_0^1 \ln|x(X_e - X)| N_i^e(X + x(X_e - X))\,\mathrm{d}x \\
&+ (X_{e+1} - X)\int_0^1 \ln|x(X_{e+1} - X)| N_i^e(X + x(X_{e+1} - X))\,\mathrm{d}x. \qquad (4.18)
\end{aligned}$$

Note that both integrals in (4.18) can be written in the following general form:

$$S = \int_0^1 f(x)g(x)\,\mathrm{d}x \qquad (4.19)$$

in which $g(x)$ is analytic and $f(x)$ is singular at $x = 0$. Using singular quadrature [20], S can be approximated as follows:

$$S \approx S_n = \sum_{i=1}^{n} T_i \qquad (4.20)$$

where

$$T_i = \int_{x_i}^{x_{i-1}} f(x)g(x)\,\mathrm{d}x, \ (i \geq 1). \qquad (4.21)$$

Here $x_0 = 1$ and $x_n \to 0$ as $n \to \infty$. In practice, the following monotonic decreasing sequence $\{x_n\}$ is usually used:

$$x_n = \theta^n, \ (0 < \theta < 1). \tag{4.22}$$

The values of T_i are calculated using Gaussian quadrature and $\theta = 0.2$ is suggested by [20].

Unfortunately however, numerical evidence suggests that the kernels calculated in the above way are not generally sufficiently accurate. Numerical tests indicate that a smooth film thickness profile can not always be obtained from a smooth pressure distribution if the kernels are calculated using the above method. Consequently this non-smooth film thickness profile will affect the smoothness of the pressure distribution through the Reynolds equation (1.11), particularly in the contact region where the convection term $\frac{\partial(\bar{\rho}H)}{\partial X}$ plays a very important role. In order to obtain more accurate kernels, adaptive Gaussian quadrature is therefore used to compute $K_i^e(X)$ (when X is outside e) and T_i.

Generally, when adaptive m-point Gaussian quadrature is used to compute
$F = \int_{x_1}^{x_2} f(x)\,\mathrm{d}x$, we first calculate F using m-point Gaussian quadrature

$$F = \int_{x_1}^{x_2} f(x)\,\mathrm{d}x \approx F_1 = \frac{x_2 - x_1}{2} \sum_{k=1}^{m} f_k w_k. \tag{4.23}$$

Then the domain $[x_1, x_2]$ is equally divided into two sub-domains, m-point Gaussian quadrature is applied over each sub-domain and a more accurate result will be obtained after summation

$$\begin{aligned} F &= \int_{x_1}^{\frac{x_1+x_2}{2}} f(x)\,\mathrm{d}x + \int_{\frac{x_1+x_2}{2}}^{x_2} f(x)\,\mathrm{d}x \approx \\ F_2 &= \frac{\frac{x_1+x_2}{2} - x_1}{2} \sum_{k=1}^{m} f_k w_k + \frac{x_2 - \frac{x_1+x_2}{2}}{2} \sum_{k=1}^{m} f_k w_k. \end{aligned} \tag{4.24}$$

If $|F_2 - F_1| \le Tol_{convergence}$, let $F = F_2$. If $|F_2 - F_1| > Tol_{convergence}$, keep equally refining the domain until $|F_k - F_{k-1}| < Tol_{convergence}, k = 3,4,5,......$ and let $F = F_k$.

In order to evaluate the integrals in equation (4.8) and (4.9), we need to calculate the values of the film thickness at the quadrature points $X_f^j,\ j = 1,2\ldots,m$ (m is the number of the quadrature points in each element f) and on each element boundary $X_k,\ k = 1,2,\ldots,N+1$. Therefore, the kernel at the quadrature points, $K_i^e(X_f^j)$, and the kernel on the element boundaries, $K_i^e(X_k)$, are required. From (4.15), we can see that $K_i^e(X)$ depends on the structure of the grid used and on the basis functions. Hence, once the grid is fixed and the basis functions are given, $K_i^e(X_f^j)$ and $K_i^e(X_k)$ can be precomputed.

4.2.3 The Force Balance Equation

The force balance equation (1.13) is discretized according to:

$$\sum_{e=1}^{N} \int_e \sum_{i=1}^{p^e+1} u_i^e N_i^e(X)\,\mathrm{d}X - \frac{\pi}{2} = 0. \tag{4.25}$$

By introducing another kernel KK_i^e:

$$KK_i^e = \int_e N_i^e(X)\,\mathrm{d}X, \tag{4.26}$$

the discrete force balance equation can be rewritten as:

$$\sum_{e=1}^{N} \sum_{i=1}^{p^e+1} KK_i^e u_i^e - \frac{\pi}{2} = 0. \tag{4.27}$$

This kernel can also be precomputed given a grid and basis functions.

4.3 Relaxation Method

This section describes a simple solution procedure that may be used on a given mesh and with a given choice of the polynomial degree on each element.

According to (4.3) and (4.7), the discrete Reynolds equation may be written in the general form:

$$L(U) = A(U)U - b(U) = 0, \tag{4.28}$$

where

$$U = \left(u_1^1, \ldots, u_{p^1+1}^1; \ldots; u_1^N, \ldots, u_{p^N+1}^N\right)^T \tag{4.29}$$

are the unknown pressure coefficients. Note that both $A(U)$ and $b(U)$ depend on U. Since the entries of U are ordered element-by-element (see (4.29)), $A(U)$ is a block-tridiagonal matrix and the size of each block is determined by the orders of the current test functions and the basis functions on the corresponding element. Therefore, equation (4.28) can be written in the following form:

$$\begin{bmatrix} A^{1,1} & A^{1,2} & & & & & & \\ A^{2,1} & A^{2,2} & A^{2,3} & & & & & \\ & \ddots & \ddots & \ddots & & & & \\ & & A^{e,e-1} & A^{e,e} & A^{e,e+1} & & & \\ & & & \ddots & \ddots & \ddots & & \\ & & & & A^{N-1,N-2} & A^{N-1,N-1} & A^{N-1,N} \\ & & & & & A^{N,N-1} & A^{N,N} \end{bmatrix} \begin{bmatrix} U^1 \\ \vdots \\ U^{e-1} \\ U^e \\ U^{e+1} \\ \vdots \\ U^N \end{bmatrix} = \begin{bmatrix} b^1 \\ \vdots \\ b^{e-1} \\ b^e \\ b^{e+1} \\ \vdots \\ b^N \end{bmatrix} \tag{4.30}$$

where, for an interior element $1 < e < N$:

$$U^e = \left(u_1^e, u_2^e, \ldots, u_{p^e+1}^e\right), \tag{4.31}$$

$$[A^{e,e-1}]_{i,j} = \left(N_i^e \frac{\varepsilon}{2} \frac{\partial N_j^{e-1}}{\partial X} + N_j^{e-1} \left\langle \varepsilon \frac{\partial N_i^e}{\partial X} \right\rangle \right)_{\Gamma_{e-1,e}}, \tag{4.32}$$

$$\begin{aligned} [A^{e,e}]_{i,j} = \int_e \varepsilon \frac{\partial N_j^e}{\partial X} \frac{\partial N_i^e}{\partial X} \, \mathrm{d}X + \left(N_i^e \frac{\varepsilon}{2} \frac{\partial N_j^e}{\partial X} - N_j^e \left\langle \varepsilon \frac{\partial N_i^e}{\partial X} \right\rangle \right)_{\Gamma_{e-1,e}} \\ + \left(-N_i^e \frac{\varepsilon}{2} \frac{\partial N_j^e}{\partial X} + N_j^e \left\langle \varepsilon \frac{\partial N_i^e}{\partial X} \right\rangle \right)_{\Gamma_{e,e+1}}, \end{aligned} \tag{4.33}$$

$$[A^{e,e+1}]_{i,j} = \left(-N_i^e \frac{\varepsilon}{2} \frac{\partial N_j^{e+1}}{\partial X} - N_j^{e+1} \left\langle \varepsilon \frac{\partial N_i^e}{\partial X} \right\rangle \right)_{\Gamma_{e,e+1}} \tag{4.34}$$

and

$$b^e = \int_e \bar{\rho} H \frac{\partial N_i^e}{\partial X} \, \mathrm{d}X + \left(N_i^e (\bar{\rho}(P^{e-1}) H) \right)_{\Gamma_{e-1,e}} - \left(N_i^e (\bar{\rho}(P^e) H) \right)_{\Gamma_{e,e+1}}. \tag{4.35}$$

In equation (4.30), the right-hand side dominates in the contact region and the left-hand side dominates elsewhere. Note that $A(U)$ in (4.28) is not a diagonally dominant or block diagonally dominant matrix. Furthermore, each entry of $b(U)$ in (4.28) actually depends on all of the u_i^e since each entry of $b(U)$ depends on the values of the local film thickness which consists of a global summation (see equation (4.14)).

Based on the above analysis, the unknown U is relaxed according to:

$$U \leftarrow U + \left(\frac{\partial L(U)}{\partial U}\right)^{-1} R, \tag{4.36}$$

where R is the numerical residual of the discrete Reynolds equation and $\frac{\partial L}{\partial U}$ is approximated by:

$$\begin{aligned} \frac{\partial L(U)}{\partial U} &= \frac{\partial}{\partial U}\left(A(U)U\right) - \frac{\partial b(U)}{\partial U} \\ &\approx A(U) - \frac{\partial b(U)}{\partial U}. \end{aligned} \tag{4.37}$$

Numerical experiments indicate that (4.37) provides the basis for a sufficiently robust smoother. In fact, equation (4.37) can be viewed as a generalization of equation (2.41). When using finite differences, the discrete system (2.34) can also be written in the following form:

$$L(P) = A(P)P - b(P) = 0 \tag{4.38}$$

where $A(P)$ is a tridiagonal matrix:

$$\begin{aligned} A_{i,i-1} &= \varepsilon_{i-\frac{1}{2}} \\ A_{i,i} &= -(\varepsilon_{i-\frac{1}{2}} + \varepsilon_{i+\frac{1}{2}}) \\ A_{i,i+1} &= \varepsilon_{i+\frac{1}{2}} \end{aligned} \tag{4.39}$$

and

$$b_i = \frac{\bar{\rho}_i H_i - \bar{\rho}_{i-1} H_{i-1}}{h}. \tag{4.40}$$

In this case P can be updated by:

$$\begin{aligned} P &\leftarrow P + \left(\frac{\partial L}{\partial P}\right)^{-1} R \\ &= P + \left(\frac{\partial}{\partial P}(A(P)P - b(P))\right)^{-1} R \\ &\approx P + \left(A(P) - \frac{\partial b(P)}{\partial P}\right)^{-1} R \end{aligned} \tag{4.41}$$

where R is the numerical residual. Note that $A(P)$ in (4.38) is a diagonally dominant matrix and it is acceptable to approximate it using a diagonal matrix $\tilde{A}$ for which

$$\tilde{A}_{i,i} = -(\varepsilon_{i-\frac{1}{2}} + \varepsilon_{i+\frac{1}{2}}). \tag{4.42}$$

As discussed in [60], the film thickness heavily depends on the local pressures and less on the pressures far away. Hence the full matrix $\frac{\partial b(P)}{\partial P}$ can also be replaced by a diagonal matrix for which

$$\frac{\partial \tilde{b}(P)}{\partial P}_{i,i} = \frac{1}{\pi}\frac{\bar{\rho}_i K^{hh}_{i,i} - \bar{\rho}_{i-1} K^{hh}_{i-1,i}}{h}. \tag{4.43}$$

As a result, $\frac{\partial L}{\partial P}$ can be approximated by (2.41). However, when using more grid points, the film thickness heavily depends on more local pressures. In this case it is not a good approximation to $\frac{\partial b(P)}{\partial P}$, using a diagonal matrix. In such a case the relaxation method may not be powerful enough, even with multigrid acceleration. This is why the under-relaxation factors have to be smaller with increasing numbers of grid points when using Gauss-Seidel relaxation and the distributive Gauss-Seidel relaxation is more robust [60].

In order to improve the efficiency of the relaxation that follows from equation (4.37), $\frac{\partial b(U)}{\partial U}$ is approximated by a full matrix according to (4.9):

$$\begin{aligned}
\left[\frac{\partial b(U)}{\partial U}\right]_{I,J} &= \frac{\partial b(U)^e_i}{\partial U^f_j} \\
&= \sum_{e\in\Omega_h}\left(\int_e \bar{\rho}\frac{\partial H^e(X)}{\partial U^f_j}\frac{\partial v}{\partial X} + \frac{\partial\bar{\rho}}{\partial U^f_j}H^e(X)\frac{\partial v}{\partial X}\,\mathrm{d}X\right) \\
&+ \sum_{\Gamma_{int}}\left([v]\left\langle\bar{\rho}(P^-)\frac{\partial H}{\partial U^f_j}\right\rangle + [v]\left\langle\frac{\partial\bar{\rho}(P^-)}{\partial U^f_j}H\right\rangle\right) \\
&+ \left(\bar{\rho}\frac{\partial H}{\partial U^f_j}v\right)|_{X_{inlet}} - \left(\bar{\rho}\frac{\partial H}{\partial U^f_j}v\right)|_{X_{outlet}},
\end{aligned} \tag{4.44}$$

where the Ith row corresponds to the row generated with the test function $v = N^e_i(X)$ and the Jth column corresponds to the unknown U^f_j. According to the discrete film thickness equation (4.14),

$$\frac{\partial H(X)}{\partial U^f_j} = K^f_j(X), \tag{4.45}$$

which may be precomputed to improve computational efficiencies.

It is important to note that the elastic deformation is more sensitive to the local pressures. That is to say, in (4.45), $K^f_j(X)$ is relatively small when the position of f is far away from the position X, which gives us very useful information to make further simplification to $\frac{\partial b(U)}{\partial U}$. Here we use the following principles:

1. Assuming X is inside element e, let $\frac{\partial H(X)}{\partial U_j^f} = 0$ if $f \neq e$ and f is not a neighbour of e.
2. Assuming $X = \Gamma_{int}$, let $\frac{\partial H(X)}{\partial U_j^f} = 0$ if f is not a neighbour of Γ_{int}.
3. $\frac{\partial H(X_{inlet})}{\partial U_j^f} = 0$ if $f \neq 1$ and $\frac{\partial H(X_{outlet})}{\partial U_j^f} = 0$ if $f \neq N$.
4. $\frac{\partial H(X)}{\partial U_j^f} = K_j^f(X)$, otherwise.

The above principles lead to the fact that $\frac{\partial b(U)}{\partial U}$ may be approximated by a block tridiagonal matrix which is of the same structure as $A(U)$. As a result, $L(U)$ is also a block tridiagonal matrix. The advantage of this simplification is that we just need to evaluate a relatively small number of the entries of $\frac{\partial b(U)}{\partial U}$ instead of calculating all of them.

When updating the unknown U in (4.36), we solve the following linear system numerically instead of calculating $\left(\frac{\partial L}{\partial U}\right)^{-1}$:

$$\frac{\partial L}{\partial U} U_{correction} = R, \tag{4.46}$$

where U is the current solution and $U_{correction}$ is the correction value to U. There are many methods which can be used to solve this linear system. Since we usually have a quite small number of degrees of freedom when using high order DG to solve EHL problems in 1D and our approximation to $\frac{\partial L}{\partial U}$ is block-tridiagonal, traditional Gaussian-Elimination is efficient for the above linear system. With the obtained $U_{correction}$, U is updated by:

$$U = U + C_1 U_{correction}, \tag{4.47}$$

where C_1 is an under-relaxation factor for pressure.

This relaxation method has the following advantages.

1. We use a uniform relaxation method over the entire computational domain, which is more straightforward compared to the relaxation method for the finite difference method proposed by Venner [60], for which the pressure is relaxed using simple Gauss-Seidel relaxation when the diffusion term of the Reynolds equation dominates and using the distributive Gauss-Seidel relaxation introduced by Venner when the convection term dominates. The new method is easy to implement since we do not have to adjust the relaxation method in different regions.

2. The new method is more robust than Gauss-Seidel like relaxations. When using finite difference methods for EHL problems, we have to use multigrid to enhance the efficiency and the robustness of the convergence if Gauss-Seidel like relaxations are employed. This is because the effect of the Gauss-Seidel like relaxations is too "local" to handle the "global" relation between the film thickness and the pressure. Unfortunately, particularly in the contact region, the film thickness plays such an important role that it dominates the high nonlinearity of the discrete Reynolds equation. Hence it is not possible to obtain converged numerical solutions using the Gauss-Seidel like relaxations and a single grid for highly loaded cases. The robustness of convergence can be significantly improved by using multigrid since both of the high frequency error and the low frequency error can be eliminated efficiently. But if only the simple Gauss-Seidel relaxation method is used on each level, it is still not robust enough for highly loaded cases when many grid points are employed. This is because the smoother becomes more "local" as the number of grid points increases. This difficulty can be overcome by the distributive Gauss-Seidel relaxation [60], but of course the multigrid method still has to be employed. The DG smoother discussed above is still a little "local" since we let $\frac{\partial H(X)}{\partial U_j^f} = 0$ when f is far away from the position X. However for high order DG, it is robust enough to approximate the global relation between the film thickness and the pressure by just counting in the neighbouring elements' contribution to $H(X)$ because the mesh sizes for high order DG are normally quite large compared to those for finite differences. Hence correction values are solved simultaneously from the resulting system. Thus our DG smoother is much more "global" than the Gauss-Seidel like relaxations.

In order to satisfy the force balance equation, we update the reference thickness H_{00} as follows:

$$H_{00} \leftarrow H_{00} - C_2\Big(\frac{\pi}{2} - \sum_{e=1}^{N}\sum_{i=1}^{p^e+1} KK_i^e u_i^e\Big), \tag{4.48}$$

where $C_2 \in [0.01, 0.1]$ is the under-relaxation factor for H_{00}.

4.4 Cavitation

As already mentioned in Chapter 2, the Reynolds equation alone allows the pressure to decrease without any limit. Negative pressures might therefore appear in the outlet region. We have to handle this separately since it is not physically possible and must therefore be prevented. As a result, the right boundary becomes a free boundary, which is sometimes called the cavitation boundary.

Using finite differences, the cavitation condition is sometimes treated by simply forcing the negative pressures to be zero [25]. As a result, at the cavitation position, $P = 0$, the requirement of $\frac{\partial P}{\partial X} = 0$ may not be generally satisfied.

In order to test the accuracy of the high order DG scheme, numerical tests are undertaken using two different approaches to the cavitation boundary. In the first of these the boundary position is captured by slightly moving the grid until, on the rightmost boundary, $P = 0$ and $\frac{\partial P}{\partial X} = 0$. Since in each element the pressure is expressed as a high order polynomial, it is easy to evaluate $\frac{\partial P}{\partial X}$ on the rightmost boundary.

Secondly, another method, known as the “Penalty Method”, introduced by Wu and Oden [64], is also employed to handle the cavitation condition. A penalty term is added into the Reynolds equation, which forces the negative pressures to be zero in a weak form. Both $P = 0$ and $\frac{\partial P}{\partial X} = 0$ at the cavitation position can be weakly satisfied. For the penalty method, we do not need to move the grid, but the computational domain should be large enough to make sure that the cavitation position is located inside it. The cavitation position can be captured automatically with the penalty method, but the accuracy of it depends on the local mesh size and the order of the local basis functions.

4.4.1 Moving Boundary

Since the Reynolds equation is only valid in the pressurised region where $P \geq 0$, here we find the pressurised region by moving the grid. This re-positioning of the computational domain ensures the pressure distribution calculated from the Reynolds equation is physically reasonable.

During computation, either of the cases depicted in Figure 4.3 might happen. Note that both of the pictures in Figure 4.3 show that $P \approx 0$ on the right boundary since the Dirichlet boundary condition has been implemented weakly in the discrete form of the Reynolds equation . But $\frac{\partial P}{\partial X} > 0$ in the left picture and $\frac{\partial P}{\partial X} < 0$ in the right one. Since $\frac{\partial P}{\partial X} = 0$ is required on the right boundary (see Figure 4.4), apparently both of the right boundaries shown in Figure 4.3 need to be adjusted. In the left picture, the grid should be moved to the left since the position where $\frac{\partial P}{\partial X} = 0$ should be somewhere left of the current boundary. In the second case, the grid should be moved in the opposite direction.

The whole procedure driving the grid-moving method is as follows.

1. Give an initial grid (possibly non-uniform). Ensure that there are sufficient elements and the elements are appropriately spaced to capture all of the features, particularly

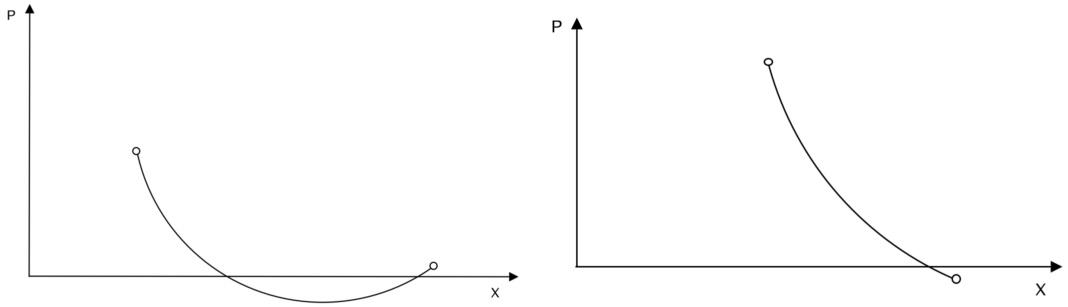

Figure 4.3: Possible pressure profiles on the rightmost element

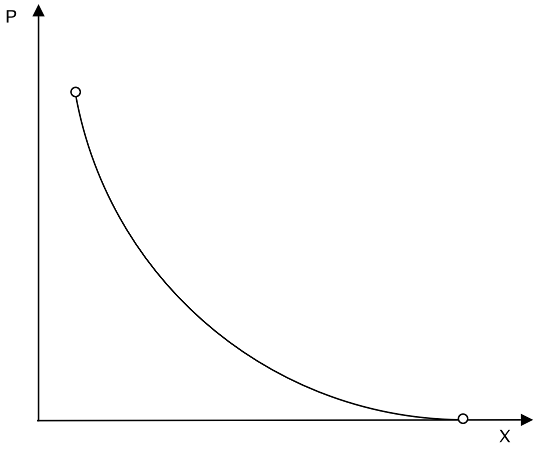

Figure 4.4: Desired pressure profile on the rightmost element

the pressure spike.

2. Fix the orders of the basis functions on each element, which can be different from one element to another.

3. Precompute $K_i^e(X)$ on each quadrature point and at element boundary points. These will be used to evaluate the film thickness at each quadrature point and element boundary. The KK_i^e are also precomputed to calculate the global integral in the force balance equation.

4. Give an initial guess for pressure distribution. Typically, we employ a Hertzian dry contact profile. Note that here we only initialize the first two unknowns U_1^e and U_2^e for each element e and $U_i^e = 0$ if $i \geq 2$. Figure 4.5 shows an initial guess for pressure.

5. Calculate the values of the film thickness at all of the quadrature points and the element boundaries according to the discrete film thickness equation (4.14).

6. Update U using the nonlinear smoother developed above.

7. Correct H_{00} using equation (4.48).

8. Move the grid according to the value of $\frac{\partial P}{\partial X}$ at the right boundary. Here we use $\triangle X = -C\frac{\partial P}{\partial X}$ to control the distance and the direction of the movement, where C is a positive constant. As we can see here, the grid will be moved to the left when $\frac{\partial P}{\partial X} > 0$ and to the right when $\frac{\partial P}{\partial X} < 0$.

9. Repeat this procedure from 5 until the residual R is very small and $\frac{\partial P}{\partial X} = 0$ on the right boundary.

Although both of $\frac{\partial P}{\partial X}|_{cavitation position} = 0$ and $P|_{cavitation position} = 0$ are finally satisfied, there are still some disadvantages:

1. It is important that the predefined grid is fine enough, and the order of the basis functions on each element is high enough, to capture all of the features accurately during the movement, particularly the pressure spike. However in practice, given a certain loaded case, we do not exactly know where the spike region is. So usually it is hard to predefine an appropriate grid.

2. The magnitude of the movement of the grid has to be limited to ensure convergence. This slows down the global convergence.

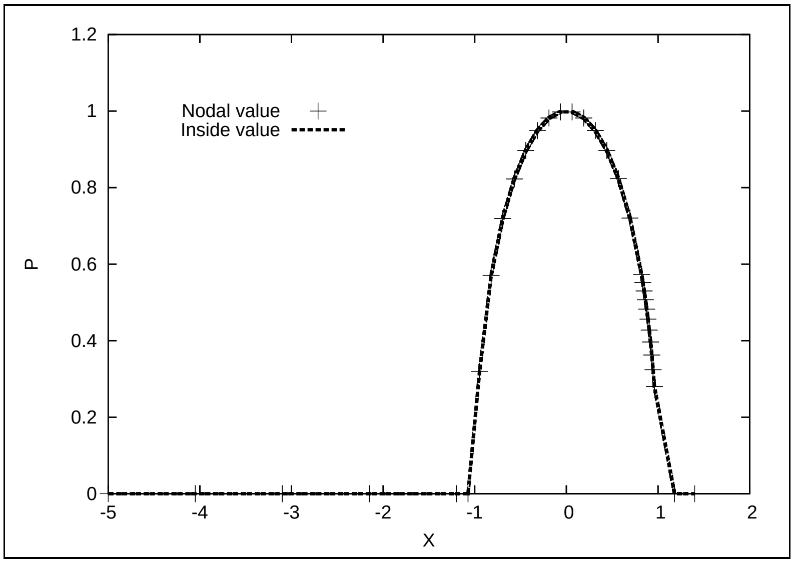

Figure 4.5: Initial pressure distribution based upon a linear interpolant of the Hertz dry contact profile.

3. In the 2D case, this grid-moving method is not applicable since the cavitation free boundary is not a point, but an unknown curve.

The above disadvantages strongly limit the application of this method. So in this thesis, it is only employed in this chapter for accuracy comparison purposes.

4.4.2 Penalty Method

An alternative to the moving-grid method is the Penalty method which was introduced by Wu and Oden [64] in 1986 and was successfully applied to the nonlinear *EHL* Reynolds-Hertz problem to handle the free boundary for incompressible lubrication problems.

By introducing an exterior penalty term, the following nonlinear system will be solved instead of (4.7):

$$L(P,v) = a(P,v) + \frac{1}{\delta} \sum_{e \in \Omega_h} \int_e P_- v \, \mathrm{d}X - l(P,v) = 0, \tag{4.49}$$

where δ is an arbitrary small positive number and

$$P_- = min(P,0). \tag{4.50}$$

Note that the penalty term $\frac{1}{\delta}\sum_{e\in\Omega_h}\int_e P_- v\,\mathrm{d}X$ is not effective where $P \geq 0$. In the outlet region, the penalty term dominates the equation (4.49) when $P < 0$, provided that the δ is small enough. In this case, the negative pressures are forced to be zero by the penalty term in the weak form. As can be seen, we do not need to do anything else besides taking into account the penalty term when discretizing the Reynolds equation. The condition of $P \geq 0$ over the entire computational domain can be satisfied automatically and the cavitation position is some determinable position in the outlet region where both $P = 0$ and $\frac{\partial P}{\partial X} = 0$ are weakly satisfied.

Equation (4.49) can be written in the same general nonlinear form as (4.28):

$$L(U) = A(U)U - b(U) = 0. \tag{4.51}$$

Note that $A(U)$ in (4.51) incorporates the penalty term and $A(U)$ remains a block tridiagonal matrix.

The penalty method has the following main advantages over the moving-grid method discussed above:

1. It is very easy to implement. The only thing we need to do is to add an extra term into the Reynolds equation.
2. We do not need to move the grid during computation (but the computational domain is required to be large enough to ensure the actual cavitation position is located inside it).
3. On the free boundary, both $P = 0$ and $\frac{\partial P}{\partial X} = 0$ are satisfied weakly and automatically.
4. The penalty method is also well-suited to the point contact problems for which the grid-moving method is non-applicable.

4.5 Adaptivity

When using finite differences to solve EHL problems, it is typical to adopt uniform grids since the multigrid and the multilevel multi-integration are applied most easily on uniform grids. The only thing we can do to improve the accuracy is to increase the number of grid points, which leads to high expense. However for high order DG, h-adaptivity is easily applicable since we do not use any additional techniques such as multigrid or multilevel multi-integration to improve the robustness of the relaxation and accelerate the computation.

In fact, in order to obtain accurate DG solutions of EHL problems, it is more efficient to use h-adaptivity. As *EHL* problems cover a large range of loaded cases, the pressure distribution and the film thickness profile varies greatly with different loads. As a result,

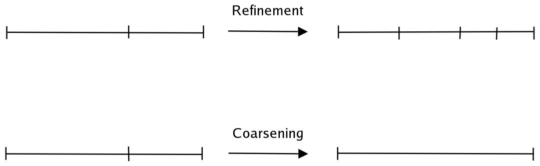

Figure 4.6: Refinement and coarsening

it is hard to predefine a suitable non-uniform grid given a specific loaded case. Hence automatic h-adaptivity emerges to be very important. In this section, two alternative h-adaptivity strategies are considered.

4.5.1 H-adaptivity Based on Discontinuity

Here an automatic h-adaptivity method is developed which can capture all of the features of EHL solutions with a small number of elements. In order to adjust the grid according to the current solution, we need a criterion to judge whether the local mesh needs to be refined or coarsened. As has been described, DG solutions are discontinuous over the element boundaries. The magnitude of the discontinuity can be reduced by local mesh refinement. Based on this property of DG, we use the magnitude of the discontinuity on the element boundaries as the criterion for h-adaptivity. The basic idea is as follows.

1. Suppose we have two neighbouring elements e and f which share an element boundary Γ_{ef}. If $|P_e - P_f|_{\Gamma_{ef}} > Tol_1$ where Tol_1 is a given tolerance, refine both e and f by splitting each of them into two equally spaced smaller elements. See the upper case in Figure 4.6.

2. If $|P_e - P_f|_{\Gamma_{ef}} < Tol_2$ where $Tol_2 \ll Tol_1$ is also a given tolerance, agglomerate e and f to be one larger element. See the lower case in Figure 4.6.

Here the quality of the numerical solution can be ensured by the h-adaptivity which can make all of the discontinuities smaller than Tol_1.

The relaxation procedure combined with h-adaptivity and the penalty method is as follows:

1. Give an initial grid and ensure that this grid covers the pressurised domain. That is to say, the left boundary of the given grid is required to be far away from the contact centre and the actual cavitation position should be inside the given grid.

2. Initialize the pressure on the given grid (see (4.5)) and calculate K_i^e and KK_i^e.

3. Give two tolerances Tol_1 and $Tol_2 \ll Tol_1$ for h-adaptivity.

4. Update the pressure on the current grid using the nonlinear smoother introduced above (4.36) until the pressure does not change too much.
5. Calculate all of the discontinuities over the element boundaries. Then adjust the grid according to the above h-adaptivity criterion.
6. Transfer the current pressure profile from the old grid onto the new grid if the grid has been adjusted.
7. Recalculate K_i^e and KK_i^e.
8. Repeat from 4 until the grid does not need to be adjusted any more and the numerical residual is smaller than some final converged value ($\mathcal{O}10^{-11}$) is used in this thesis).

The discontinuity on the boundary between e and $e+1$ can be cheaply calculated by:

$$Discontinuity_{\Gamma_{e,e+1}} = |u_1^{e+1} - u_2^e| \tag{4.52}$$

because u_2^e equals the pressure on the right boundary of e and u_1^{e+1} is the pressure on the left boundary of $e+1$.

Figure 4.7 shows an example of the history of the h-adaptivity around the pressure spike in a certain high loaded case ($U = 1.0 \times 10^{-11}$, $W = 1.0 \times 10^{-4}$ and $G = 5000$), where $Jump_{max}$ and N are the maximum pressure jump over the entire domain and the number of elements respectively. Note that the grid is changed by both local grid refinement and local grid coarsening and the order of the basis functions is $p^e = 8$ everywhere. With the initial grid in Figure 4.7 (a) discontinuities over the element boundaries around the pressure spike can be observed, which indicates that the local grid needs to be adjusted. From Figure 4.7 (b) to (h) the local elements around the pressure spike has been refined and the mesh in the smooth region has been coarsened. Finally, an appropriate mesh is obtained in Figure 4.7 (h) and the steep pressure spike is captured much more accurately on the resulting grid than on the initial grid without increasing the number of degrees of freedom significantly. This is the main advantage of h-adaptivity.

4.5.2 H-Adaptivity Based on High-Order Components

In the previous subsection a very simple h-adaptivity method was developed. This triggered local refinement based on the magnitude of the discontinuities in pressure over element interfaces (since the target was to obtain a sufficiently smooth pressure profile).

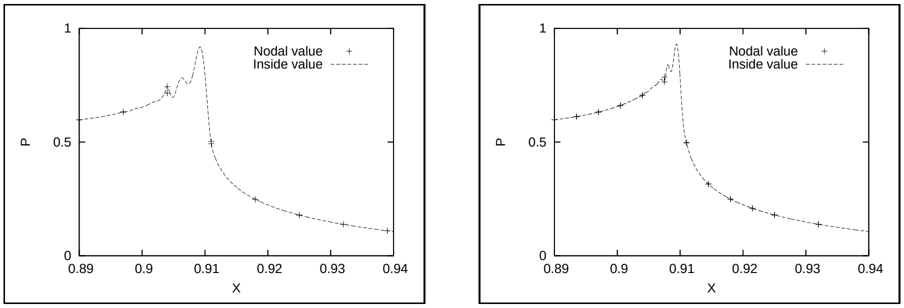

(a) $Jump_{max} = 0.0289759, N = 36$ (b) $Jump_{max} = 0.0212322, N = 35$

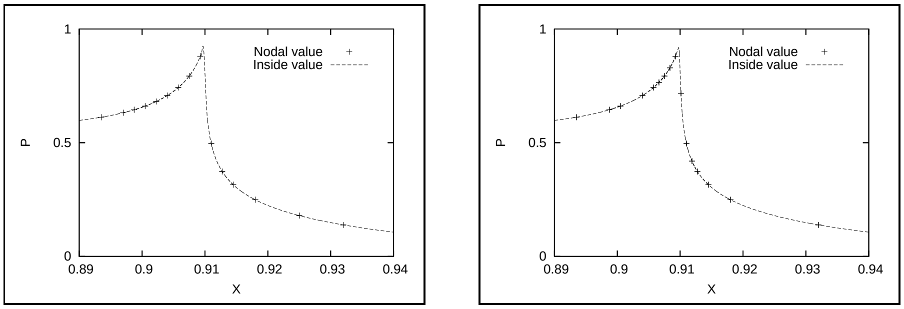

(c) $Jump_{max} = 0.0011343, N = 32$ (d) $Jump_{max} = 0.0006125, N = 30$

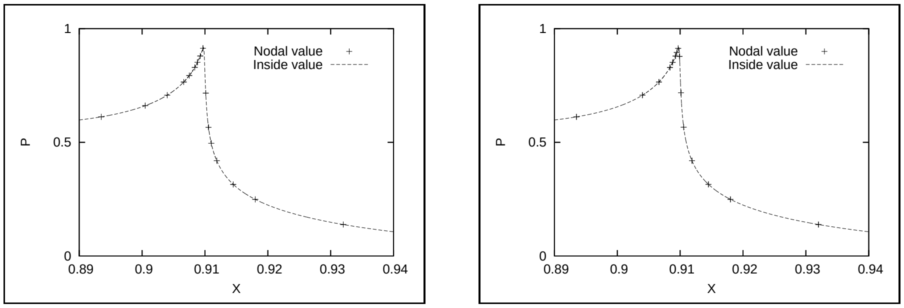

(e) $Jump_{max} = 0.0001636, N = 30$ (f) $Jump_{max} = 0.0000107, N = 27$

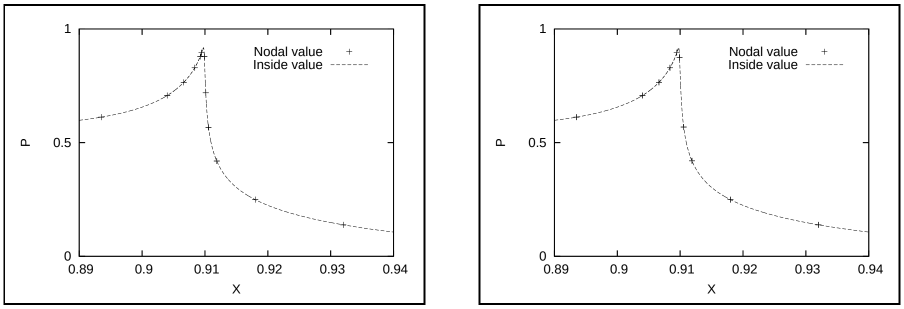

(g) $Jump_{max} = 0.0000107, N = 23$ (h) $Jump_{max} = 0.0000864, N = 21$

Figure 4.7: History of the h-adaptivity based on the discontinuities in the spike region when $U = 1.0 \times 10^{-11}$, $W = 1.0 \times 10^{-4}$ and $G = 5000$

e	5	8	15	16
u_1	0.5328185952	0.6944287943	0.8649104162	0.7426089370
u_2	0.8067864536	0.5768638476	0.7426088624	0.6030807685
u_3	-0.0451199503	0.0040050361	0.0030824574	0.0240525447
u_4	0.0079280043	0.0052016457	0.0038435210	-0.0039836946
u_5	-0.0017316450	0.0019679464	-0.0010204973	0.0003895965
u_6	0.0003682077	0.0005942727	0.0000578894	0.0000364659
u_7	-0.0000647246	0.0001960444	0.0000340746	-0.0000324751
u_8	0.0000074255	0.0000342904	-0.0000106300	0.0000109820
u_9	0.0000054348	0.0000234168	0.0000010894	-0.0000025932

Table 4.1: Values of u_e^i

However, following some preliminary numerical experiments, this method is found to be insufficiently robust for transient line contact problems (see chapter 5). This is because the magnitude of the discontinuities between neighbouring elements does not fully represent the degree of the accuracy of the numerical solution. Furthermore, for time-dependent problems, it is always a challenge to control the global error since a sequence of solutions are required and the errors generated at the previous time steps will of course affect the quality of the later numerical solutions. In this section, an alternative h-adaptivity method is therefore developed and tested on steady-state problems based on the properties of the high order basis functions used for the DG approximation. This approach will also be applied to the transient problems considered in the next chapter.

The finite element functions, N_i^e, used in this work are the hierarchical basis functions described in [58] (see 4.2). Numerical experiments suggest that the high order coefficients u_i^e, corresponding to the higher order basis functions, are usually very small when an accurate, converged solution is obtained. When the local order of the basis functions is not sufficiently high, or the local mesh is not fine enough, these high order coefficients are relatively large and the resulting solution is not sufficiently accurate. The values of u_i^e in four different elements (5, 8, 15 and 16) of the converged solution shown in Figure 4.10 are displayed in Table 4.1. Based upon this observed property of the basis functions, an h-adaptivity method has been implemented as described below. Note that in this work we use the same order of element over the entire domain, however more generality is certainly possible.

The basic principle behind the adaptivity is summarized as follows:

1. Refine any element on which the solution has too large a contribution from the highest order basis functions. Here we give a small tolerance $Tol_{refine} = 0.001$ say. If either of the last two high order coefficients ($u_{p^e}^e$ and $u_{p^e+1}^e$) is greater than

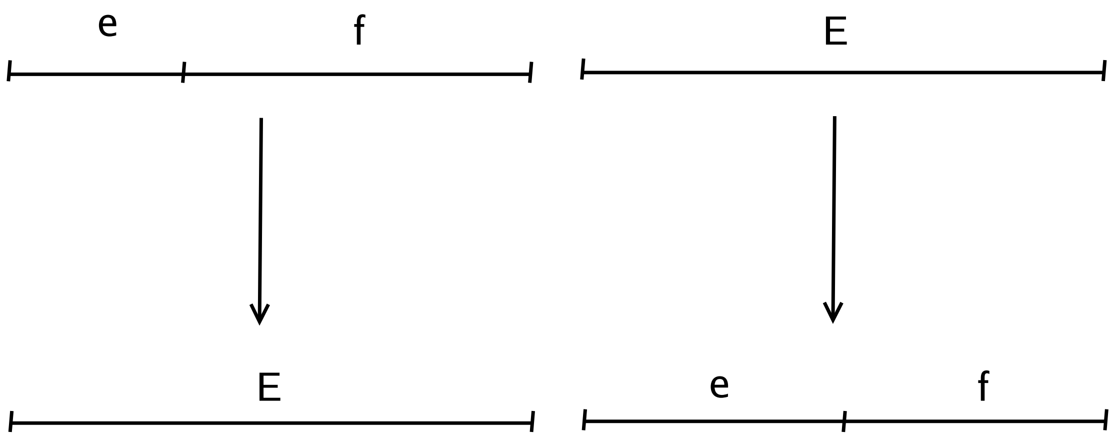

(a) Use I_f^c to transfer data from $e+f$ to E (b) Use I_c^f to transfer data from E to $e+f$

Figure 4.8: Data transfer between grids

Tol_{refine}, divide the element e to be two equally spaced smaller elements.

2. Agglomerate two neighbouring elements to be a larger one (the details of the data transfer will be given later) if the local solution is sufficiently smooth. Here, for every pair of neighbouring elements (for example e and $e+1$), we agglomerate them to be a larger trial element E and interpolate the local solution onto the trial element. If both of the coefficients $u_{p^E}^E$ and $u_{p^E+1}^E$ are less than another tolerance $Tol_{coarsen} = 0.0005(say) < Tol_{refine}$, take E as the new local mesh element to replace e and $e+1$.

4.5.3 Data Transfer

Once the grid is changed during computation, U needs to be transferred from the original grid onto the new grid. This includes two cases: transferring data from two finer elements to a coarser element (see 4.8 (a)) and transferring data from a coarser element to two finer elements (see 4.8 (b)). We now define two transfer operators: I_f^c and I_c^f to transfer data from finer mesh to coarser mesh and from coarser mesh to finer mesh respectively.

The I_f^c, for which we can write

$$I_f^c \begin{bmatrix} u^e \\ u^f \end{bmatrix} = \begin{bmatrix} \left(I_f^c\right)^e & \left(I_f^c\right)^f \end{bmatrix} \begin{bmatrix} u^e \\ u^f \end{bmatrix} = u^E, \tag{4.53}$$

can be found by enforcing the following weak form

$$\int_E P^E(X) v \mathrm{d}X = \int_{e+f} P^{e+f}(X) v \mathrm{d}X, \ \forall v \in \{N_i^E(X)\}, \tag{4.54}$$

where $P^E(X)=\sum_{i=1}^{p^E+1} u_i^E N_i^E(X)$ is the pressure in E, $P^{e+f}(X)$ is the pressure in $e+f$ and

$$\begin{aligned} u^e &= (u_1^e, u_2^e, \ldots, u_{p^e+1}^e)^T && (4.55)\\ u^f &= (u_1^f, u_2^f, \ldots, u_{p^f+1}^f)^T. && (4.56) \end{aligned}$$

Note that $P^{e+f} = P^e = \sum_{i=1}^{p^e+1} u_i^e N_i^e(X)$ when $X \in e$ and $P^{e+f} = P^f = \sum_{i=1}^{p^f+1} u_i^f N_i^f(X)$ when $X \in f$. Using n point Gaussian quadrature, equation (4.54) becomes

$$\sum_{k=1}^{n} (P^E(X)v)_k w_k = \sum_{k=1}^{n} (P^{e+f}(X)v)_k w_k,\ \forall v \in \{N_i^E(X)\}, \tag{4.57}$$

$$\begin{aligned} \sum_{k=1}^{n}(\sum_{j=1}^{p^E+1} u_j^E N_j^E(X_k)N_i^E(X_k))w_k &= \sum_{X_k\in e}(\sum_{j=1}^{p^e+1} u_j^e N_j^e(X_k)N_i^E(X_k))w_k\\ &+ \sum_{X_k\in f}(\sum_{j=1}^{p^f+1} u_j^f N_j^f(X_k)N_i^E(X_k))w_k,\\ & i=(1,\ldots,p^E+1). && (4.58) \end{aligned}$$

Here we define:

$$\begin{aligned} \mathscr{M}_{ij} &= \sum_{k=1}^{n} N_j^E(X_k)N_i^E(X_k)w_k && (4.59)\\ \mathscr{N}_{ij}^e &= \sum_{X_k\in e} N_j^e(X_k)N_i^E(X_k)w_k && (4.60)\\ \mathscr{N}_{ij}^f &= \sum_{X_k\in f} N_j^f(X_k)N_i^E(X_k)w_k, && (4.61) \end{aligned}$$

which allows (4.58) to be expressed as

$$\mathscr{M} u^E = \mathscr{N}^e u^e + \mathscr{N}^f u^f. \tag{4.62}$$

That is,

$$u^E = \mathscr{M}^{-1}\mathscr{N}^e u^e + \mathscr{M}^{-1}\mathscr{N}^f u^f, \tag{4.63}$$

where

$$u^E = (u_1^E, u_2^E, \ldots, u_{p^E+1}^E). \tag{4.64}$$

Therefore,

$$I_f^c = \begin{bmatrix} (I_f^c)^e & (I_f^c)^f \end{bmatrix} \tag{4.65}$$

$$= \begin{bmatrix} \mathscr{M}^{-1}\mathscr{N}^e & \mathscr{M}^{-1}\mathscr{N}^f \end{bmatrix}. \tag{4.66}$$

When one element E is divided into two small elements e and f we can calculate u^e and u^f separately. For example, to calculate u^e we enforce

$$\int_e P^E(X)v\mathrm{d}X = \int_e P^e(X)v\mathrm{d}X,\ \forall v \in \{N_i^e(X)\}. \tag{4.67}$$

Substituting (4.3) to (4.67), we have

$$\int_e (\sum_{j=1}^{p^E+1} u_j^E N_j^E(X))v\mathrm{d}X = \int_e (\sum_{j=1}^{p^e+1} u_j^e N_j^e(X))v\mathrm{d}X,\ \forall v \in \{N_i^e(X)\}. \tag{4.68}$$

Hence

$$u^e = \mathscr{A}^{-1}\mathscr{B}u^E, \tag{4.69}$$

where

$$\mathscr{A}_{ij} = \int_e N_j^e(X)N_i^e(X)\mathrm{d}X \tag{4.70}$$

$$\mathscr{B}_{ij} = \int_e N_j^E(X)N_i^e(X)\mathrm{d}X. \tag{4.71}$$

Clearly u^f can be calculated in the same way,

$$u^f = \mathscr{C}^{-1}\mathscr{D}u^E, \tag{4.72}$$

where

$$\mathscr{C}_{ij} = \int_f N_j^f(X)N_i^f(X)\mathrm{d}X \tag{4.73}$$

$$\mathscr{D}_{ij} = \int_f N_j^E(X)N_i^f(X)\mathrm{d}X. \tag{4.74}$$

Therefore,

$$\begin{bmatrix} u^e \\ u^f \end{bmatrix} = I_c^f u^E, \tag{4.75}$$

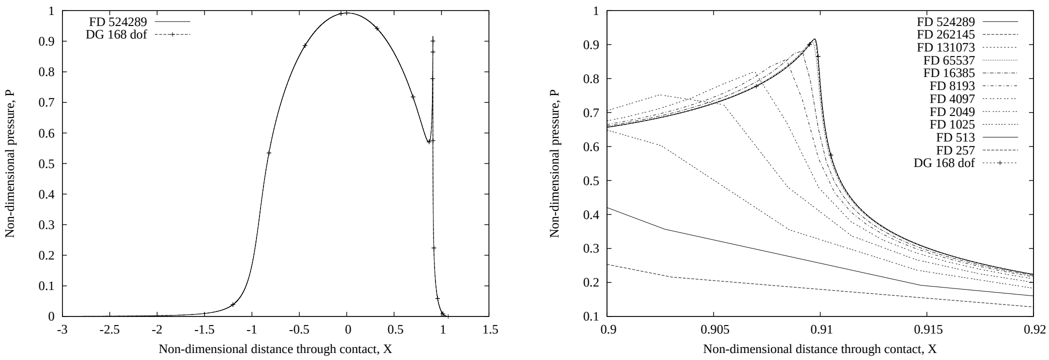

Figure 4.9: Pressure distributions obtained using DG and FD methods across the entire contact, left, and around the pressure spike, right

where

$$I_c^f = \begin{bmatrix} \mathscr{A}^{-1}\mathscr{B} \\ \mathscr{C}^{-1}\mathscr{D} \end{bmatrix}. \tag{4.76}$$

4.6 Numerical Results

This section begins by describing a typical numerical experiment that demonstrates the high accuracy of the DG method by comparing solutions for a high load test problem ($U = 1.0 \times 10^{-11}$, $W = 1.0 \times 10^{-4}$ and $G = 5000$) against those obtained using a standard multi-level, multi-integration FD algorithm. It is shown in [27] that in order to fully resolve the pressure spike up to half a million FD grid-points may be required. Here we compare our DG results against increasing resolutions of FD grids. For the DG solution 16 elements are used (not of equal size) and the polynomial degree is either 10 (in the pressure spike region) or 8 (elsewhere). Figure 4.9 shows the pressure profile computed for a typical highly loaded case. The entire contact is shown in the left graph whilst a detailed view of the position of the pressure spike is shown on the right. Note that the finite difference results used for comparison have been provided by Dr C.E. Goodyer. The key features of interest are the peak value of pressure, its position and the point at which the free boundary occurs. These values are shown in Table 4.2. It is clear from these results that the DG solution matches the converged finite difference solution very closely indeed. There is clearly excellent agreement between the two solutions although the DG solution requires a tiny fraction of the number of unknowns needed for the FD solution.

In the above example, the moving-grid strategy is used without h-adaptivity (so the finite element grid has been carefully selected *a priori*). We now solve the same loaded case using the automatic h-adaptivity method based on the discontinuities along with the

Method	Unknowns	Peak Pressure	Peak Position	Free Boundary Position
FD	4097	0.8212	0.9069	1.0693
FD	8193	0.8566	0.9084	1.0701
FD	16385	0.8810	0.9092	1.0704
FD	65537	0.9095	0.9066	1.0705
FD	131073	0.9138	0.9097	1.0707
FD	262145	0.9158	0.9097	1.0706
FD	524289	0.9164	0.9097	1.0706
DG FE	168	0.91646	0.9098	1.0707

Table 4.2: Comparison of Pressure Peak Position and Free Boundary Values

penalty method to handle the free boundary. In Figure 4.10, the initial guess for pressure is depicted on the left, for which there are 40 elements ($p = 8$ everywhere, $Tol_1 = 0.0001$ and $Tol_2 = 0.000001$). The resulting converged pressure profile is shown on the right in Figure 4.10. There are 21 elements, which are appropriately spaced according to the pressure distribution. The pressure profile obtained using the penalty method and automatic h-adaptivity is very similar to the one obtained using the moving-grid method (which is shown in Figure 4.9). However, since the cavitation position is captured weakly (see equation (4.49)), a very small difference can be observed around the cavitation boundary between the moving-grid solution and the penalty solution. An initial comparison of the pressure profile around the cavitation boundary obtained using the moving-grid method and the penalty method is shown Figure 4.11 (a), from which no difference can be observed. Further comparison in a much smaller region around the cavitation position is demonstrated in Figure 4.11 (b), where a slight difference can be observed since the penalty method captures the cavitation boundary in a weak form (see 4.49) instead of giving the exact cavitation position. This slight difference around the cavitation position can lead to slight differences in the pressure profile elsewhere. Table 4.3 shows a comparison of the peak pressures and peak positions for the grid-moving method and the penalty method.

The above numerical results indicate that the penalty method may not be sufficient when the position of the free boundary is required to very high accuracy if the mesh size of the element, e_{cavi}, which includes the cavitation position is relatively large. Hence, further h-refinement around the cavitation position is needed to improve the accuracy of the cavitation boundary. This further h-refinement is performed until all the pressures on the quadrature points in the element containing the cavitation point are less than a given tolerance (0.00001 say). Figure 4.12 shows a comparison of the pressure profiles around the cavitation position obtained using the moving-grid method and the refined

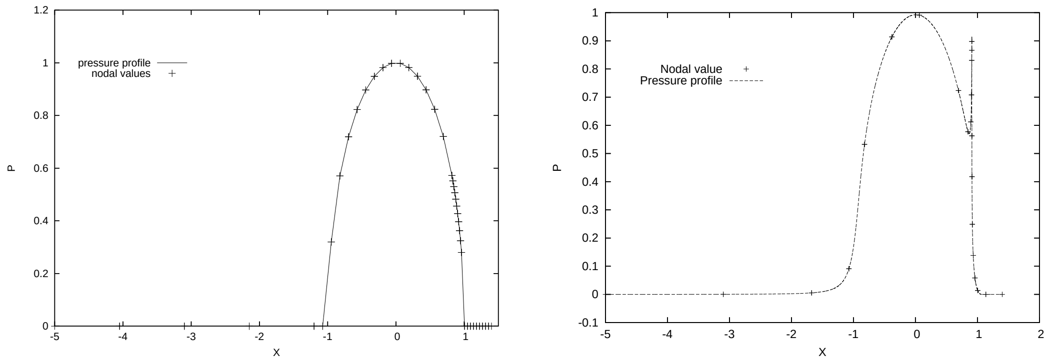

Figure 4.10: Initial guess for pressure, left, and the resulting pressure profile, right

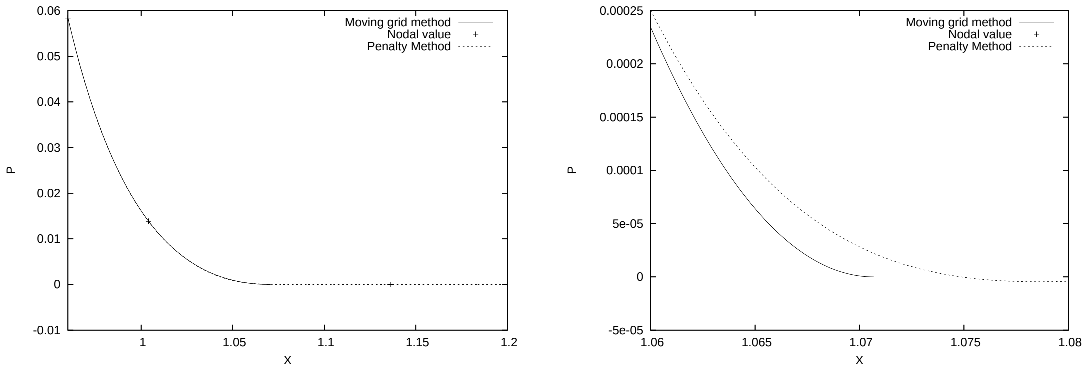

(a) (b)

Figure 4.11: Comparison of the cavitation boundaries obtained using the moving-grid method and the penalty method

penalty method. From Figure 4.12 (a), we can see that the mesh size around the cavitation boundary is much smaller than the size of e_{cavi} in Figure 4.11 (a). Now, no significant difference in the pressures can be observed even in the close-up, Figure 4.12 (b), which indicates that the cavitation boundary is resolved more accurately. The peak value and the peak position are displayed in Table 4.3, showing that the difference between the results is not significant.

In order to demonstrate the robustness of this h-adaptivity method and the flexibility of the high order DG method, another loaded case ($U = 2.0 \times 10^{-11}$, $W = 4.0 \times 10^{-5}$ and $G = 5000$) is solved using different orders ($p = 6$ and $p = 12$ respectively). Figure 4.13

Method	Unknowns	Central pressure	Peak Pressure	Peak Position
Moving-grid method	168	0.992540	0.91646	0.9098
Penalty method	189	0.992561	0.91734	0.909745
Refined penalty method	252	0.992558	0.91660	0.909757

Table 4.3: Comparison of Pressure Peak Position and Free Boundary Values

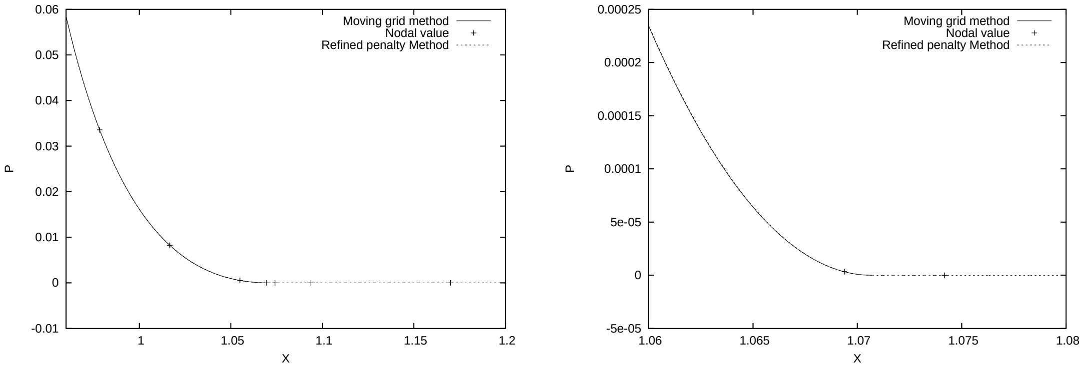

(a) (b)

Figure 4.12: Comparison of the cavitation boundaries obtained using the moving-grid method and the refined penalty method

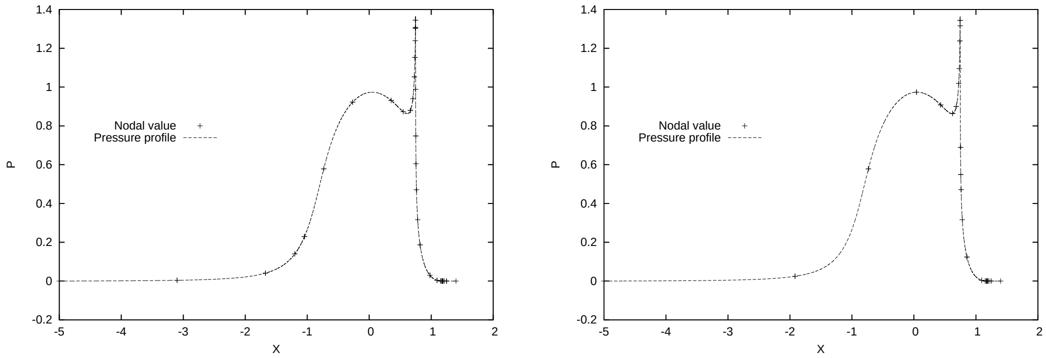

Figure 4.13: Pressure profile when $p = 6$, left, and pressure profile when $p = 12$, right

shows the pressure profiles calculated with $p = 6$ on the left and $p = 12$ on the right. Here $Tol_1 = 0.0001$ and $Tol_2 = 0.000001$ are used in these two cases and the refined penalty method is employed to handle the cavitation boundary. Although different orders are used, the converged pressure profiles match very well. When $p = 6$, 32 elements are used to capture every detail of the solution. When $p = 12$, the converged pressure profile has 25 elements. Table 4.4 displays the pressure peak positions and the peak pressures obtained using different orders. The high quality of the results is the same in both cases.

Figure 4.14 shows some results calculated using the second h-adaptivity method which is based on the high-order components. Here the same initial guess for pressure, as shown

Method	unknowns	Central pressure	Peak Pressure	Peak Position
p = 6	224	0.972538	1.3645	0.74663
p = 12	325	0.972546	1.3644	0.74666

Table 4.4: Comparison of Pressure Peak Position and Peak Pressure when using different orders

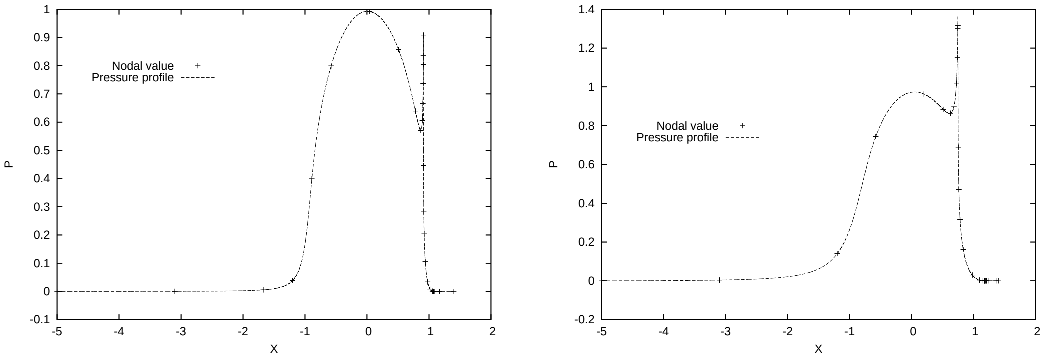

Figure 4.14: Pressure profile when $p = 12$, $U = 1.0 \times 10^{-11}$, $W = 1.0 \times 10^{-4}$ and $G = 5000$, left, and pressure profile when $p = 12$, $U = 2.0 \times 10^{-11}$, $W = 4.0 \times 10^{-5}$ and $G = 5000$, right

Case	Number of elements	Central pressure	Peak Pressure	Peak Position
High load	27	0.992560	0.91658	0.909759
Slight load	26	0.972545	1.36441	0.746668

Table 4.5: Results obtained using the second h-adaptivity method when $p = 12$

in Figure 4.5, is used and $p = 12$. After the solution is fully converged, there are 27 elements over the entire computational domain in the highly loaded case ($U = 1.0 \times 10^{-11}$, $W = 1.0 \times 10^{-4}$ and $G = 5000$) and 26 elements in total in the relatively lightly loaded case ($U = 2.0 \times 10^{-11}$, $W = 4.0 \times 10^{-5}$ and $G = 5000$). From Figure 4.14, 4.13 and 4.10, we can see that the results obtained using different h-adaptivity methods match very well (but see Tables 4.3, 4.4 and 4.5 for the quantitative comparison) and all pressure profiles are sufficiently smooth.

4.7 Conclusion

In this chapter, a new technique, based upon the Discontinuous Galerkin method, is introduced to solve steady-state line contact problems. There are several significant characteristics:

- The accuracy of EHL solutions is very high when using this high order Discontinuous Galerkin method. The upwinding for the convection term is simply implemented, which has been shown to be a significant problem for continuous high order finite element approximations.

- The pressure is expressed in high order form. As a result, the film thickness equation and the force balance equation are also discretized in corresponding high order forms. For the convenience of the computation, two kernels are defined which need to be precomputed numerically.

- The relaxation method introduced is based on the nonlinearity of the resulting discrete system. It is sufficiently robust that we do not need multigrid in order to accelerate convergence. Since we have to solve a linear system at each sweep, it is more expensive than Gauss-Seidel like methods, however the expense is acceptable because the linear system is banded and is not large since there are only a relatively small number of unknowns when using this high order scheme.
- The implementation of the two h-adaptivity methods is simple and natural for high order DG. The application of the h-adaptivity allows every detail of the solution to be captured accurately and at low expense. Furthermore, numerical examples show that h-p-adaptivity is also feasible, although it has not been implemented here.
- The penalty method can be easily implemented to handle the free boundary condition when using high order DG. However, the pressure profile around the cavitation position might not be sufficiently accurate if the element which covers the cavitation position is too large, although the global solution is not significantly affected. Further h-refinement can be used around the cavitation boundary to obtain a more accurate solution in this region if needed.

In the next chapter, the approach is extended to the solution of time-dependent EHL problems.

Chapter 5

High Order DG Solution of Transient Line Contact Problems

5.1 Introduction

In the last chapter, some typical steady-state line contact EHL problems are solved using a high-order DG method. Typical EHL features, such as the cavitation boundary and “the Petrusevich spike” can be precisely captured with far fewer degrees of freedom than are used by standard low-order finite difference methods. However, we should note that each of the cases considered features smooth contacts. That is, the contacting surfaces are smooth. In practice however, the contacting surfaces will not always be smooth. In many situations, the roughness on the surfaces is an important factor and should be taken into account. Furthermore, a transient analysis is required in such situations since the roughness in the contact will vary due to the moving surfaces. This is generally referred to as a micro-EHL contact problem [18, 62]. For theoretical analysis, artificial roughness models (such as indentation or waviness) [62] are usually adopted. In some situations, real roughness can also be handled using numerical methods [18]. Numerical results show that the roughness can strongly affect the pressure distribution and the film thickness profile and that the transient solutions might therefore be significantly different from their steady state counterparts. It follows that transient analysis is of great importance if we are to be able to approach reliable numerical predictions of the real behaviour of lubricants.

In [18], Evans demonstrated the numerical simulation of real roughness, for which complicated non-smoothness is distributed across the entire contact. For such cases, low order schemes are still applicable and can give converged solutions. However it is hard to estimate the accuracy. It is likely that it is impossible to provide highly accurate solutions using the high-order DG scheme since it is not possible to precisely describe the features of such roughness numerically. When the roughness is describable however, such as the roughness models given in [62], the high-order DG can be expected to produce highly accurate solutions. For this reason, the latter case is the focus of this chapter.

In this chapter, the high order DG method is extended to the solution of transient line contact problems. The high-order Discontinuous Galerkin finite element method is used for the spatial discretization and the standard fully implicit Crank-Nicolson method is employed to approximate the time derivative. The second h-adaptivity method developed in Chapter 4 is used for grid adaptation with the time-stepping, and the penalty method is employed to handle the cavitation condition. The roughness model employed here is a simple indentation which is located on the upper surface as studied by [62]. Numerical results are presented comparing the Discontinuous Galerkin method to standard finite difference techniques kindly provided by Dr M. Walkley. It is shown that very detailed micro-EHL features are captured with fewer degrees of freedom compared to the finite difference method.

5.2 Governing Equations

As presented in Chapter 1, The line contact EHL problem consists of three equations: the Reynolds equation, the film thickness equation and the force balance equation. The non-dimensional transient Reynolds equation reads:

$$\frac{\partial}{\partial X}\left(\varepsilon\frac{\partial P}{\partial X}\right)-\frac{\partial(\bar{\rho}H)}{\partial X}-\frac{\partial(\bar{\rho}H)}{\partial T}=0, \tag{5.1}$$

where

$\varepsilon=\frac{\bar{\rho}H^3}{\eta\lambda}$,

P is the unknown pressure,

H is the unknown film thickness,

$\bar{\rho}$ is the density of the lubricant (dependent upon pressure),

$\bar{\eta}$ is the viscosity of the lubricant (dependent upon pressure),

λ is a dimensionless speed parameter,

T is the dimensionless time.

Note that the only difference between the steady-state Reynolds equation and the transient Reynolds equation is that there is a time-dependent term in the transient Reynolds equation, known as the “squeeze” term.

The elasticity and the contact roughness are included through the film thickness equation which, as before, defines the contact geometry for a given pressure solution:

$$H(X,T) = H_{00}(T) + \frac{X^2}{2} - \mathscr{R}(X,T) - \frac{1}{\pi}\int_{-\infty}^{\infty} \ln|X - X^{'}|P(X^{'},T)\,\mathrm{d}X^{'}, \tag{5.2}$$

where

$H_{00}(T)$ is the central offset film thickness,

$\mathscr{R}(X,T)$ describes the surface roughness.

Note that this equation is identical to that used in the previous chapters except for the roughness term $\mathscr{R}(X,T)$. In this thesis we adopt the same dimensionless model of the roughness used by Venner in [62]:

$$\mathscr{R}(X,T) = \alpha 10^{-10((X-X_d))^2}\cos\left(2\pi(X - X_d)\right), \tag{5.3}$$

where

$\alpha = -0.11$ is the amplitude of a smooth dent in the parabolic surface,

X_d is the position of the centre of the dent at time T.

Here, X_d is given by:

$$X_d = X_s + 2\frac{u_2}{u_s}T, \tag{5.4}$$

where

X_s denotes the position of the dent at $T = 0$

u_2 is the velocity of the indented upper surface

u_s is the sum velocity of the indented upper surface and the flat lower surface.

In this example we set $\frac{u_2}{u_s} = 0.25$, hence some sliding behaviour is implied.

The force balance equation remains the same as in the steady-state case, given by:

$$\int_{-\infty}^{\infty} P(X)\,\mathrm{d}X - \frac{\pi}{2} = 0. \tag{5.5}$$

5.3 Discretization

The discretization of the transient EHL problem consists of two components: spatial discretization and temporal discretization. In order to resolve highly accurate solutions, the high order DG scheme is employed for the spatial discretization. The Crank-Nicolson method [18] is used to undertake time-stepping.

5.3.1 Spatial Discretization

Recall from the previous chapter that for the steady-state problem, using the DG scheme and the penalty method, the Reynolds equation can be discretized into the following nonlinear system:

$$L(P,v) = a(P,v) + \frac{1}{\delta}\sum_{e\in\Omega_h}\int_e P_- v \,\mathrm{d}X - l(P,v) = 0, \tag{5.6}$$

where δ is an arbitrary positive number and

$$P_- = min(P,0). \tag{5.7}$$

Substituting equation (4.3) into (5.6), the steady-state equation (4.49) can therefore be written in the general nonlinear form:

$$L(U) = A(U)U - b(U) = 0, \tag{5.8}$$

where

$$U = \left(u_1^1,\dots,u_{p^1+1}^1;\dots;u_1^N,\dots,u_{p^N+1}^N\right)^T. \tag{5.9}$$

With this spatial discretization of the steady-state problem in hand, it is convenient for us use the same notation to describe the Crank-Nicolson discretization of the time-dependent problem.

5.3.2 Temporal Discretization

Note that the transient form of the Reynolds equation contains the single time-dependent term, $\frac{\partial}{\partial T}(\bar{\rho}H)$. Consequently, using the Crank-Nicolson method [18] and the DG spatial discretization (5.6), the 1D transient Reynolds equation is discretized to be:

$$-\sum_{e\in\Omega_h}\left(\int_e \bar{\rho}Hv\,\mathrm{d}x\right)^T+\sum_{e\in\Omega_h}\left(\int_e \bar{\rho}Hv\,\mathrm{d}x\right)^{T+\triangle T}$$
$$+\theta\triangle TL(P,v)^T+(1-\theta)\triangle TL(P,v)^{T+\triangle T}=0,\ \forall v\in V,\quad (5.10)$$

where $\theta=0.5$ gives the Crank-Nicolson discretization and $\theta=0$ implies the implicit Euler scheme. The above equation allows for a single time step to be taken from T to $T+\triangle T$ and the superscripts are used to denote the time level at which the different terms are to be evaluated. Reorganizing this equation, so that all of the unknown terms at time $T+\triangle T$ are grouped together, yields the following discrete form:

$$\sum_{e\in\Omega_h}\left(\int_e \bar{\rho}Hv\,\mathrm{d}x\right)^{T+\triangle T}+(1-\theta)\triangle TL(P,v)^{T+\triangle T}=$$
$$\sum_{e\in\Omega_h}\left(\int_e \bar{\rho}Hv\,\mathrm{d}x\right)^{T}-\theta\triangle TL(P,v)^T.\quad (5.11)$$

To simplify the notation further, using (4.3), we rewrite the above system to be:

$$R(U^{T+\triangle T})=C(U^{T+\triangle T})+(1-\theta)\triangle TL(U^{T+\triangle T})-C(U^T)+\theta\triangle TL(P,v)^T=0,\quad (5.12)$$

where L is given by (5.8), $C(U^{T+\triangle T})$ has components $(\int_e \bar{\rho}HN_i^e\,\mathrm{d}x)^{T+\triangle T}$, $C(U^T)$ has components $(\int_e \bar{\rho}HN_i^e\,\mathrm{d}x)^T$ and

$$U^{T+\triangle T}=\left((u_1^1)^{T+\triangle T},\dots,(u_{p^1+1}^1)^{T+\triangle T};\dots;(u_1^N)^{T+\triangle T},\dots,(u_{p^N+1}^N)^{T+\triangle T}\right)^T\quad (5.13)$$

are the unknown pressure coefficients. At each time step, $U^{T+\triangle T}$ is required to be solved from (5.12) based on the obtained U^T at the previous time step. It is assumed that the initial pressure profile (and therefore the value of U^T when $T=0$) is known.

5.4 Relaxation

Similar to the nonlinear smoother introduced for the steady-state problems, the following relaxation method is used to define an iterative solver for (5.12) at each time step:

$$\begin{aligned} U^{T+\triangle T} &\leftarrow U^{T+\triangle T} \\ &+ C_1\left(\frac{\partial}{\partial U^{T+\triangle T}}\left(C(U^{T+\triangle T})+(1-\theta)\triangle T L(U^{T+\triangle T})\right)\right)^{-1} \\ &\quad R(U^{T+\triangle T}), \end{aligned} \tag{5.14}$$

where $R(U^{T+\triangle T})$ is the current numerical residual, $U^{T+\triangle T}$ is initialized to be equal to U^T and C_1 is the under-relaxation factor for pressure. According to equation (4.37), the Jacobian, $\frac{\partial L(U^{T+\triangle T})}{\partial U^{T+\triangle T}}$, may be approximated by:

$$\frac{\partial L(U^{T+\triangle T})}{\partial U^{T+\triangle T}} \approx A(U^{T+\triangle T}) - \frac{\partial b(U^{T+\triangle T})}{\partial U^{T+\triangle T}}. \tag{5.15}$$

Furthermore $\partial b(U^{T+\triangle T})/\partial U^{T+\triangle T}$ is a full matrix:

$$\begin{aligned} \frac{\partial b(U^{T+\triangle T})}{\partial U^{T+\triangle T}}_{I,J} &= \left[\frac{\partial b(U)_i^e}{\partial U_j^f}\right]^{T+\triangle T} \\ &= \left[\int_e \bar{\rho}\frac{\partial H^e(X)}{\partial U_j^f}\frac{\partial v}{\partial X}\,\mathrm{d}X\right]^{T+\triangle T} \\ &+ \left[\sum_{\Gamma_{int}}[v]\left\langle \bar{\rho}(P^-)\frac{\partial H}{\partial U_j^f} + \frac{\partial \bar{\rho}(P^-)}{\partial U_j^f}H\right\rangle\right]^{T+\triangle T} \\ &+ \left[\left(\bar{\rho}\frac{\partial H}{\partial U_j^f}v\right)|_{X_{inlet}}\right]^{T+\triangle T} - \left[\left(\bar{\rho}\frac{\partial H}{\partial U_j^f}v\right)|_{X_{outlet}}\right]^{T+\triangle T}, \end{aligned} \tag{5.16}$$

where the Ith row corresponds to the row generated with the test function $v = N_i^e(X)$ and the Jth column corresponds to the unknown U_j^f. Since $C(U^{T+\triangle T})$ has components $(\int_e \bar{\rho} H N_i^e \mathrm{d}x)^{T+\triangle T}$, which involve the film thickness H, $\partial C(U^{T+\triangle T})/\partial U^{T+\triangle T}$ is also a full matrix:

$$\begin{aligned}\frac{\partial C(U^{T+\triangle T})}{\partial U^{T+\triangle T}}_{I,J} &= \left[\frac{\partial C(U)_i^e}{\partial U_j^f}\right]^{T+\triangle T} \\ &= \left[\int_e \left(\bar{\rho}\frac{\partial H^e(X)}{\partial U_j^f}v + \frac{\partial \bar{\rho}}{\partial U_j^f}Hv\right)\,\mathrm{d}X\right]^{T+\triangle T}. \end{aligned} \tag{5.17}$$

5.5 Adaptivity

For steady-state line contact problems, in Chapter 4, a simple h-adaptivity method was developed. This triggered local refinement based on the magnitude of the discontinuities in pressure over element interfaces (since the target was to obtain a sufficiently smooth pressure profile). However, following some preliminary numerical experiments, this method is found to be insufficiently robust for transient line contact problems. This is because the magnitude of the discontinuities between neighbouring elements does not fully represent the degree of the accuracy of the numerical solution. Furthermore, for time-dependent problems, it is always a challenge to control the global error since a sequence of solutions are required and the errors generated at the previous time steps will of course affect the quality of the later numerical solutions.

In this chapter therefore, the h-adaptivity method, based on the high-order components, is employed for transient EHL problems. The basic principle behind the adaptivity is summarized as follows:

1. Refine any element on which the solution has too large a contribution from the highest order basis functions. Here we give a small tolerance $Tol_{refine} = 0.0001$. If either of the last two high order coefficients ($(u^e_{p^e})^{T+\triangle T}$ and $(u^e_{p^e+1})^{T+\triangle T}$) is greater than Tol_{refine}, divide the element e to be two equally spaced smaller elements.

2. Agglomerate two neighbouring elements to be a larger one if the local solution is sufficiently smooth. Here, for every pair of neighbouring elements (for example e and $e+1$), we agglomerate them to be a larger trial element E and interpolate the local solution (both $U^{T+\triangle T}$ and U^T) onto the trial element. If the coefficients $(u^E_{p^E})^{T+\triangle T}$, $(u^E_{p^E+1})^{T+\triangle T}$, $(u^E_{p^E})^T$ and $(u^E_{p^E+1})^T$ are all less than another tolerance $Tol_{coarsen} = 0.00005 < Tol_{refine}$, take E as the new local mesh element to replace e and $e+1$.

Figure 5.1 shows the schematic refinement and coarsening operations.

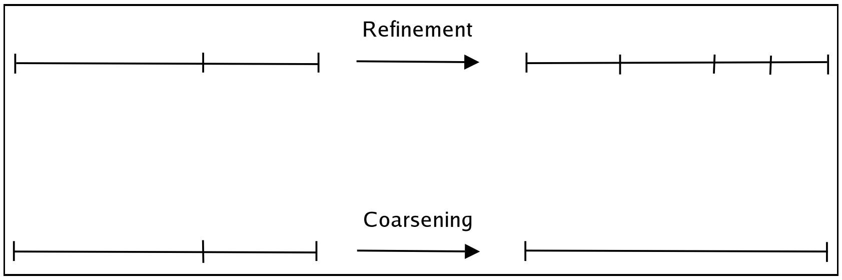

Figure 5.1: H-adaptivity

Once the grid is changed, $U^{T+\triangle T}$ and U^{T} need to be transferred from the original grid onto the new grid using the two transfer operators: I_f^c and I_c^f, defined in Section 4.5.3, to transfer data from finer mesh to coarser mesh and from coarser mesh to finer mesh respectively.

5.5.1 Overall Solution Procedure

A sequence of numerical solutions at different time steps are calculated as follows.

1. At the start, the roughness is located far from the contact region. The steady state solution at $T = 0$ is calculated. Then for each time step, repeat 2-5 below.
2. Choose $u^{T+\triangle T} = u^{T}$ as initial guess.
3. Update $u^{T+\triangle T}$ based on u^{T} using (5.14) until $R^{T+\triangle T}$ is small (smaller than $\mathscr{O}(10^{-7})$ for example).
4. Check if the grid needs to be adjusted. If yes, go to step 2 after generating the new grid according to the h-adaptivity method discussed above and transferring both $u^{T+\triangle T}$ and u^{T} onto the new grid.
5. Update $u^{T+\triangle T}$ until $R^{T+\triangle T}$ in (5.12) is smaller than a final convergence tolerance ($\mathscr{O}(10^{-11})$ say).

Note that we need to check the degree of smoothness for both $u^{T+\triangle T}$ and u^{T} on the local trial element when determining whether to coarsen the local mesh. The local mesh is coarsened only if both of the local solutions at T and $T+\triangle T$ are sufficiently smooth. The resulting grid at each time step must be good enough for both $u^{T+\triangle T}$ and u^{T}.

5.6 Numerical Results

In this section, we focus on the solution of our transient model problem using the DG scheme and demonstrate that it is capable of resolving details of the solution that are not so easily captured by a more traditional finite difference scheme with a similar number of degrees of freedom (or even with substantially more).

In particular, our proposed numerical scheme for compressible transient EHL is used to investigate the influence of a dent on the upper surface on the pressure and the film thickness under prescribed conditions. In standard Dowson and Higginson notation the case solved here is specified by the non-dimensional quantities, $U = 0.15 \times 10^{-11}$, $W = 0.4 \times 10^{-4}$, $G = 4942$ (see [60]). The computational domain is $[-5.0, 1.5]$. The roughness model used is given by (5.3).

When $T = 0$, where $X_d = -2.0$ (relatively far from the contact centre), the pressure and film thickness, depicted on the left in Figure 5.2, are quite similar to the steady-state solution for the smooth contact. A detailed view of the pressure spike (at $T = 0$) captured by DG and FD schemes is shown on the right in Figure 5.2. Note that the FD solutions for which the grid points are equally spaced converge toward the DG solution ($p^e = 8$ everywhere, 32 elements and 288 unknowns in total) with increasing number of grid points. Further, it is seen that the DG method resolves the pressure spike more accurately than FD, as in [40].

Figure 5.3 shows a sequence of solutions (pressure and film thickness) with the dent moving. Note that in Figure 5.3(c) a new pressure spike is captured (at approximately $X = -0.8$), which is caused by the roughness. This becomes sharper in Figure 5.3(d) and then begins to disappear in Figure 5.3(e). After the dent passes the contact centre, this spike grows up again (see Figure 5.3(j) and 5.3(k)). When the dent centre arrives at the “Petrusevich Spike” region, the combination of the roughness and the film thickness dip produces a much sharper pressure spike than would otherwise be present (see Figure 5.3(l)).

At each time step, the total number of elements present remains no more than 60 since h-adaptivity is employed. Since $p = 8$ everywhere the total number of degrees of freedom never exceeds 540. It should be noted however that the time step has to be quite small in order to ensure convergence ($\triangle T = 0.001$ when the pressure profile is relatively smooth and $\triangle T = 0.0001$ when the sharp spike shown in Figure 5.3 (l) appears and small elements are required to resolve it).

In order to further illustrate the potential of this method, we have also included results computed using the standard multilevel finite difference scheme [25, 60] on a moderately

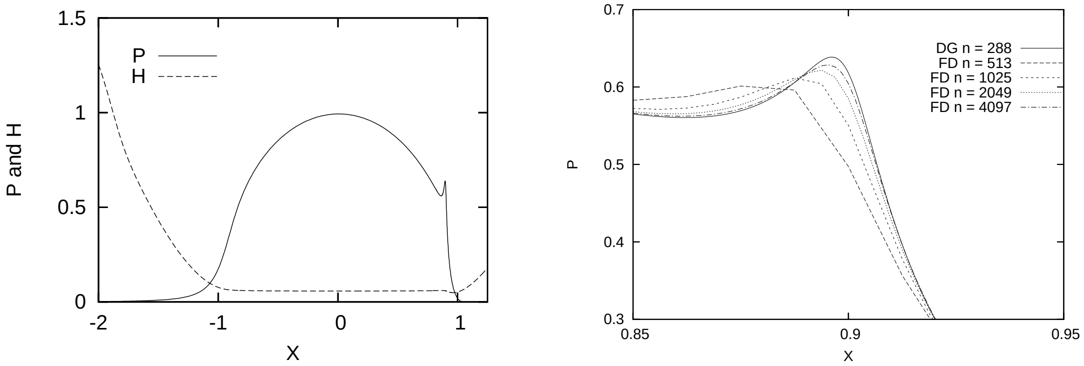

(a) DG solution calculated at $T = 0$ (b) Resolution of the initial pressure spike compared to the standard FDM

Figure 5.2: Non-dimensional pressure and film thickness when X_d = -2.0

sized grid of 1025 points (provided by Dr M. Walkley). Figure 5.4 shows a series of close-ups of the pressure spike that is caused by the roughness, which has not been captured by the multilevel FD method. Note that there is no spike in Figure 5.4 (a) when $X_d = -0.9$, but the roughness has significantly affected the pressure profile (in the region [-1.5,-0.5]). From Figure 5.4(b) to (f), the spike has been clearly captured by the DG method and completely missed by the FD method. It should be noted that elsewhere in the domain there is good agreement between the two solutions.

It is important to note that the implications of this additional accuracy in the DG scheme are that useful quantities, such as friction [27], can be computed with greater accuracy at relatively low resolution. As described in [27] a non-dimensional model for the friction is given by:

$$F = \int_{X_{inlet}}^{X_{outlet}} -m_1 \frac{\mathrm{d}P}{\mathrm{d}X}\frac{H}{2} + m_2 \frac{\eta}{H}(U_2 - U_1)\,\mathrm{d}X, \qquad (5.18)$$

where $m_1 = \frac{p_h b^2}{R}$ and $m_2 = \frac{\eta_0 R}{b}$ (see more details about these parameters in Chapter 1). Table 5.1 shows a comparison of this non-dimensional friction calculated from the DG solution and the FD solution with 1025 grid points, at a range of times. At times in the simulation where the micro-EHL spike is apparent, the solution computed by the FD scheme, which misses the spike, is up to 20% different from the DG solution. This is due to both the significant discrepancy in $\frac{\mathrm{d}P}{\mathrm{d}X}$ in the rolling term (the first term in the integrand in (5.18)) and the large difference in η (which depends exponentially on P, see Equation (1.6)) in the sliding term (the second term in the integrand) of the friction equation (5.18).

In the above results, some interesting micro-EHL features (for example, the extra pressure spike) are observed. In order to confirm this physical phenomenon, another

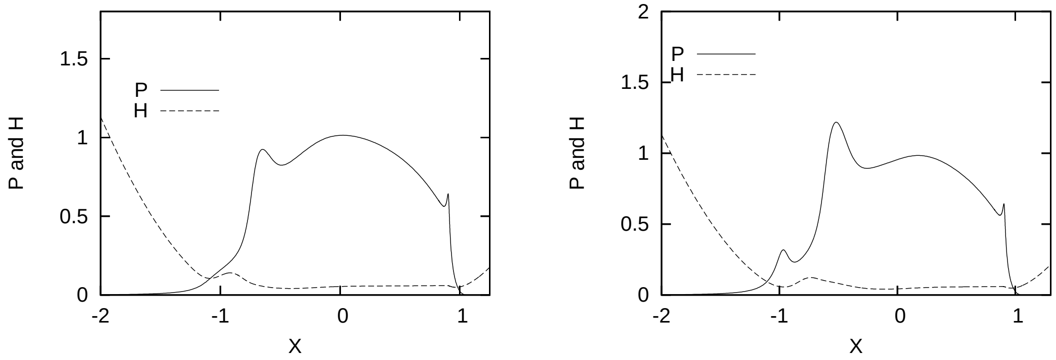

(a) $X_d = -0.9$ (b) $X_d = -0.75$

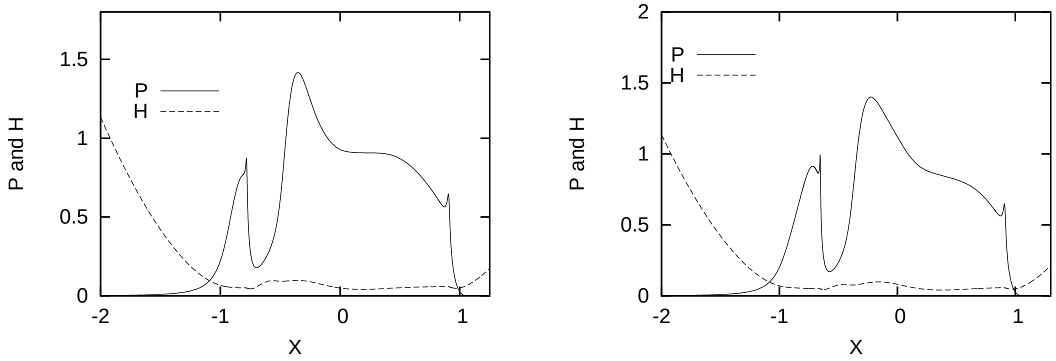

(c) $X_d = -0.6$ (d) $X_d = -0.5$

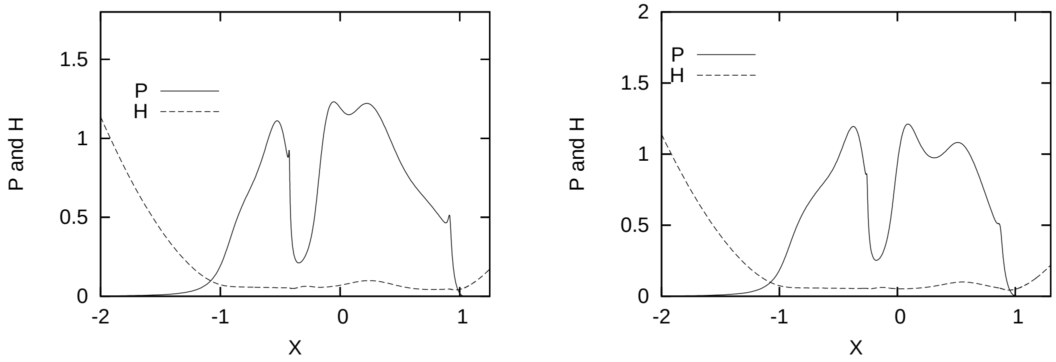

(e) $X_d = -0.3$ (f) $X_d = -0.145$

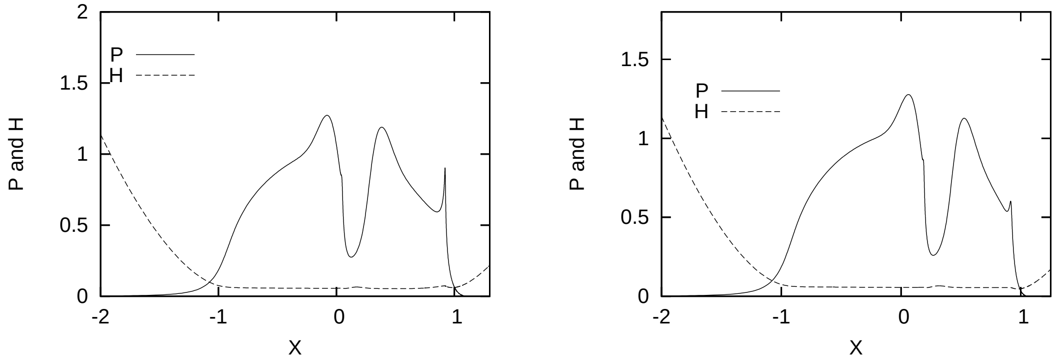

(g) $X_d = 0.155$ (h) $X_d = 0.3$

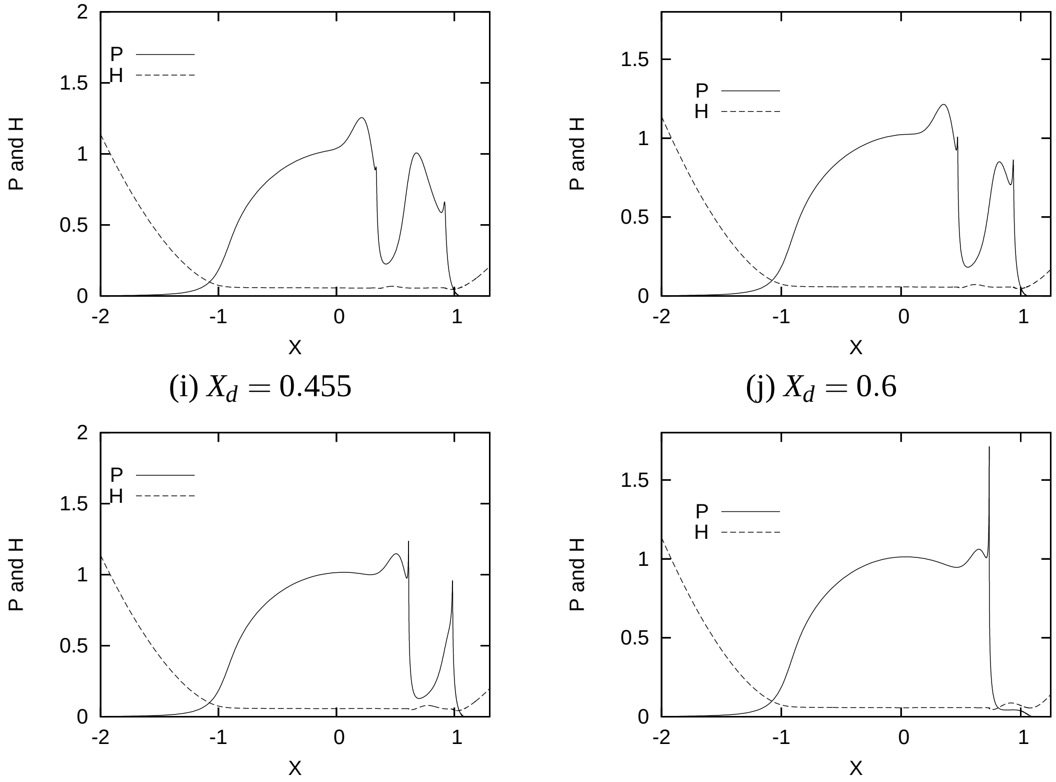

(i) $X_d = 0.455$ (j) $X_d = 0.6$

(k) $X_d = 0.755$ (l) $X_d = 0.9$

Figure 5.3: Non-dimensional P and H obtained using the DG simulation for the first transient problem

X_d	-2.0	-0.9	-0.6	-0.3	0.3	0.6	0.9
DG	-97.96	-166.3	-219.7	-126.7	-135.1	-136.6	-127.2
FD	-92.07	-161.5	-206.6	-108.0	-106.9	-118.1	-109.7

Table 5.1: Comparison of friction at particular times

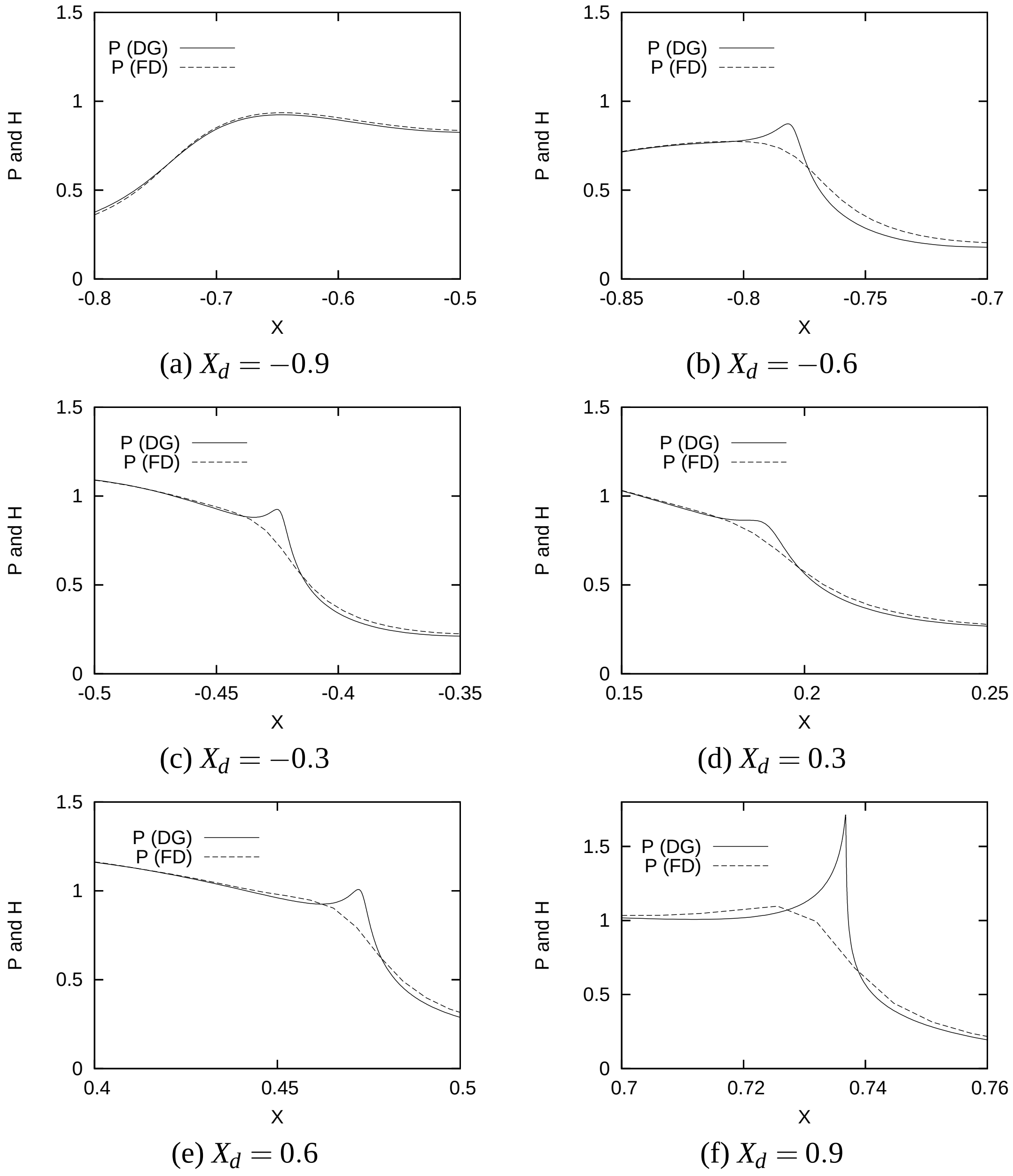

(a) $X_d = -0.9$ (b) $X_d = -0.6$

(c) $X_d = -0.3$ (d) $X_d = 0.3$

(e) $X_d = 0.6$ (f) $X_d = 0.9$

Figure 5.4: Comparison of the fine details of the pressure computed via the new Discontinuous Galerkin (DG) method and using the standard multilevel Finite Difference (FD) solver on a mesh of 1025 points

numerical test is performed. Here a slightly different roughness model, which is referred to as “Roughness 2” here compared to “Roughness 1” in equation (5.3), is used for the same loaded case:

$$\mathscr{R}(X,T) = \alpha 10^{-40((X-X_d))^2}\cos(4\pi(X-X_d)), \tag{5.19}$$

where

$\alpha = -0.04$ (rather than -0.11 in equation (5.3)) is the amplitude of a smooth dent in the parabolic surface,

X_d is the position of the centre of the dent at time T.

Here, X_d is given by:

$$X_d = X_s + 2\frac{u_2}{u_s}T, \tag{5.20}$$

where

X_s denotes the position of the dent at $T = 0$

u_2 is the velocity of the indented upper surface

u_s is the sum velocity of the indented upper surface and the flat lower surface and $\frac{u_2}{u_s} = 0.25$.

The Crank-Nicolson method and the high-order DG ($p = 8$) are employed for temporal discretization and spatial discretization respectively. When the pressure profile is relatively smooth ($X_d < 0.945$), $\triangle T = 0.002$ is used. When $X_d \geq 0.945$ more micro-details appear, therefore, a smaller time step is employed: $\triangle T = 0.00002$. At each time step the number of the elements remains no more than 45. A sequence of results are shown in Figure 5.5 and some interesting details in pressure are demonstrated in Figure 5.6. Here, similar micro-EHL features are captured and the shape of the extra pressure spike is slightly different from the one shown in Figure 5.3 due to the difference between the two roughness models.

In the above results, the Crank-Nicolson method is used for temporal discretization however a much smaller time step has to be used when some micro-features appear (for example (l) in Figure 5.3) to ensure convergence of the nonlinear solver. However, when the time step becomes too small (for example $\triangle T < 0.00001$), it is difficult for the nonlinear smoother (see equation (5.14)) to converge at all. Numerical tests indicate that this smoother is more robust when a smaller value of θ is used for temporal discretization

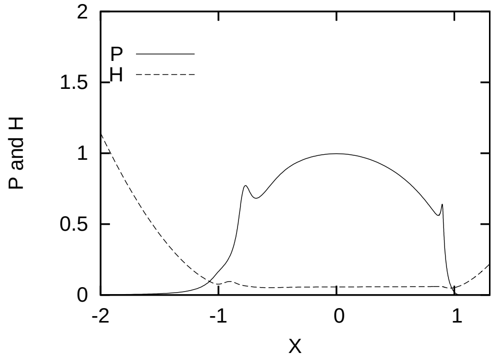

(a) $X_d = -0.9$

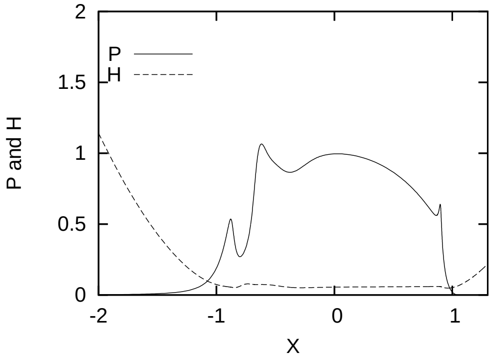

(b) $X_d = -0.75$

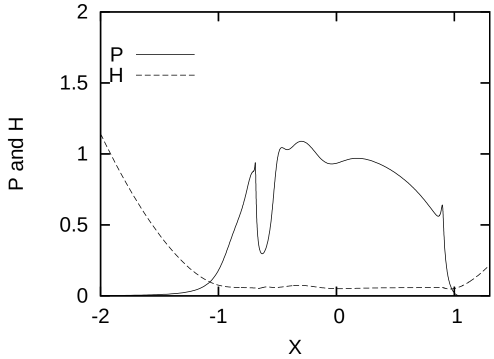

(c) $X_d = -0.6$

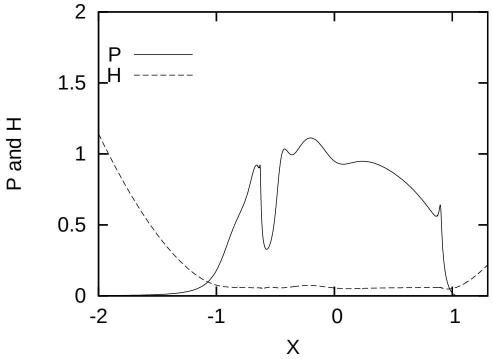

(d) $X_d = -0.55$

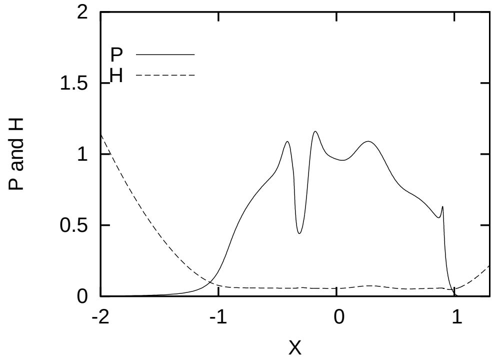

(e) $X_d = -0.3$

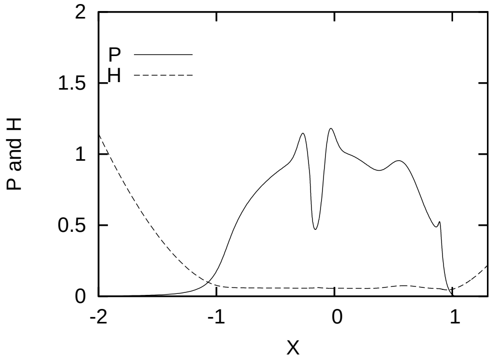

(f) $X_d = -0.15$

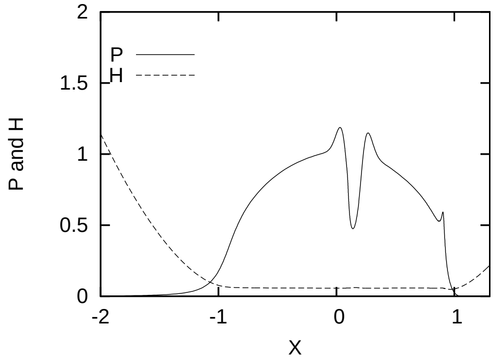

(g) $X_d = 0.15$

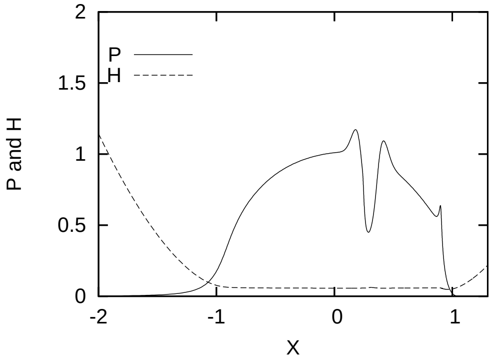

(h) $X_d = 0.3$

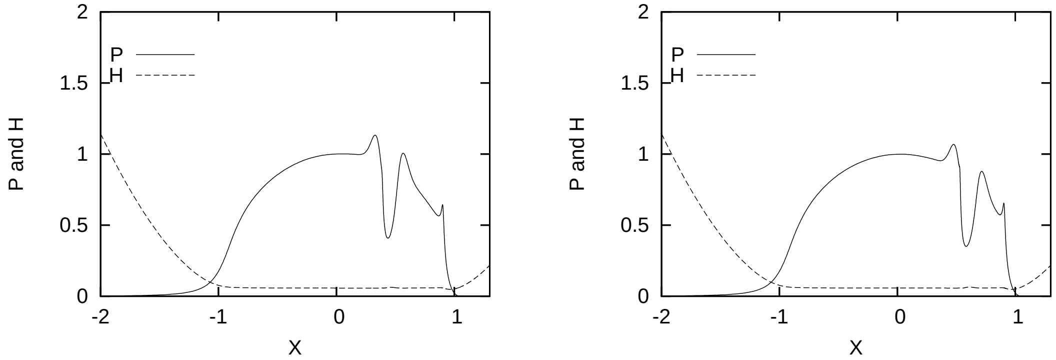

(i) $X_d = 0.45$ (j) $X_d = 0.6$

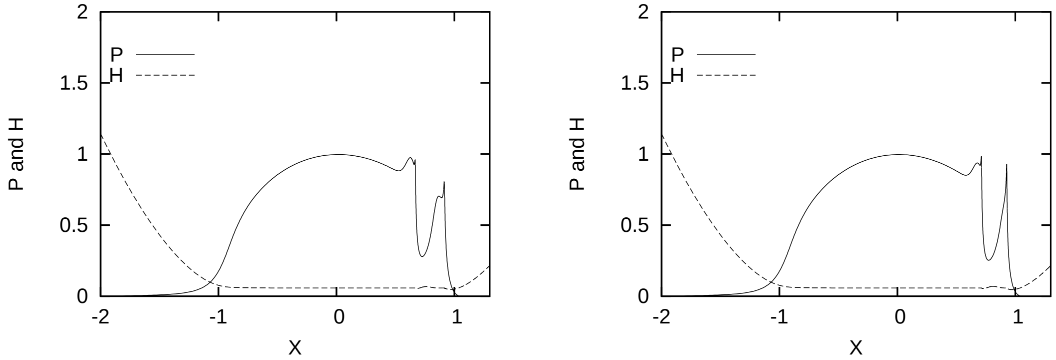

(k) $X_d = 0.75$ (l) $X_d = 0.8$

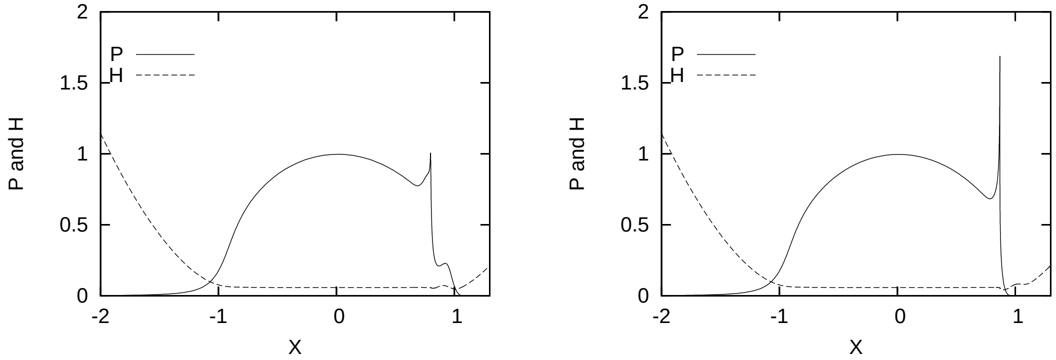

(m) $X_d = 0.9$ (n) $X_d = 1.0$

Figure 5.5: Non-dimensional P and H obtained using the DG simulation for the second transient test problem

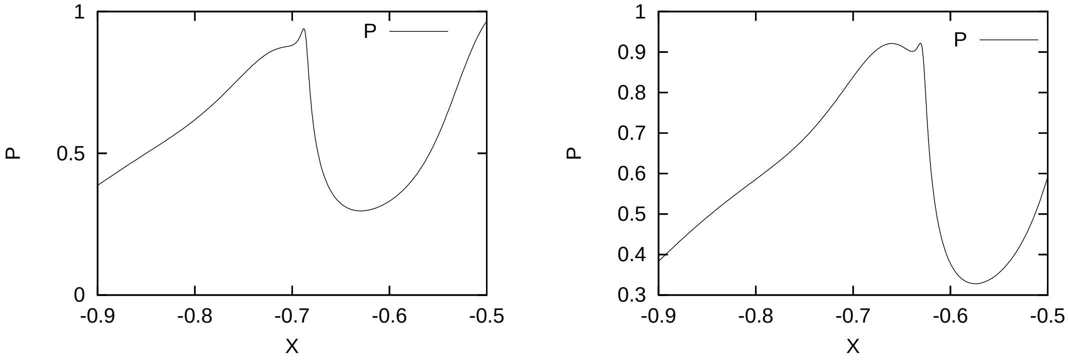

(a) $X_d = -0.6$ (b) $X_d = -0.55$

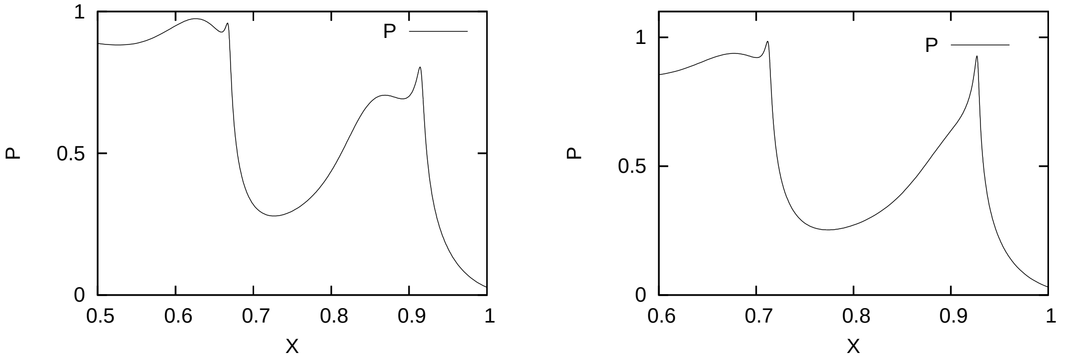

(c) $X_d = 0.75$ (d) $X_d = 0.8$

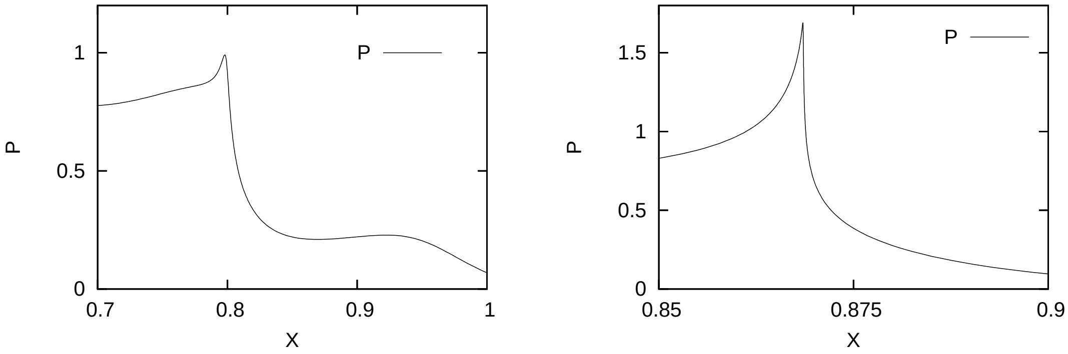

(e) $X_d = 0.9$ (f) $X_d = 1.0$

Figure 5.6: Some fine details of the pressure computed using the new Discontinuous Galerkin (DG) method

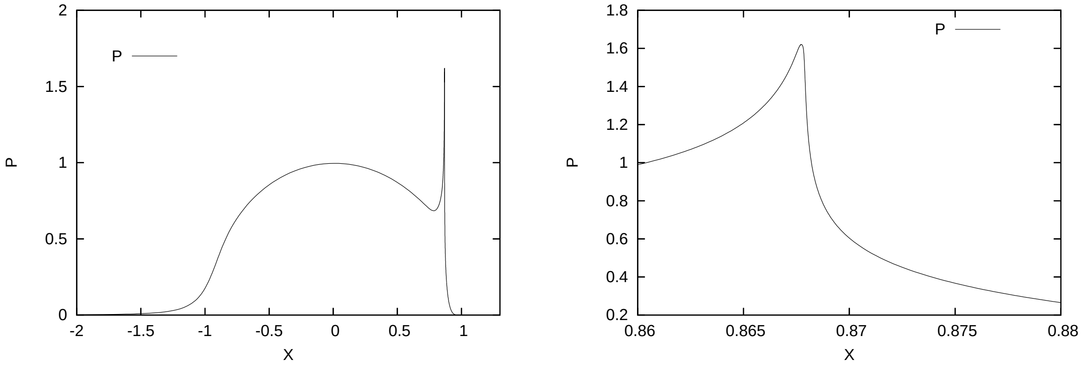

(a) Pressure profile (b) Pressure spike

Figure 5.7: Pressure profile when $X_d = 1.0$ for the second transient test problem

(i.e. the scheme is more implicit). Although in theory the Crank-Nicolson method is more accurate than the more implicit methods, little difference can be observed when a sufficiently small time step is used. To show this, a further numerical test is undertaken. We still use the second roughness model (see equation (5.19)), but we start from the solution when $X_d = 1.0$, where the pressure spike has become very sharp (see Figure 5.7 (a)). Then different time-stepping methods ($\theta = 0.5$, $\theta = 0.45$, $\theta = 0.25$ and $\theta = 0.0$) and different time steps ($\triangle T = 0.001$ and $\triangle T = 0.0001$) are used to advance X_d to 1.01. The resulting pressure profiles are displayed in Figure 5.8. When using Crank-Nicolson method and a relatively large time step ($\theta = 0.5$ and $\triangle T = 0.001$) the resulting pressure spike is not smooth. With decreasing θ, the pressure spike becomes smoother and the position of the pressure spike remains almost the same (around $X = 0.8722$) (see Figure 5.8 (b)). When using smaller time steps ($\triangle T = 0.0001$), no significant difference can be observed between the different time-stepping methods. When fixing θ but different time steps ($\triangle T = 0.001$ and $\triangle T = 0.0001$), the positions of the pressure spikes are significantly different (around $X = 0.8722$ when $\triangle T = 0.001$ and around $X = 0.8727$ when $\triangle T = 0.0001$). This last observation reflects the fact that the choice of the $\triangle T$ is more important for accuracy than the choice of θ.

Figure 5.9 displays the results calculated using implicit time-stepping ($\theta = 0$), where we use the same loaded case and the roughness model as in Figure 5.3. But here we use higher-order DG (p = 12) for the spatial discretization. When $X_d < 0.8$, $\triangle T = 0.001$ and $\triangle T = 0.0001$ when $X_d \geq 0.8$. At each time step, the number of elements remains no more than 50. The results in Figure 5.9 match well with the corresponding results in Figure 5.3 though different time-stepping and different order are used.

The additional pressure spikes captured in the above results (see Figure 5.3, 5.5 and 5.9) are very interesting. However, for other relatively smooth roughness models, this

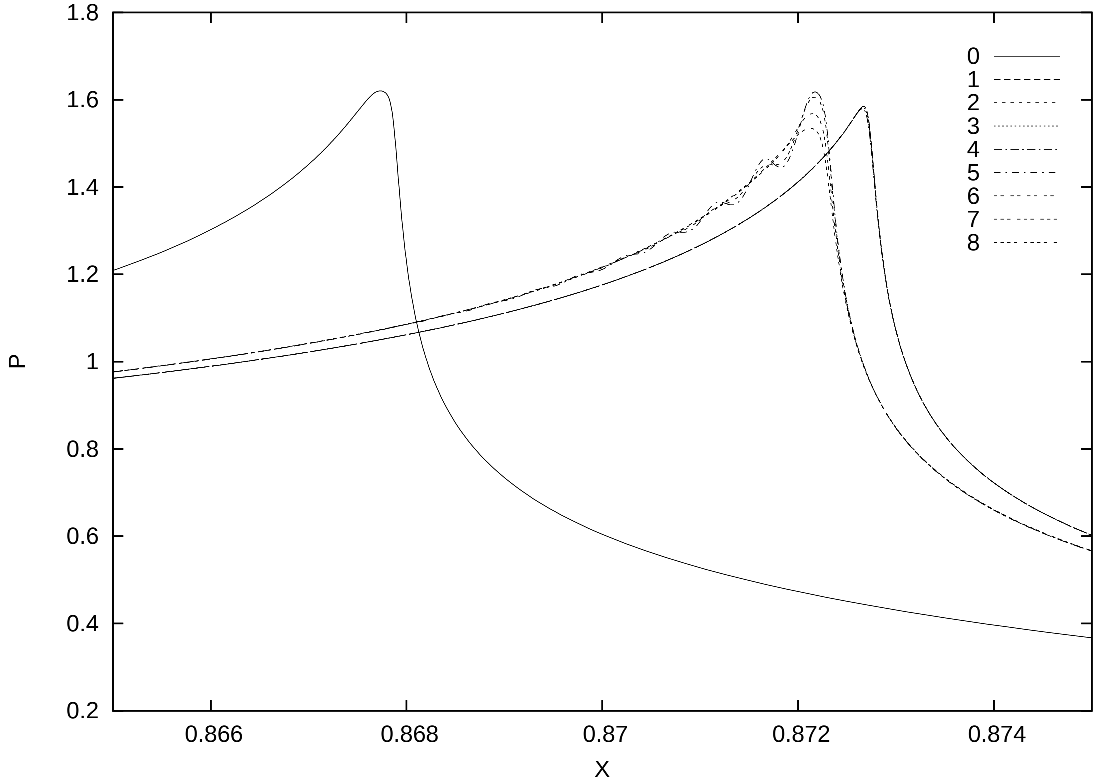

(a) Initial guess (0) and predicted solutions

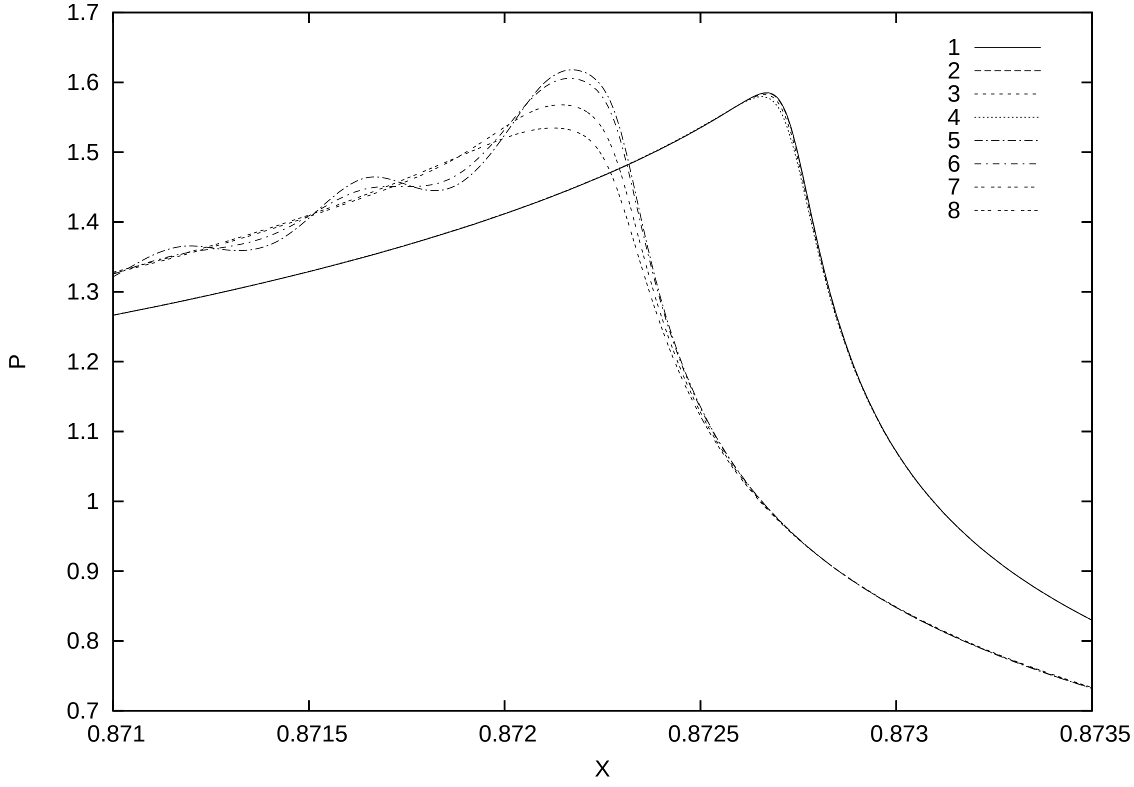

(b) Close-up of the predicted solutions

Figure 5.8: Comparison of the pressure profiles obtained using different θ and $\triangle T$. 0, initial guess. 1, $\theta = 0.5$ and $\triangle T = 0.0001$. 2, $\theta = 0.45$ and $\triangle T = 0.0001$. 3, $\theta = 0.25$ and $\triangle T = 0.0001$. 4, $\theta = 0.0$ and $\triangle T = 0.0001$. 5, $\theta = 0.5$ and $\triangle T = 0.001$. 6, $\theta = 0.45$ and $\triangle T = 0.001$. 7, $\theta = 0.25$ and $\triangle T = 0.001$. 8, $\theta = 0.0$ and $\triangle T = 0.001$.

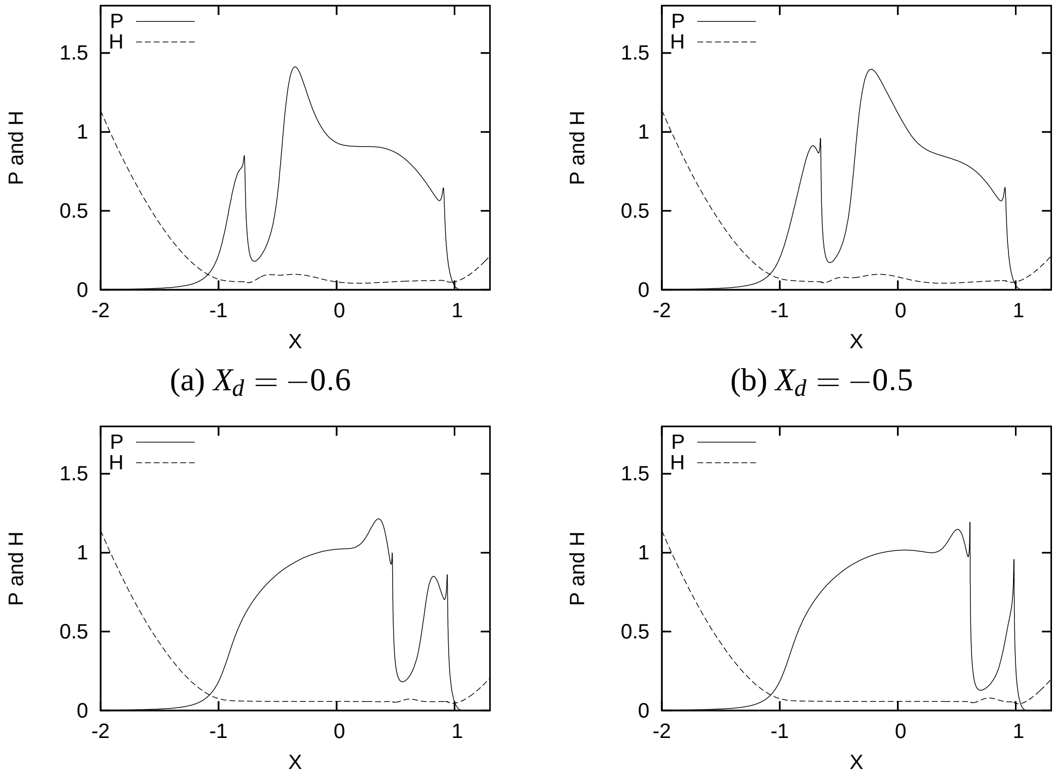

(a) $X_d = -0.6$ (b) $X_d = -0.5$

(c) $X_d = 0.6$ (d) $X_d = 0.755$

Figure 5.9: Non-dimensional P and H obtained for the first roughness model but with different spatial degree and different time-stepping to the results in Figure 5.3

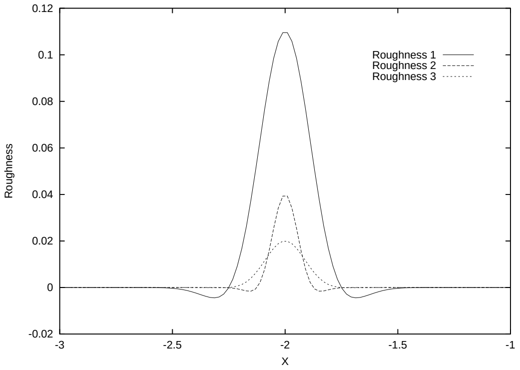

Figure 5.10: Three roughness models

phenomenon might not happen. Here we test another roughness model, “Roughness 3”, which is:

$$\mathscr{R}(X,T) = \alpha 10^{-20((X-X_d))^2}\cos(2\pi(X-X_d)), \tag{5.21}$$

where

$\alpha = -0.02$ (rather than -0.11 in equation (5.3)) is the amplitude of a smooth dent in the parabolic surface,

X_d is the position of the centre of the dent at time T.

Here, X_d is given by:

$$X_d = X_s + 2\frac{u_2}{u_s}T, \tag{5.22}$$

where

X_s denotes the position of the dent at $T = 0$

u_2 is the velocity of the indented upper surface

u_s is the sum velocity of the indented upper surface and the flat lower surface and $\frac{u_2}{u_s} = 0.25$.

The comparison of the three roughness shapes when $T = 0$ is shown in Figure 5.10.

In the calculations undertaken $p = 12$, $\triangle T = 0.001$ when $X_d < 0.8$ and $\triangle T = 0.0001$ when $X_d \geq 0.8$. At each time step, the number of elements remains no more than 30. The resolved pressure profiles are displayed in Figure 5.11. Compared to the results in Figure 5.3 and 5.5, the pressure profiles in Figure 5.11 are much more smooth and no extra pressure spike is observed due to the presence of the dent in this case.

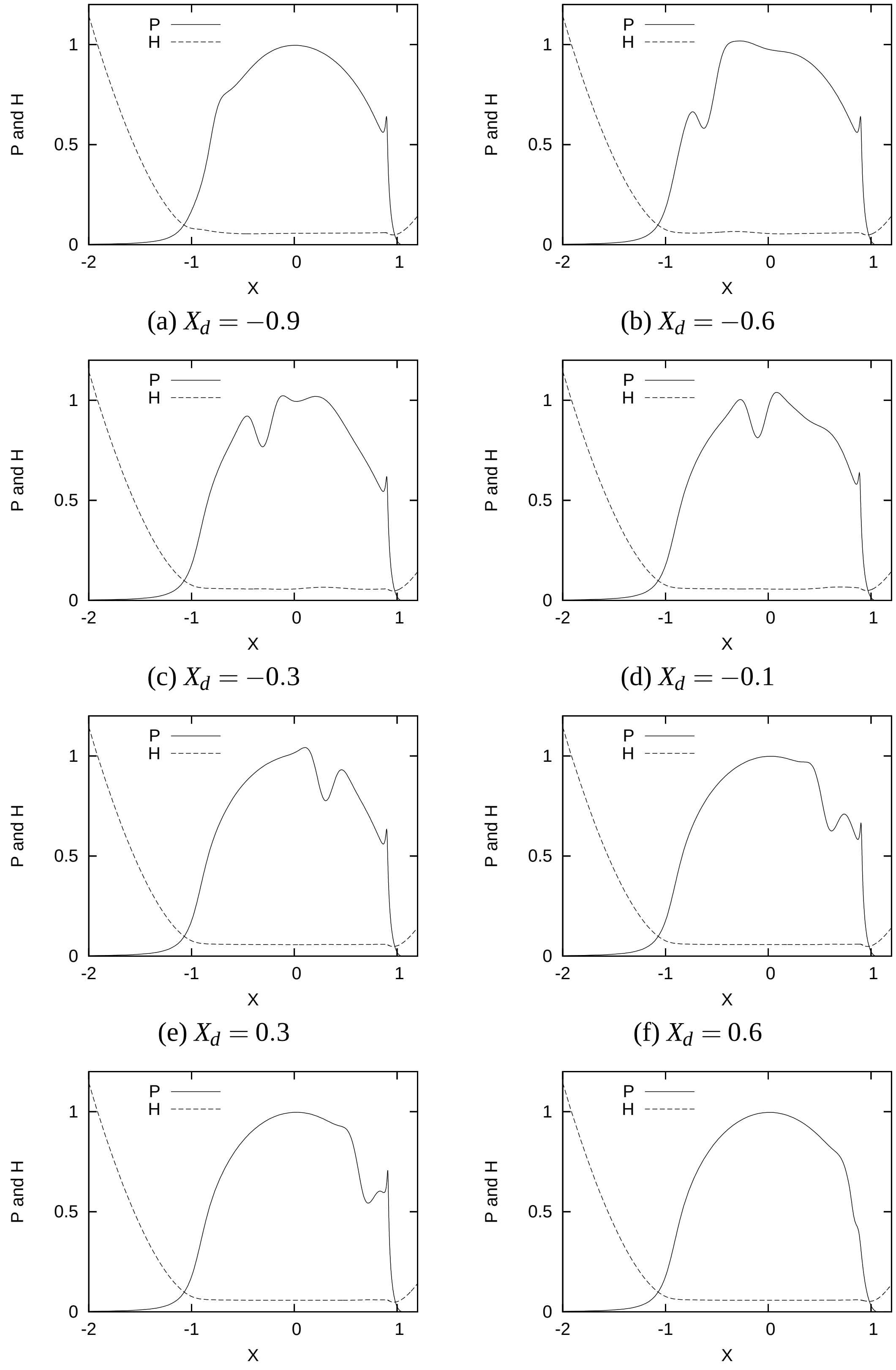

(a) $X_d = -0.9$ (b) $X_d = -0.6$

(c) $X_d = -0.3$ (d) $X_d = -0.1$

(e) $X_d = 0.3$ (f) $X_d = 0.6$

(g) $X_d = 0.7$ (h) $X_d = 0.9$

Figure 5.11: Non-dimensional P and H obtained using the DG simulation with "Roughness 3"

The above results are all based on a simple “dent” roughness model. A simple “bump” roughness model (“Roughness 4”) is easy to construct by changing the sign of “Roughness 2” in equation (5.19):

$$\mathscr{R}(X,T) = \alpha 10^{-40((X-X_d))^2} \cos(4\pi(X-X_d)), \tag{5.23}$$

where $\alpha = 0.04$ and other parameters remain the same as in equation (5.19).

Here $\theta = 0$ and 12th-order DG are used to simulate this “bump” roughness case. $\triangle T = 0.001$ for $X_d < 0.8$ and $\triangle T = 0.0001$ for $X_d \geq 0.8$. From (a) to (g) in Figure 5.12, a “bump” in pressure is produced by the “bump” roughness. In Figure 5.12 (h), the interaction between the “bump” roughness and the original “dent” in film thickness around the “the Petrusevich spike” gives a very high pressure spike.

5.7 Conclusion

In this chapter, the high order DG method introduced for the solution of steady-state problems in the previous chapters is extended to solve transient line contact EHL problems. The Crank-Nicolson method and slightly more implicit schemes are used for the temporal discretization. In order to ensure both accuracy and an acceptable computational cost, a new h-adaptivity scheme is introduced based on the properties of the hierarchical basis functions.

Through the high accuracy of the DG method and its flexibility in adaptivity, numerical results show that additional details of the solution may be captured in some cases, compared to the traditional finite difference method for which a uniform grid is used. Particularly, due to the roughness profile, a micro-EHL pressure spike has been captured in addition to the well-known “Petrusevich Spike” using fewer than 540 degrees of freedom.

So far relatively little effort has been put into optimizing the computational efficiency for 1d transient EHL problems. For example, once the grid is adjusted, part of $K_i^e(X)$ and KK_i^e need to be updated. For the convenience of implementation, we recalculated all of them, which increases the computational expense. Consequently it can take as much as 3 weeks to finish about 16000 time steps! The efficiency could be better if we improved the efficiency of the computation of the kernels $K_i^e(X)$ and KK_i^e, but in this thesis, we currently focus on the accuracy.

Another way to improve the efficiency and control the error is by using automatic adaptive time-stepping [6]. In this chapter, we currently focus on the transient solution details. Since the used roughness models are relatively simple, it is not difficult to tell

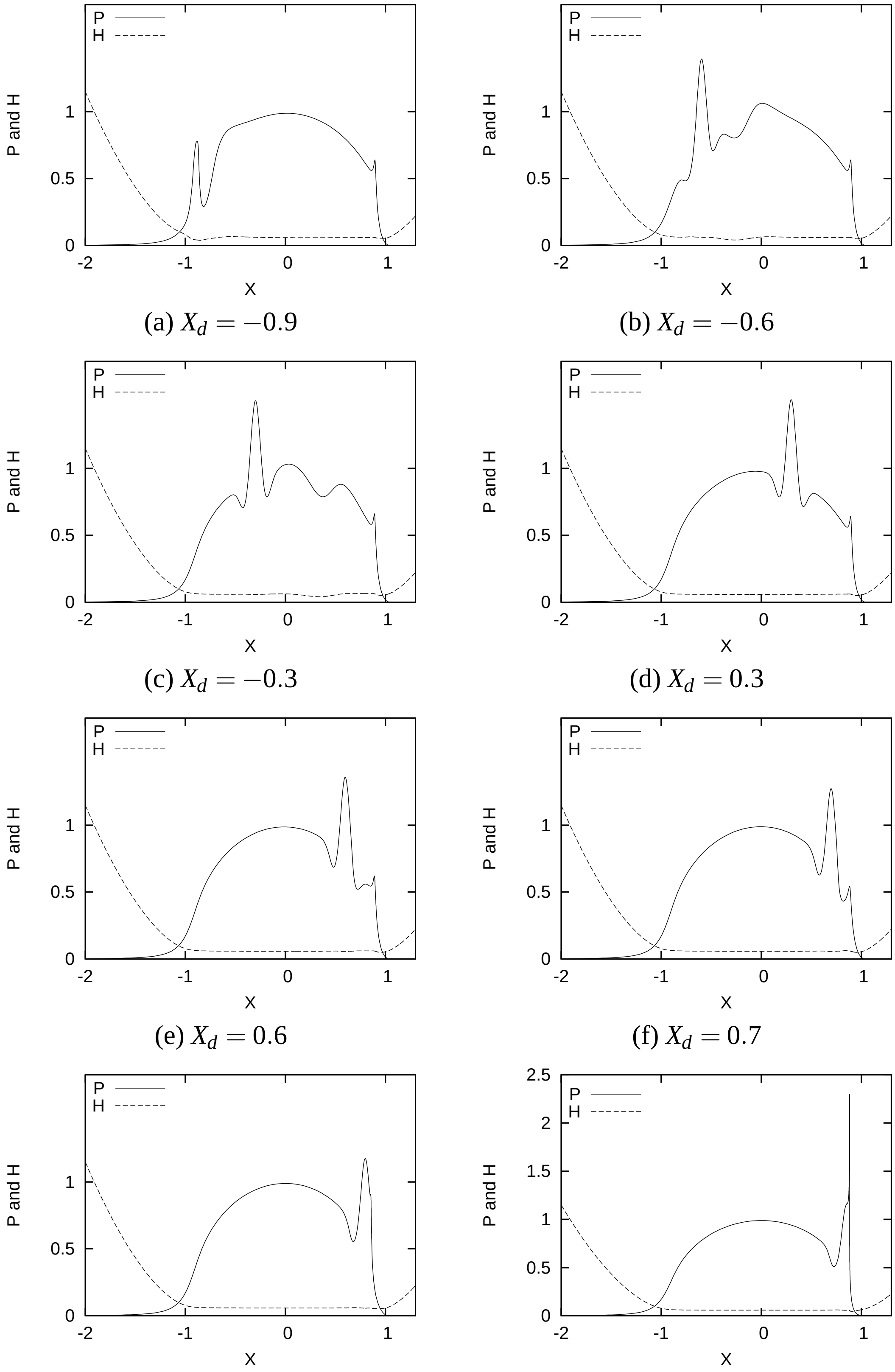

(a) $X_d = -0.9$ (b) $X_d = -0.6$

(c) $X_d = -0.3$ (d) $X_d = 0.3$

(e) $X_d = 0.6$ (f) $X_d = 0.7$

(g) $X_d = 0.8$ (h) $X_d = 0.85$

Figure 5.12: Non-dimensional P and H obtained using the DG simulation with “Roughness 4”

when we should adjust the time step to ensure the solution quality. However, if the roughness model is more complicated, automatic time-stepping has to be used to ensure the accuracy and to improve the efficiency.

For the low-order temporal discretization used in this chapter, numerical results indicate that relatively small time steps have to be used to ensure the accuracy. The efficiency and accuracy of the time-stepping may benefit from using some higher order temporal discretization [13, 14].

Chapter 6

High Order DG Solution of Steady-State Point Contact Problems

6.1 Introduction

In this chapter, the application of the high-order DG method introduced in the previous chapters is extended to the two-dimensional case. The two-dimensional Reynolds equation (1.26) is discretized using high-order DG. For the convenience of evaluating the film thickness (1.27), and solving the two-dimensional force balance equation (1.28), some two-dimensional kernels (similar to those introduced in the 1d case-see equations (4.15) and (4.26)) are introduced. The h-adaptivity method developed in the 1d case, which is based on the contributions of the high-order components of the pressure is also extended to the two-dimensional case. The penalty method [64] has to be employed to capture the cavitation boundary in the two-dimensional case. Furthermore, a multi-level technique, p-multigrid [24], is used to accelerate the convergence since the computation in two dimensions is much more expensive than in one dimension. Rather than using different grids at different levels, p-multigrid uses different polynomial orders but on the same grid. Both low-frequency errors and high-frequency errors, which correspond to low degree modes and high degree modes respectively, can be eliminated quickly by relaxing the solution on different levels.

6.2 Discretization

In this section, the high-order discretization of the two-dimensional Reynolds equation, film thickness equation and the force balance equation are given.

6.2.1 The Reynolds Equation

The two-dimensional, dimensionless, steady-state Reynolds equation (1.26) is given in Chapter 1. For the convenience of describing the discretization of the steady-state equation we write it in the following general form in the two-dimensional case:

$$-\nabla\cdot(\varepsilon\nabla P)+\nabla\cdot(\beta\bar{\rho}H)=0, \tag{6.1}$$

where the cavitation condition $P\geq 0$ must hold in the computational domain and $P=0$ on the boundaries. In (6.1) $\varepsilon=\frac{\bar{\rho}(P)H^3}{\bar{\eta}(P)\lambda}$, $\beta=(1,0)^T$, and $\bar{\rho}(P)$ and $\bar{\eta}(P)$ are calculated using the density model of Dowson and Higginson (1.30) and the viscosity-pressure model of Roelands (1.29) respectively. It is necessary to introduce some additional notation before describing the discretization of (6.1).

Let $\mathscr{P}_h$ be a partition of the rectangular domain Ω into N rectangular elements Ω_e. Moreover, let $\Gamma_{int}=\cup\Gamma_{ef}$ where Γ_{ef} represents each internal interface,

$$\Gamma_{ef}=\partial\Omega_e\cap\partial\Omega_f \tag{6.2}$$

with $e>f$, and let $\hat{n}$ be the unit normal pointing from Ω_e to Ω_f. Let Γ_D be the boundary of Ω, which is taken to be a Dirichlet boundary where $P=g$. Let Γ_- be the inflow part of the boundary, which is the part of Γ_D for which $\hat{n}\cdot\beta<0$ in the two-dimensional case, where $\hat{n}$ is the outward normal from the computational domain. Here g is the solution on the Dirichlet boundary and for EHL problems of the form (6.1) $g=0$.

The jump of a function v at point $X=(x,y)$ on the element interface Γ_{ef} is defined to be

$$[v]_{ef}(X)=v(X)|_{\partial\Omega_e\cap\Gamma_{ef}}-v(X)|_{\partial\Omega_f\cap\Gamma_{ef}},\; e>f, \tag{6.3}$$

and the average is given by

$$\langle v(X)\rangle_{ef}=\frac{1}{2}\left(v(X)|_{\partial\Omega_e\cap\Gamma_{ef}}+v(X)|_{\partial\Omega_f\cap\Gamma_{ef}}\right). \tag{6.4}$$

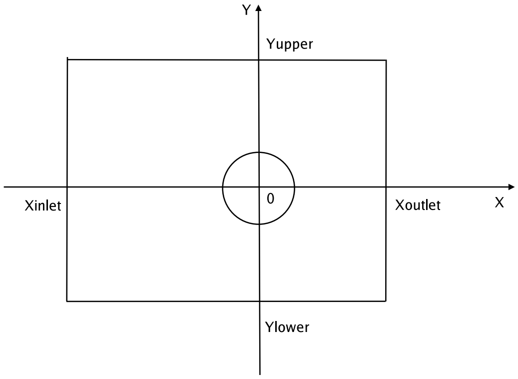

Figure 6.1: Computational domain used for the DG discretization of equations ((1.20), (1.21) and (1.22))

In each element e, Let P be expressed in the following form:

$$P^e(X) = \sum_{i=1}^{n(p^e)} u_i^e N_i^e(X), \tag{6.5}$$

where p^e is the order of the approximating polynomial, $n(p^e)$ is the number of basis functions, u_i^e are the unknown coefficients and $N_i^e(X)$ are the local finite element basis functions which belong to a finite element space V. As for the one-dimensional case, in this chapter, *hierarchical* basis functions are used, based on the definitions in [58]. These functions consist of “nodal modes”, “side modes” and “internal modes”. One important property of these basis functions is that the $(p+1)^{th}$ degree basis functions can be easily obtained by adding several higher order basis functions to the p^{th} degree basis. Then P^e can also be written as follows:

$$P^e(X) = \sum_{p=1}^{p^e} \sum_{j=1}^{m(p)} u_j^{e,p} N_j^{e,p}(X), \tag{6.6}$$

where $N_j^{e,p}(X)$ is the basis function that corresponds to degree p. From equations (6.5) and (6.6), it follows that

$$n(p^e) = \sum_{p=1}^{p^e} m(p). \tag{6.7}$$

Figure 6.2 demonstrates the first 4 basis functions, which correspond to degree 1 “nodal modes”, on the reference element where $X = (x, y)$, $x \in [-1:1]$ and $y \in [-1:1]$. For any $p > 1$, the first 4 $N_j^{e,p}$ in equation (6.6) are “side modes”, which are shown in Figure 6.3. The other basis functions $N_j^{e,p}$ ($5 \le j \le m(p)$, where $m(p) = p+1$) corresponding to $p \ge 4$ are called “internal modes”, which are displayed in Figure 6.4.

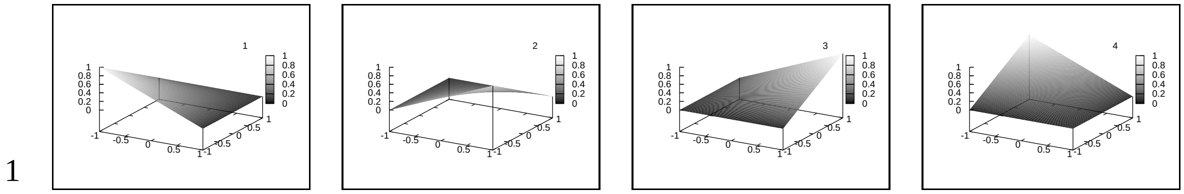

Figure 6.2: Nodal modes for the hierarchical basis

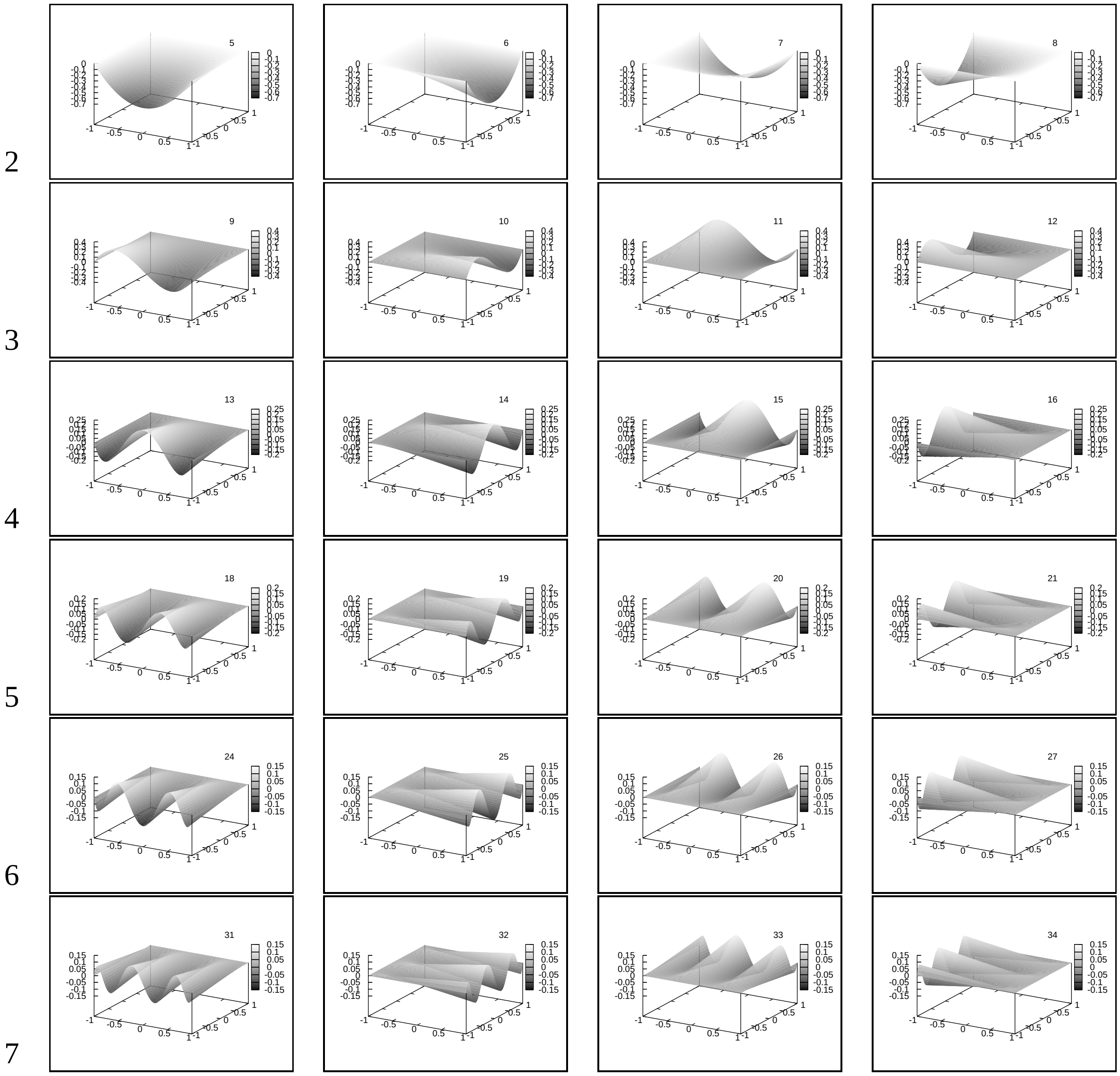

Figure 6.3: Side modes for the hierarchical basis

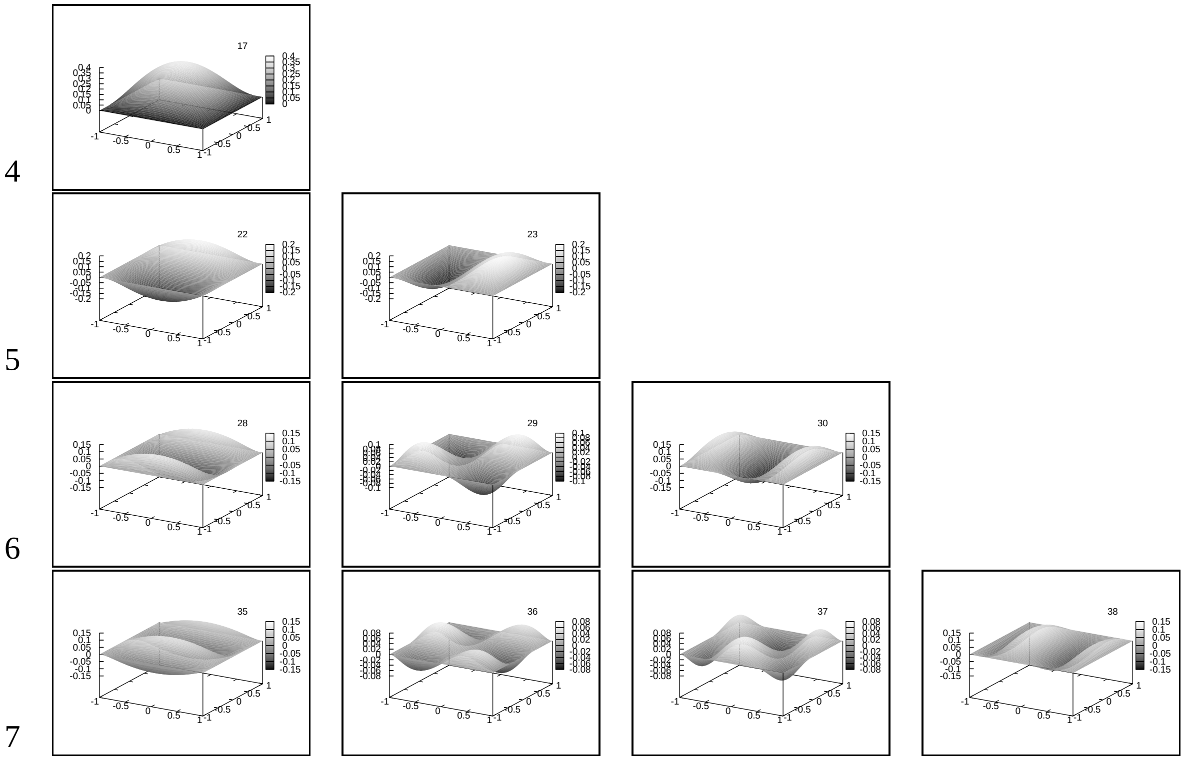

Figure 6.4: Internal modes for the hierarchical basis

Following the approach of [5, 45], a discrete form of the two-dimensional steady-state Reynolds equation becomes:

$$L(P,v) = a(P,v) - l(P,v) = 0,\ \forall v \in V, \tag{6.8}$$

where

$$\begin{aligned} a(P,v) &= \sum_{\Omega_e \in \mathscr{P}_h} \left(\int_{\Omega_e} \nabla v \cdot \varepsilon \nabla P \, \mathrm{d}X \right) \\ &+ \int_{\Gamma_{int}} \left([P] \left\langle (\varepsilon \nabla v) \cdot \hat{n} \right\rangle - [v] \left\langle (\varepsilon \nabla P) \cdot \hat{n} \right\rangle \right) \mathrm{d}s \\ &+ \int_{\Gamma_D} \left(P (\varepsilon \nabla v) \cdot \hat{n} - v (\varepsilon \nabla P) \cdot \hat{n} \right) \mathrm{d}s, \end{aligned} \tag{6.9}$$

and

$$\begin{aligned} l(P,v) &= \sum_{\Omega_e \in \mathscr{P}_h} \left(\int_{\Omega_e} (\nabla v \cdot \beta) \bar{\rho} H \, \mathrm{d}X \right) - \int_{\partial \Omega_e \setminus \Gamma_-} v \bar{\rho}(P^-) H \left(\beta \cdot \tilde{n}_e \right) \mathrm{d}s \\ &- \int_{\Gamma_-} v \bar{\rho}(g) H \left(\beta \cdot \hat{n} \right) \mathrm{d}s + \int_{\Gamma_D} (g \varepsilon \nabla v) \cdot \hat{n} \, \mathrm{d}s. \end{aligned} \tag{6.10}$$

In the above equations,

$$P^- = \lim_{\delta \to 0} P(X - \delta\beta), \text{ for } X \in \Gamma_{int}, \tag{6.11}$$

and $\tilde{n}_e$ is the outward-pointing normal from Ω_e. Note that sufficient upwinding has been incorporated through the choice of $\bar{\rho}(P^-)$ when calculating the numerical flux over element boundaries [5].

The term $\int_{\Gamma_{int}} [v] \langle (\varepsilon \nabla P) \cdot \hat{n} \rangle \, \mathrm{d}s$ in equation (6.9) is nonzero since a discontinuity is allowed over element boundaries, whilst the desired continuity of P over element boundaries is weakly enforced by

$$\int_{\Gamma_{int}} [P] \langle (\varepsilon \nabla v) \cdot \hat{n} \rangle \, \mathrm{d}s = 0 \tag{6.12}$$

in equation (6.9). Dirichlet boundary conditions are also imposed weakly since the last integrals in (6.9) and (6.10) include the additional constraint:

$$\int_{\Gamma_D} (P - g) \langle (\varepsilon \nabla v) \cdot \hat{n} \rangle \, \mathrm{d}s = 0. \tag{6.13}$$

For all problems considered in this chapter $g = 0$, which is reasonable so long as the upstream and span-wise boundaries are sufficiently far from the contact region (see Figure 6.1).

6.2.2 The Film Thickness Equation

Similar to the 1d case, a new kernel is introduced for the convenience of calculating the two-dimensional film thickness. For a given pressure distribution the film thickness may be calculated as follows:

$$\begin{aligned} H(x,y) &= H_{00} + \frac{x^2}{2} + \frac{y^2}{2} \\ &+ \frac{2}{\pi^2} \int_{Y_{lower}}^{Y_{upper}} \int_{X_{inlet}}^{X_{outlet}} \frac{P(x',y')}{\sqrt{(x-x')^2 + (y-y')^2}} \, \mathrm{d}x' \mathrm{d}y' \\ &= H_{00} + \frac{x^2}{2} + \frac{y^2}{2} + \frac{2}{\pi^2} \sum_{e=1}^{N} \sum_{i=1}^{n(p^e)} K_i^e(x,y) u_i^e, \end{aligned} \tag{6.14}$$

where, using (6.5),

$$K_i^e(x,y) = \int_{\Omega_e} \frac{N_i^e(x',y')}{\sqrt{(x-x')^2 + (y-y')^2}} \, \mathrm{d}x' \mathrm{d}y'. \tag{6.15}$$

In this work $K_i^e(x,y)$ is calculated using numerical quadrature due to its complexity. Special care must be taken when $(x,y) \in \Omega_e$ due to the nature of the integrand, and so singular quadrature [20] has to be used. Gaussian quadrature can be employed elsewhere. Note that $K_i^e(x,y)$ depends on both the structure of the FE grid and on the basis functions that are used.

When evaluating the integrals in equation (6.9) and (6.10) over elements and element boundaries, Gaussian quadrature is used. Hence, the value of the film thickness H needs to be calculated for every quadrature point in each element and on each element boundary. In order to do this, values of $K_i^e(x,y)$ must be evaluated at each quadrature point. Note however that, for a given grid, a given set of basis functions, and a given set of quadrature points, these kernels, $K_i^e(x,y)$, only need to be evaluated once.

If (x,y) is located outside e, Gaussian quadrature [20, 58] is used to compute $K_i^e(x,y)$ (note that we use rectangular elements aligned with the axes in the two-dimensional case):

$$\begin{aligned} K_i^e(x,y) &= \int_{\Omega_e} \frac{N_i^e(x',y')}{\sqrt{(x-x')^2+(y-y')^2}}\,\mathrm{d}x'\mathrm{d}y' \\ &= \frac{h_x^e}{2}\frac{h_y^e}{2}\int_{-1}^{1}\int_{-1}^{1} \frac{N_i^e(x'(\xi,\eta),y'(\xi,\eta))}{\sqrt{\left(x-x'(\xi,\eta)\right)^2+\left(y-y'(\xi,\eta)\right)^2}}\,\mathrm{d}\xi\,\mathrm{d}\eta \\ &= \frac{h_x^e}{2}\frac{h_y^e}{2}\sum_{j=1}^{m}\sum_{k=1}^{m}\left(\frac{N_i^e(x'(\xi_j,\eta_k),y'(\xi_j,\eta_k))}{\sqrt{\left(x-x'(\xi_j,\eta_k)\right)^2+\left(y-y'(\xi_j,\eta_k)\right)^2}}\right) w_j w_k, \quad (6.16) \end{aligned}$$

where h_x^e and h_y^e are the sizes of element e in the x direction and y direction respectively and m-point quadrature is applied in each direction. Furthermore, as shown in Figure 6.5,

$$h_x^e = x_2 - x_1; \quad (6.17)$$

$$h_y^e = y_2 - y_1, \quad (6.18)$$

where $\xi \in [-1,1]$ and $\eta \in [-1,1]$ are the coordinate directions for the reference element. When (x,y) is inside e, as demonstrated in Figure 6.6, where element e is divided into 4 smaller elements ($f_k, k = 1,2,3,4$), singular quadrature can be employed to evaluate $K_i^e(x,y)$ since $\frac{1}{(x-x')^2+(y-y')^2}$ has a singularity at (x,y). First, we rewrite $K_i^e(x,y)$ as fol-

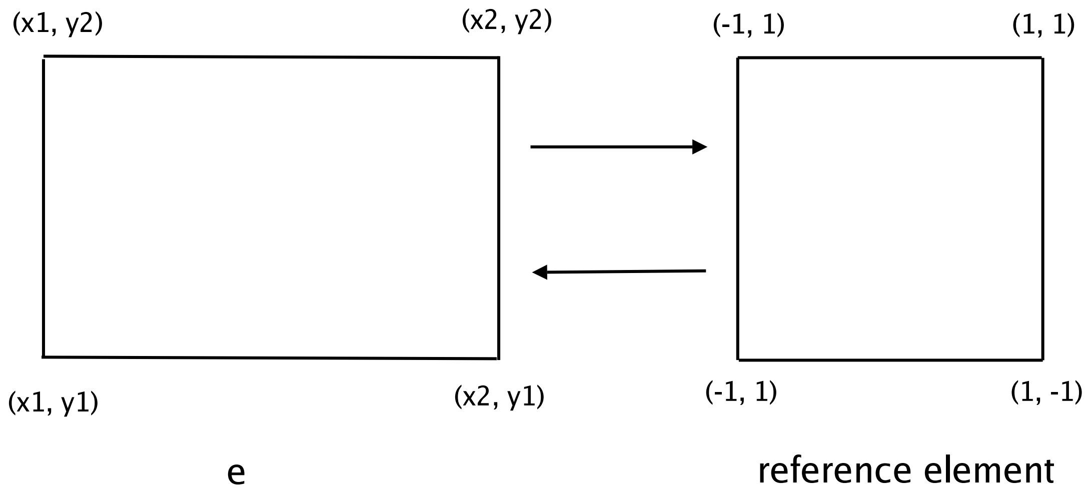

Figure 6.5: Coordinate mapping between the reference element and the local element *e*

lows:

$$\begin{aligned} K_i^e(x,y) &= \int_{\Omega_e} \frac{N_i^e(x^{'},y^{'})}{\sqrt{(x-x^{'})^2+(y-y^{'})^2}}\,\mathrm{d}x^{'}\mathrm{d}y^{'} \\ &= \sum_{k=1}^{4}\int_{f_k} \frac{N_i^e(x^{'},y^{'})}{\sqrt{(x-x^{'})^2+(y-y^{'})^2}}\,\mathrm{d}x^{'}\mathrm{d}y^{'} \\ &= \sum_{k=1}^{4}(K_i^e(x,y))^{f_k}, \end{aligned} \tag{6.19}$$

where the sub-elements f_k $(k=1,2,3,4)$ are shown in Figure 6.6 and

$$(K_i^e(x,y))^{f_k} = \int_{f_k} \frac{N_i^e(x^{'},y^{'})}{\sqrt{(x-x^{'})^2+(y-y^{'})^2}}\,\mathrm{d}x^{'}\mathrm{d}y^{'}. \tag{6.20}$$

Similar to equation (4.18), $(K_i^e(x,y))^{f_k}$ can be written in the following general form:

$$\left(K_i^e(x^{'},y^{'})\right)^{f_k} = S = \int_0^1\int_0^1 f(x^{'},y^{'})q(x^{'},y^{'})\,\mathrm{d}x^{'}\mathrm{d}y^{'}, \tag{6.21}$$

where $q(x^{'},y^{'})$ (corresponding to $N_i^e(x^{'},y^{'})$ in (6.20)) is analytic and $f(x^{'},y^{'})$ (corresponding to $\frac{1}{\sqrt{(x-x^{'})^2+(y-y^{'})^2}}$) is singular at $(0,0)$. S is evaluated using singular quadrature (see Figure 6.7) as follows:

$$S \approx S_n = \sum_{i=1}^{n} T_i, \tag{6.22}$$

where T_i can be calculated by summing over the three rectangular regions shown in Fig-

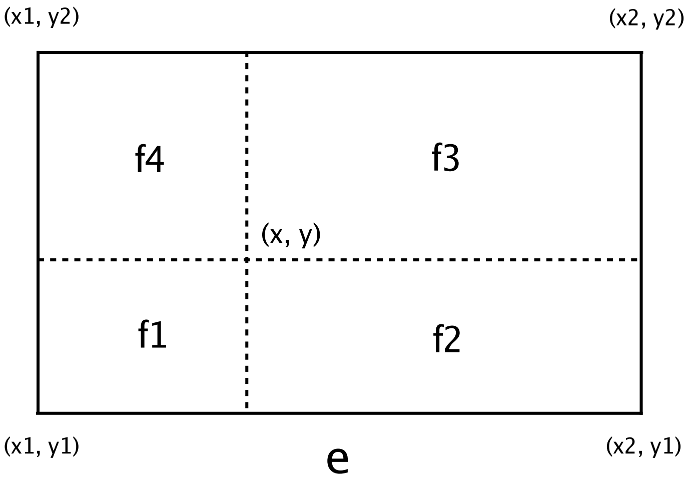

Figure 6.6: Singular quadrature is used when $(x,y) \in e$

ure 6.7:

$$\begin{aligned} T_i &= \int_0^{x_i'} \int_{y_i'}^{y_{i-1}'} f(x',y')q(x',y')\,\mathrm{d}x'\mathrm{d}y' + \int_{x_i'}^{x_{i-1}'} \int_{y_i'}^{y_{i-1}'} f(x',y')q(x',y')\,\mathrm{d}x'\mathrm{d}y' \\ &+ \int_{x_i'}^{x_{i-1}'} \int_0^{y_i'} f(x',y')q(x',y')\,\mathrm{d}x'\mathrm{d}y'. \end{aligned} \tag{6.23}$$

The integrals in equation (6.23) are calculated using Gaussian quadrature. Here $x_0 = 1$, $y_0 = 1$ and $x_i \to 0$, $y_i \to 0$ as $i \to \infty$. In this thesis, the following monotonic decreasing sequence $\{x_i, y_i\}$ is used:

$$x_i = \theta^i, \tag{6.24}$$

$$y_i = \theta^i,\ (0 < \theta < 1) \tag{6.25}$$

where $\theta = 0.2$ is employed.

Note that both $K_i^e(x,y)$ and $K_i^f(x,y)$ are computed using singular quadrature (see Figure 6.8) when (x,y) is on edge Γ_{ef}.

These kernels can all be precomputed given a grid and a set of basis functions. Note however that a large amount of memory is required to store the values of these kernels. If we have N elements and M edges in the computational domain and m-point quadrature is used, there will be $(N \times m^2 + M \times m) \times \sum_{e=1}^{N} n(p^e)$ double precision values to store.

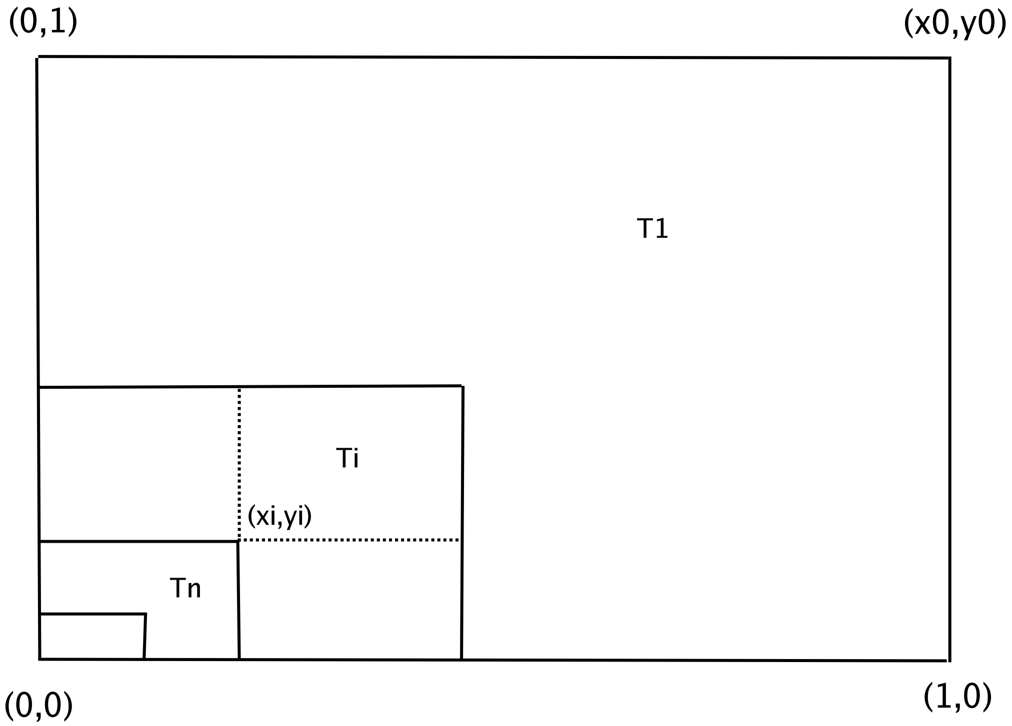

Figure 6.7: Two-dimensional singular quadrature

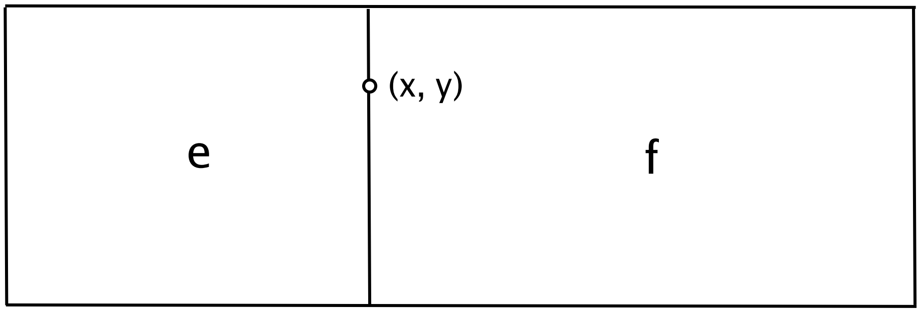

Figure 6.8: Singular quadrature is used to calculate $K_i^e(x,y)$ and $K_i^f(x,y)$ when $(x,y) \in \Gamma_{ef}$

6.2.3 The Force Balance Equation

Using (6.5), the discrete form of the force balance equation (1.28) is given by:

$$\sum_{e=1}^{N}\left(\int_{\Omega_e}\sum_{i=1}^{n(p^e)} u_i^e N_i^e(x,y)\,\mathrm{d}x\mathrm{d}y\right)-\frac{2\pi}{3}=0. \tag{6.26}$$

Hence it is possible to define a two-dimensional kernel by:

$$G_i^e=\int_{\Omega_e} N_i^e(x,y)\,\mathrm{d}x\mathrm{d}y, \tag{6.27}$$

to yield the following form:

$$\sum_{e=1}^{N}\sum_{i=1}^{n(p^e)} G_i^e u_i^e-\frac{2\pi}{3}=0. \tag{6.28}$$

Again this kernel can be precomputed using Gaussian quadrature for a given grid and a given set of basis functions.

6.3 Penalty Method

In Chapter 4 it was demonstrated that the penalty method of Wu, [64], can provide accurate results for the one-dimensional problems considered. This approach extends naturally to the two-dimensional problems considered here and so it is used throughout this chapter. The consequence of introducing an exterior penalty term is to modify the discrete system (6.8) so that it becomes:

$$L(P,v)=a(P,v)+\frac{1}{\delta}\int_{\Omega} P_{-}v\,\mathrm{d}\Omega-l(P,v)=0,\ \forall v\in V, \tag{6.29}$$

where δ is an arbitrary small positive number ($\delta=1.0\times10^{-7}$ in the calculations used in this chapter) and

$$P_{-}=min(P,0). \tag{6.30}$$

Note that the penalty term $\frac{1}{\delta}\int_{\Omega}P_{-}v\,\mathrm{d}\Omega$ is only effective when $P<0$ and it dominates the equation (6.29) in this case since δ is very small. When P would have been negative, these negative pressures are forced to be zero by the presence of the penalty term in this modified weak form. The physical constraint that $P\geq0$ over the entire computational domain is therefore satisfied automatically in a weak sense.

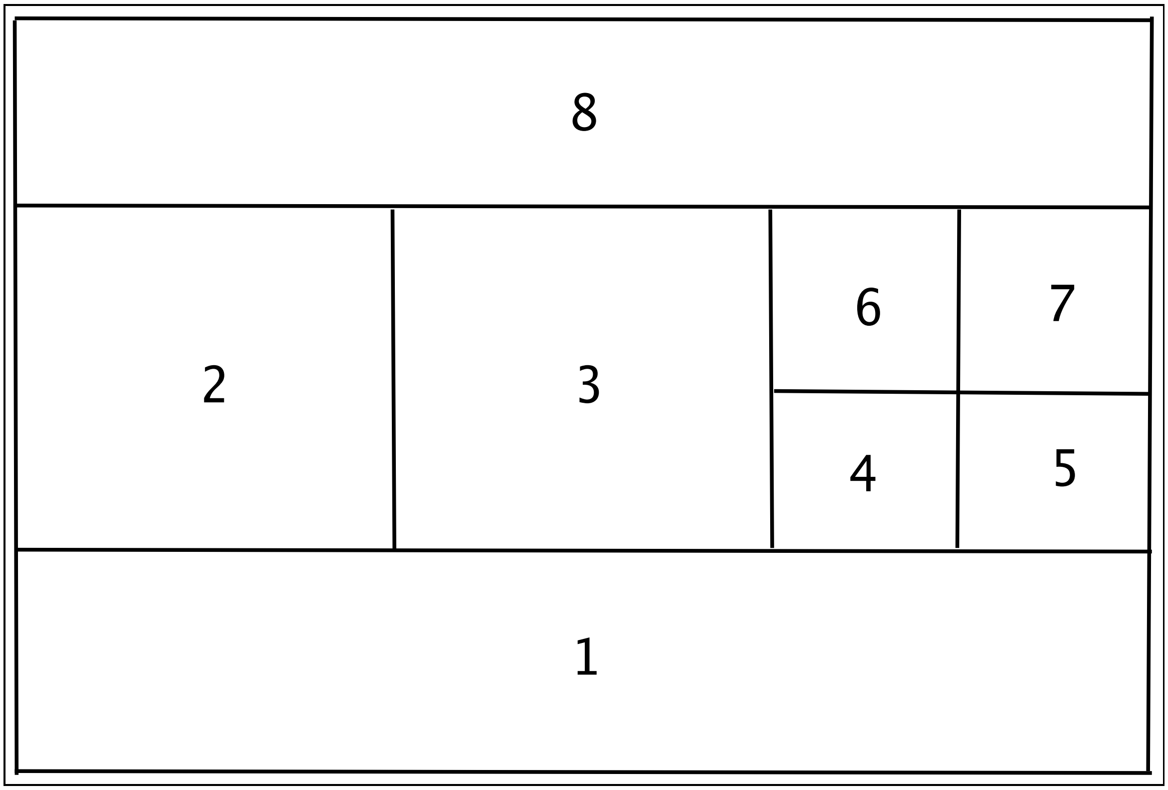

Figure 6.9: A simple adaptive grid

6.4 Relaxation

Using (6.5) and using the basis functions as the test functions, the steady-state equation (6.29) can be written in the following general nonlinear algebraic form:

$$L(U) = A(U)U - b(U) = 0, \tag{6.31}$$

where

$$U = \left(u_1^1, \ldots, u_{n(p^1)}^1; \ldots; u_1^N, \ldots, u_{n(p^N)}^N\right)^T. \tag{6.32}$$

Note that both $A(U)$ and $b(U)$ depend on U. Since the entries of U are ordered element by element, $A(U)$ is a sparse block matrix with non-zero blocks on the diagonal and block entries for block row e and block column f wherever e and f are neighbours (since each element e is connected with its neighbouring elements through the element boundaries, see Equation (6.9)).

$$\begin{bmatrix} A_{1,1} & A_{1,2} & A_{1,3} & A_{1,4} & A_{1,5} & 0 & 0 & 0 \\ A_{2,1} & A_{2,2} & A_{2,3} & 0 & 0 & 0 & 0 & A_{2,8} \\ A_{3,1} & A_{3,2} & A_{3,3} & A_{3,4} & 0 & A_{3,6} & 0 & A_{3,8} \\ A_{4,1} & 0 & A_{4,3} & A_{4,4} & A_{4,5} & A_{4,6} & 0 & 0 \\ A_{5,1} & 0 & 0 & A_{5,4} & A_{5,5} & 0 & A_{5,7} & 0 \\ 0 & 0 & A_{6,3} & A_{6,4} & 0 & A_{6,6} & A_{6,7} & A_{6,8} \\ 0 & 0 & 0 & 0 & A_{7,5} & A_{7,6} & A_{7,7} & A_{7,8} \\ 0 & A_{8,2} & A_{8,3} & 0 & 0 & A_{8,6} & A_{8,7} & A_{8,8} \end{bmatrix} \qquad (6.33)$$

A simple iterative procedure for solving this nonlinear algebraic system is to use the following quasi-Newton relaxation:

$$U \leftarrow U + \left(\frac{\partial L(U)}{\partial U}\right)^{-1} R, \qquad (6.34)$$

where R is the numerical residual of the discrete Reynolds equation ($R = -L$) and $\frac{\partial L(U)}{\partial U}$ is approximated by:

$$\begin{aligned} \frac{\partial L(U)}{\partial U} &= \frac{\partial}{\partial U}(A(U)U) - \frac{\partial b(U)}{\partial U} \\ &\approx A(U) - \frac{\partial b(U)}{\partial U}. \end{aligned} \qquad (6.35)$$

Note that $\frac{\partial b(U)}{\partial U}$ is a full matrix which can itself be computed by:

$$\begin{aligned} \frac{\partial b(U)}{\partial U}\Big|_{I,J} &= \frac{\partial b(U)_i^e}{\partial U_j^f} \\ &= \sum_{\Omega_e \in \mathscr{P}_h} \left(\int_{\Omega_e} (\nabla v \cdot \beta) \left(\bar{\rho} \frac{\partial H}{\partial U_j^f} + \frac{\partial \bar{\rho}}{\partial U_j^f} H \right) \mathrm{d}X \right) \\ &- \int_{\partial\Omega_e \setminus \Gamma_-} v \left(\bar{\rho}(P^-) \frac{\partial H}{\partial U_j^f} + \frac{\partial \bar{\rho}(P^-)}{\partial U_j^f} H \right) (\beta \cdot \tilde{n}_e)\, \mathrm{d}s \\ &- \int_{\Gamma_-} v \bar{\rho}(g) \frac{\partial H}{\partial U_j^f} (\beta \cdot \hat{n})\, \mathrm{d}s, \end{aligned} \qquad (6.36)$$

where the Ith row corresponds to the row generated with the test function $v = N_i^e(X)$ and the Jth column corresponds to the unknown U_j^f. Note that, according to the discrete film thickness equation (6.14),

$$\frac{\partial H(x,y)}{\partial U_j^f} = K_j^f(x,y), \tag{6.37}$$

which can be precomputed.

It is important to note from (6.14) that the film thickness depends heavily on the local pressures and much less on the pressures far away. Thus, in (6.37), $K_j^f(x,y)$ is small when the position of element f is far away from the position of $X = (x,y)$. This provides useful information with which to make a further simplification to the approximation of $\frac{\partial b(U)}{\partial U}$. Here we use the following approximations:

1. $\frac{\partial H(X)}{\partial U_j^f} = 0$ where $X \in e$ if $f \neq e$ and f is not a neighbour of e.
2. $\frac{\partial H(X)}{\partial U_j^f} = 0$ where $X \in \Gamma_{int}$ if f is not a neighbour of Γ_{int}.
3. $\frac{\partial H(X)}{\partial U_j^f} = 0$ where $X \in \Gamma_D$ if f is not a neighbour of Γ_D.
4. $\frac{\partial H(X)}{\partial U_j^f} = K_j^f(X)$, otherwise.

As we did in Chapter 4 for the one-dimensional case, the above principles lead to the fact that $\frac{\partial b(U)}{\partial U}$ may be approximated by a block sparse matrix of the same sparsity as $A(U)$. As a result, $\frac{\partial L(U)}{\partial U}$ in (6.35) is also approximated by a block sparse matrix. An advantage of this simplification is that it is only necessary to evaluate a relatively small number of the entries of $\frac{\partial b(U)}{\partial U}$ instead of calculating all of them, yet the relaxation (6.34) is only affected in a relatively minor way. Consequently, when updating the unknown U in (6.34), the following linear system is solved numerically rather than calculating $\left(\frac{\partial L(U)}{\partial U}\right)^{-1}$ precisely:

$$\left(\frac{\partial \hat{L(U)}}{\partial U}\right) U_{correction} = R, \tag{6.38}$$

where U is the current solution, $\left(\frac{\partial \hat{L(U)}}{\partial U}\right)$ is the approximation to $\frac{\partial L(U)}{\partial U}$ described above and $U_{correction}$ is the correction value to U. There are many methods which can be used to solve this linear system. In this work, at each iteration we use a sparse GMRES implementation [56], along with an under-relaxation version of (6.34), as described in Section 6.4, to improve robustness:

$$U = U + C_1 U_{correction}, \tag{6.39}$$

where C_1 is an under-relaxation factor.

Finally, in order to satisfy the force balance equation, we update H_{00} as follows:

$$H_{00} \leftarrow H_{00} - C_2 \left(\frac{2\pi}{3} - \sum_{e=1}^{N} \sum_{i=1}^{n(p^e)} G_i^e u_i^e \right), \tag{6.40}$$

where C_2 is another under-relaxation factor for H_{00}. The overall solution procedure is presented in Section 6.7 but first we introduce two important components to improve the efficiency of the method.

6.5 P-multigrid

Multilevel techniques (multigrid methods and multi-level multi-integration) play a very important role when the finite difference method is used to solve EHL contact problems. Multigrid methods accelerate convergence and make it possible to obtain a converged solution with a huge number of grid points in a relatively short time [25, 26, 60]. When using high-order DG to solve line contact problems in Chapters 4 and 5, we do not use any multi-level technique because the computation is not very expensive, since it usually requires only several hundreds of degrees of freedom to capture every detail in the solution. However, point contact problems are more complicated and more degrees of freedom are required due to the additional dimension. As a result, the computation becomes more expensive.

P-multigrid [24] is a multi-level technique suitable for high-order DG methods. Rather than using different spatial grids on different levels, p-multigrid uses different polynomial degrees but on the same spatial grid. The low frequency modes and the high frequency modes correspond to the low degree and the high degree components respectively. Here the low degree interpolants serve as “coarse” levels. Both high frequency errors and low frequency errors can be eliminated effectively by relaxing on both “fine” and “coarse” levels. For convenience, a brief introduction to the two-level full approximation scheme (FAS) is given in this section.

6.5.1 FAS for P-multigrid

Consider the following nonlinear system which results from a degree p FE discretization of a PDE:

$$\mathscr{L}^p(u^p) = f^p, \tag{6.41}$$

where u^p is the discrete solution vector for the p^{th} degree piecewise polynomials on a given grid, $\mathscr{L}^p(u^p)$ is the associated nonlinear system and f^p is a source term ($f^p = 0$ on the finest level). The discrete residual is defined by:

$$r^p = f^p - \mathscr{L}^p(u^p). \tag{6.42}$$

Let $q < p$ and let u^q denote the coefficients of a coarse level q^{th} degree piecewise polynomial approximation. The two-level correction scheme is given as follows:

1. Restrict the state and the residual to the coarse level:

$$u_0^q = \tilde{I}_p^q u^p, \tag{6.43}$$

$$r^q = I_p^q r^p. \tag{6.44}$$

2. Solve the coarse grid problem:

$$\mathscr{L}^q(u^q) = f^q = \mathscr{L}^q(u_0^q) + r^q. \tag{6.45}$$

3. Interpolate the correction from the coarse level to the fine level and correct the fine level state:

$$e^p = I_q^p(u^q - u_0^q), \tag{6.46}$$

$$u^p = u^p + e^p. \tag{6.47}$$

I_p^q is the residual restriction operator and $\tilde{I}_p^q$ is the state restriction operator (which need not necessarily be the same) and I_q^p is the state prolongation operator.

In practice, normally more than 2 levels are used to eliminate various frequency errors effectively. In this general case, the recursive coarse grid correction for level k reads:

- If level $k = 1$ (the coarsest level), perform v_0 relaxation sweeps to solve the problem nearly exactly.
- If $k > 1$,
  - Perform v_1 relaxation sweeps on level k.
  - Perform γ coarse grid correction cycles on level $k-1$.
  - Correct the solution on level k using the results on level $k-1$.
  - Perform v_2 relaxation sweeps on level k.

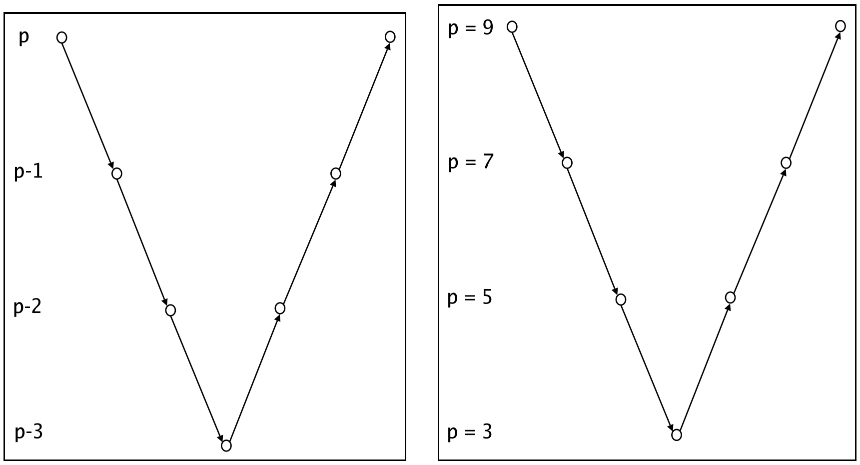

(a) $\triangle p = 1$ (b) $\triangle p = 2$

Figure 6.10: Four level V-cycles for p-multigrid

When $\gamma = 1$, the coarse grid correction cycle is referred to as the $V(\nu_1, \nu_2)$ cycle. In the case that $\gamma = 2$, it is called $W(\nu_1, \nu_2)$ cycle.

In the above two-level correction scheme, it is supposed that the order decreases by $\triangle p = p - q$ from the fine level to the coarse level. A general four level V-cycle is demonstrated for $\triangle p = 1$ in Figure 6.10 (a). However numerical tests indicate that p-multigrid is most robust and efficient for point contact EHL problems when $\triangle p = 2$. Therefore in this chapter, a four level V-cycle is employed, where $p = 9$ on the finest level, $p = 3$ on the coarsest level and $\triangle p = 2$ (see Figure 6.10 (b)). Note that the DG scheme is not stable for $p = 1$ [5,45].

6.5.2 Transfer Operators

Since the same spatial grid is used on all levels, the transfer operators between grids, restriction and prolongation, are local. Hence, the restriction and prolongation operators only need to be defined and stored for a reference element.

First we seek a prolongation operator through which we can represent the coarse level solution on the neighbouring fine level. That is:

$$u^p = I_q^p u^q \tag{6.48}$$

where u^p and u^q satisfy the following equation:

$$\sum_{j=1}^{n(p)} u_j^p N_j^p = \sum_{i=1}^{n(q)} u_i^q N_i^q. \tag{6.49}$$

Here N_j^p denotes the j^{th} basis function of order at most p on the reference element. Note that N_i^q can be written in terms of N_j^p:

$$N_i^q = \sum_{j=1}^{n(p)} \alpha_{i,j}^q N_j^p. \tag{6.50}$$

Substituting equation (6.50) into (6.49), we have:

$$\begin{aligned} \sum_{j=1}^{n(p)} u_j^p N_j^p &= \sum_{i=1}^{n(q)} u_i^q \sum_{j=1}^{n(p)} \alpha_{i,j} N_j^p, \\ \sum_{j=1}^{n(p)} I_q^p u_j^q N_j^p &= \sum_{j=1}^{n(p)} \sum_{i=1}^{n(q)} \alpha_{i,j} u_i^q N_j^p. \end{aligned} \tag{6.51}$$

Since a state representation is unique in the basis N_j^p, we have:

$$I_q^p = (\alpha^q)^T. \tag{6.52}$$

Note that equation (6.52) is for general case. When the hierarchical basis functions (see equation (6.6)) are used, it is easy to see that

$$\alpha_{i,j}^q = \begin{cases} 1 & \text{when } i = j \\ 0 & \text{otherwise} \end{cases}. \tag{6.53}$$

Hence I_q^p is the identity matrix with zero rows appended:

$$I_q^p = \begin{bmatrix} I_q \\ 0 \end{bmatrix}. \tag{6.54}$$

In order to transfer the residual to the next coarse level, a residual restriction operator is needed, for which

$$R^q = I_p^q R^p. \tag{6.55}$$

Let L represent the original system of partial differential equations and Ω denote the entire domain,

$$R_i^q = \int_\Omega (L) N_i^q \, \mathrm{d}\Omega \tag{6.56}$$

and

$$R_j^p = \int_\Omega (L) N_j^p \, \mathrm{d}\Omega. \tag{6.57}$$

Using equation (6.50) then, rewriting equation (6.56), we have

$$\begin{aligned} R_i^q &= \int_\Omega (L) N_i^q \, \mathrm{d}\Omega \\ &= \sum_{j=1}^{n(p)} \alpha_{i,j}^q \int_\Omega (L) N_j^p \, \mathrm{d}\Omega \\ &= \sum_{j=1}^{n(p)} \alpha_{i,j}^q R_j^p . \end{aligned} \tag{6.58}$$

The resulting residual restriction operator is:

$$I_p^q = \alpha^q . \tag{6.59}$$

When using the hierarchical basis, I_p^q is identity matrix with zero columns appended:

$$I_p^q = \left[\begin{array}{cc} I_q & 0 \end{array} \right] . \tag{6.60}$$

In order to evaluate the state restriction operator, the following equality is enforced, since it is impossible to represent a general p^{th} degree solution using basis functions of degree $q < p$:

$$\int_\Omega N_k^q \sum_i u_i^q N_i^q \, \mathrm{d}\Omega = \int_\Omega N_k^q \sum_j u_j^p N_j^p \, \mathrm{d}\Omega . \tag{6.61}$$

This can be rewritten as follows:

$$\sum_{i=1}^{n(q)} \mathscr{M}_{k,i}^q u_i^q = \sum_{j=0}^{n(p)} \mathscr{N}_{k,j}^q u_j^p , \tag{6.62}$$

where

$$\mathscr{M}_{k,i}^q = \int_\Omega N_k^q N_i^q \, \mathrm{d}\Omega \tag{6.63}$$

and

$$\mathscr{N}_{k,j}^q = \int_\Omega N_k^q N_j^p \, \mathrm{d}\Omega . \tag{6.64}$$

Thus,

$$u^q = (\mathscr{M}^q)^{-1} \mathscr{N}^q u^p \tag{6.65}$$

and

$$\tilde{I}_p^q = (\mathscr{M}^q)^{-1} \mathscr{N}^q . \tag{6.66}$$

Note that the above operators only need to be calculated over the reference element since the data transfer operations between levels are performed element-by-element throughout the entire domain. Since these three transfer operators do not depend on the structure of the grid , they only need to be calculated once even when using adaptive grids.

6.6 Adaptivity

Since the solutions of typical EHL problems exhibit sharp local features, such as pressure spikes and variations in the film thickness, some form of adaptivity is essential in order to obtain a robust and efficient solution method. In this section we describe an adaptive algorithm based upon local h-refinement and coarsening, where the polynomial degree on each element is kept fixed. Of course it would also be possible to adapt the polynomial degree on each element but this would significantly complicate the p-multigrid algorithm outlined in the previous section and so has not been considered at this stage. Furthermore, since the solution trial space is discontinuous over element interfaces, h-adaptivity is relatively easy to implement: unlike for C^0 finite elements which require continuity restrictions on element boundaries to be taken into account.

In this chapter, local h-refinement is used to improve the local accuracy of the solution where it is not accurate enough and local grid-coarsening is performed in smooth regions to reduce the number of degrees of freedom. In order to undertake h-adaptivity, the quality of the current solution needs to be evaluated: a generalization of the technique based on the high order components of the pressure (applied successfully in 1d in Chapters 4 and 5) is proposed.

6.6.1 Adaptive Strategy

In Chapter 5, highly accurate one-dimensional solutions were obtained using an h-adaptivity method based on the magnitude of the high-order components of the pressure solution on each element. In this chapter, we extend this approach to the two-dimensional problems considered here. For the *hierarchical* basis functions [58] used in this chapter, the high-order modes can be viewed as terms added to a lower order solution in order to improve its accuracy. To illustrate this we rewrite equation (6.5), for the solution P^e on a element e, as:

$$P^e(X) = \sum_{i=1}^{n(p^e-1)} u_i^e N_i^e(X) + \sum_{i=n(p^e-1)}^{n(p^e)} u_i^e N_i^e(X). \tag{6.67}$$

Here the second term contains only terms of the highest order, p^e whilst the first sum contains the terms of order at most $p^e - 1$. A simple error indicator is provided by con-

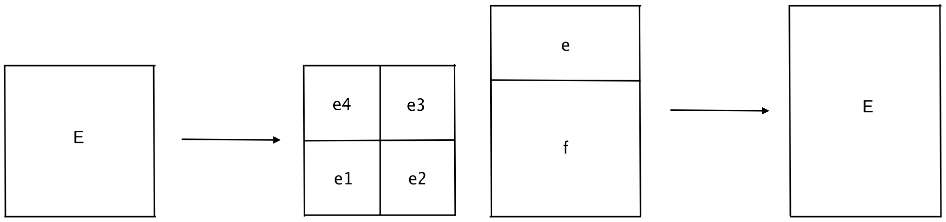

(a) Mesh refinement (b) Mesh coarsening

Figure 6.11: H-adaptivity in two dimensions

sidering

$$E^e = \left\| \sum_{i=n(p^e-1)}^{n(p^e)} u_i^e N_i^e(X) \right\|_2 = \sqrt{\frac{2}{h_x^e}\frac{2}{h_y^e}\int_{\Omega_e}\left(\sum_{i=n(p^e-1)}^{n(p^e)} u_i^e N_i^e(X)\right)^2 \mathrm{d}X}. \tag{6.68}$$

The use of this error indicator leads to the following rules for local mesh adaptivity.

1. Refine element e if $E^e > Tol_1$, where Tol_1 is a given tolerance, by splitting e into 4 equally sized smaller elements (see Figure 6.11 (a)).

2. Remove edge k, which has two neighbouring elements e and f, if $E^e < Tol_2$ and $E^f < Tol_2$, where Tol_2 is a smaller tolerance than Tol_1 (see Figure 6.11 (b)).

Here the quality of the numerical solution can be ensured by the h-adaptivity which forces all of the highest-order contributions of P smaller than Tol_1.

6.6.2 Data Transfer

Once the grid is adjusted, the current pressure on the original grid needs to be transferred onto the new grid so that the computation may be continued from the current estimate of the solution. The two-dimensional data transfer between the new grid and the old grid includes two cases: transferring the solution from one original element to four equally sized smaller elements, and transferring the solution from two neighbouring smaller original elements to one new larger element, which is generated by agglomerating these two elements. Thus, two local transfer operators, I_f^c and I_c^f, are required.

First we consider a transfer operator I_c^f to transfer solution from E to e_1, e_2, e_3 and e_4 (see Figure 6.11 (a)). This may be achieved through interpolation by enforcing

$$\int_{e_k} P^E(X)v\mathrm{d}X = \int_{e_k} P^{e_k}(X)v\,\mathrm{d}X,\ \forall v \in \left\{N_i^{e_k}(X),\ i = 1,2,\ldots,n(p^{e_k})\right\}, \tag{6.69}$$

which can be written as:

$$\begin{aligned}\int_{e_k}\left(\sum_{j=1}^{n(p^E)} u_j^E N_j^E(X)\right) v\,\mathrm{d}X &= \int_{e_k}\left(\sum_{j=1}^{n(p^{e_k})} u_j^{e_k} N_j^{e_k}(X)\right) v\,\mathrm{d}X, \\ \forall v &\in \left\{N_i^{e_k}(X),\ i=1,2,\ldots,n(p^{e_k})\right\},\end{aligned} \tag{6.70}$$

for $k=1,2,3,4$. This yields the matrix systems

$$u^{e_k} = (\mathscr{A}^{e_k})^{-1}\mathscr{B}^{e_k}u^E, \tag{6.71}$$

where

$$\mathscr{A}_{ij}^{e_k} = \int_{e_k} N_j^{e_k}(X)N_i^{e_k}(X)\,\mathrm{d}X = \sum_{k=1}^{n\times n} N_j^{e_k}(X_k)N_i^{e_k}(X_k)w_k, \tag{6.72}$$

$$\mathscr{B}_{ij}^{e_k} = \int_{e_k} N_j^{E}(X)N_i^{e_k}(X)\,\mathrm{d}X = \sum_{k=1}^{n\times n} N_j^{E}(X_k)N_i^{e_k}(X_k)w_k. \tag{6.73}$$

Thus

$$\left(I_c^f\right)^{e_k} = (\mathscr{A}^{e_k})^{-1}\mathscr{B}^{e_k}. \tag{6.74}$$

for $k=1,2,3,4$. Overall, we therefore have

$$I_c^f = \begin{bmatrix} (\mathscr{A}^{e_1})^{-1}\mathscr{B}^{e_1} \\ (\mathscr{A}^{e_2})^{-1}\mathscr{B}^{e_2} \\ (\mathscr{A}^{e_3})^{-1}\mathscr{B}^{e_3} \\ (\mathscr{A}^{e_4})^{-1}\mathscr{B}^{e_4} \end{bmatrix}. \tag{6.75}$$

Clearly the I_f^c operators cannot generally be interpolants however they may be defined by enforcing the following weak form

$$\int_E P^E(X)v\mathrm{d}X = \int_{e+f} P^{e+f}(X)v\,\mathrm{d}X,\ \forall v \in \left\{N_i^E(X),\ i=1,2,\ldots,n(p^E)\right\}. \tag{6.76}$$

Here $P^E(X) = \sum_{i=1}^{n(p^E)} u_i^E N_i^E(X)$ is the pressure in E and $P^{e+f}(X)$ is the pressure in $e+f$, where $P^{e+f} = P^e = \sum_{i=1}^{n(p^e)} u_i^e N_i^e(X)$ when $X \in e$ and $P^{e+f} = P^f = \sum_{i=1}^{n(p^f)} u_i^f N_i^f(X)$ when $X \in f$. Using $n \times n$ point two-dimensional Gaussian quadrature with weights w_k, equation (6.76) becomes

$$\sum_{k=1}^{n\times n}(P^E(X)v)_k w_k = \sum_{k=1}^{n\times n}(P^{e+f}(X)v)_k w_k,\ \forall v \in \left\{N_i^E(X),\ i=1,2,\ldots,n(p^E)\right\}. \tag{6.77}$$

The above equation expands to be

$$\begin{aligned}\sum_{k=1}^{n\times n}\left(\sum_{j}^{n(p^E)} u_j^E N_j^E(X_k) N_i^E(X_k)\right) w_k &= \sum_{X_k\in e}\left(\sum_{j}^{n(p^e)} u_j^e N_j^e(X_k) N_i^E(X_k)\right) w_k \\ &+ \sum_{X_k\in f}\left(\sum_{j}^{n(p^f)} u_j^f N_j^f(X_k) N_i^E(X_k)\right) w_k, \quad (6.78)\end{aligned}$$

for $i = 1,2,\ldots,n(p^E)$. In matrix form this may be expressed as

$$\mathscr{M} u^E = \mathscr{N}^e u^e + \mathscr{N}^f u^f \tag{6.79}$$

where

$$\begin{aligned}\mathscr{M}_{ij} &= \sum_{k=1}^{n\times n}\left(N_j^E(X_k) N_i^E(X_k)\right) w_k, && (6.80)\\ \mathscr{N}_{ij}^e &= \sum_{X_k\in e}\left(N_j^e(X_k) N_i^E(X_k)\right) w_k, && (6.81)\\ \mathscr{N}_{ij}^f &= \sum_{X_k\in f}\left(N_j^f(X_k) N_i^E(X_k)\right) w_k && (6.82)\end{aligned}$$

and

$$u^E = \left(u_1^E, u_2^E, \ldots, u_{n(p^E)}^E\right). \tag{6.83}$$

Therefore,

$$I_f^c = \left[\begin{array}{cc}\left(I_f^c\right)^e & \left(I_f^c\right)^f\end{array}\right] = \left[\begin{array}{cc}\mathscr{M}^{-1}\mathscr{N}^e & \mathscr{M}^{-1}\mathscr{N}^f\end{array}\right]. \tag{6.84}$$

6.7 Overall Solution Procedure

Having introduced all of the components of the solution algorithm this section briefly describes how the p-multigrid may be combined with h-adaptivity to provide the following overall solution procedure.

1 Give an initial grid and ensure that this grid covers the pressurised domain. That is to say, the left boundary of the given grid is required to be far away from the contact centre and the actual cavitation position should be inside the given grid. Provide Tol_1 and Tol_2 for h-adaptivity.

2 Initialize the pressure on the given grid (For example, the Hertzian dry contact pressure profile [60] is used in this chapter). Give an initial guess for H_{00} (zero is

usually used).

3 Calculate the kernels K_i^e (see equation (6.15)) at all quadrature points and on element boundaries, and calculate the kernels G_i^e (see equation (6.27)).

4 Perform 1 or 2 V-cycles on the current grid to update the solution. On the initial grid which is usually coarse, we do more V-cycles to make the solution almost converge. Note that H_{00} is only updated on the finest level.

5 Check if the grid needs to be adjusted according to Tol_1 and Tol_2.

6 Stop if $E^e > Tol_1$ for each element e and the L_2-norm of the numerical residual is less than a given tolerance (10^{-10} say).

7 Adjust the grid if needed and transfer the current pressure profile from the old grid onto the new grid. Calculate the kernels K_i^e and G_i^e related to any new element. Go to 4.

6.8 Numerical Results

In this thesis, four loaded cases ((a) $W = 0.2 \times 10^{-7}$, $U = 0.1 \times 10^{-11}$ and $G = 5000$; (b) $W = 0.5 \times 10^{-7}$, $U = 0.2 \times 10^{-11}$ and $G = 5000$; (c) $W = 0.6 \times 10^{-7}$, $U = 0.2 \times 10^{-11}$ and $G = 5000$; (d) $W = 0.7 \times 10^{-7}$, $U = 0.3 \times 10^{-11}$ and $G = 5000$) are solved using the high-order DG method. For each case, the same initial guess is used: the piecewise bilinear interpolant of the Hertzian dry contact pressure profile,

$$p(x,y) = \begin{cases} \sqrt{1-x^2-y^2} & \text{if } |x^2+y^2| < 1 \\ 0 & \text{otherwise} \end{cases}. \tag{6.85}$$

This initial guess is shown in Figure 6.13 for a typical initial grid (see Figure 6.12). Note that the initial pressure profile is not smooth, and discontinuities over the element boundaries can be observed. Of course, a smoother initial guess could be more suitable but this choice of initial data demonstrates that a good initial guess is not generally required.

In these results values of $Tol_1 = 0.001$ and $Tol_2 = 0.00005$ are used for the h-adaptivity. On the initial grid, 10 V-cycles are performed to resolve an almost converged solution prior to any h-adaptivity. After the first h-adaptivity, the quality of the current solution is checked after every 2 V-cycles before repeated h-adaptivity is applied until the quality of the solution is satisfactory ($E^e < Tol_1$ for each element e) and it has fully converged (the L_2-norm of the numerical residual is less than 10^{-10}).

Tol_1	Number of Elements	Peak Pressure	Peak Position
0.025	26	1.33297	(0.57609,0)
0.005	34	1.32411	(0.57746,0)
0.001	48	1.32259	(0.57982,0)
0.0002	121	1.31972	(0.57768,0)

Table 6.1: Comparison of Pressure Peak Position and Peak Pressure

The fully converged pressure profiles for each of these cases are displayed in Figures 6.15, 6.18, 6.21 and 6.24 along with the final mesh generated (recall $p = 9$ on each element). In each case a pressure profile is obtained with 48, 60, 126, 246 elements respectively (48×57, 60×57, 126×57 and 246×57 degrees of freedom respectively). These are all symmetric along $y = 0$ as expected. The pressure ridge which characterizes point contact EHL problems is accurately captured in each case on the final grids (see Figure 6.14, 6.17, 6.20 and 6.23). Note that to obtain equivalent results using standard finite difference methods would require very large numbers of degrees of freedom [25, 26, 60] (for example, up to 16385×16385 degrees of freedom were used in [26]).

For all four of these cases, P increases smoothly from the inflow boundary ($x = -4.0$) to the contact centre ($x = 0, y = 0$) along the central line $y = 0$. The pressure drops a bit and then goes up steeply to the top of the pressure ridge. In the short distance between the top of the pressure ridge and the cavitation boundary, where P becomes zero, the pressure decreases rapidly. It should be noted however that the shapes of these three pressure ridges are significantly different. In Figure 6.15, the maximum pressure is located on the central line $y = 0$ and P decreases in both the x and y directions from the top of the pressure ridge. In Figures 6.18, 6.21 and 6.24, the maximum pressure is not on the central line (and so, due to symmetry, there are in fact two maxima). In Figure 6.18 for example, the pressure at the top of the ridge increases significantly from the central line when moving along the y and $-y$ directions, before decreasing rapidly to zero.

In order to demonstrate that $Tol_1 = 0.001$ is small enough to provide a sufficiently accurate solution. Case (a) is also solved using three other tolerances, $Tol_1 = 0.025$, $Tol_1 = 0.005$ and $Tol_1 = 0.0002$ respectively. Table 6.1 shows a detailed comparison of the peak pressure and the peak pressure location when using different Tol_1. The difference in these results are very small: especially when Tol_1 is reduced from 0.001 to 0.0002.

In Chapter 4, numerical results have been provided to show that the penalty method does not give an especially accurate cavitation position in the 1d case unless local refinement is performed in this region. In this chapter, an additional h-refinement also is performed for the case (a) ($W = 0.2 \times 10^{-7}$, $U = 0.1 \times 10^{-11}$ and $G = 5000$) around the cavitation region in order to check the accuracy of the penalty method. Let $\{e_{cavi}\}$ denote

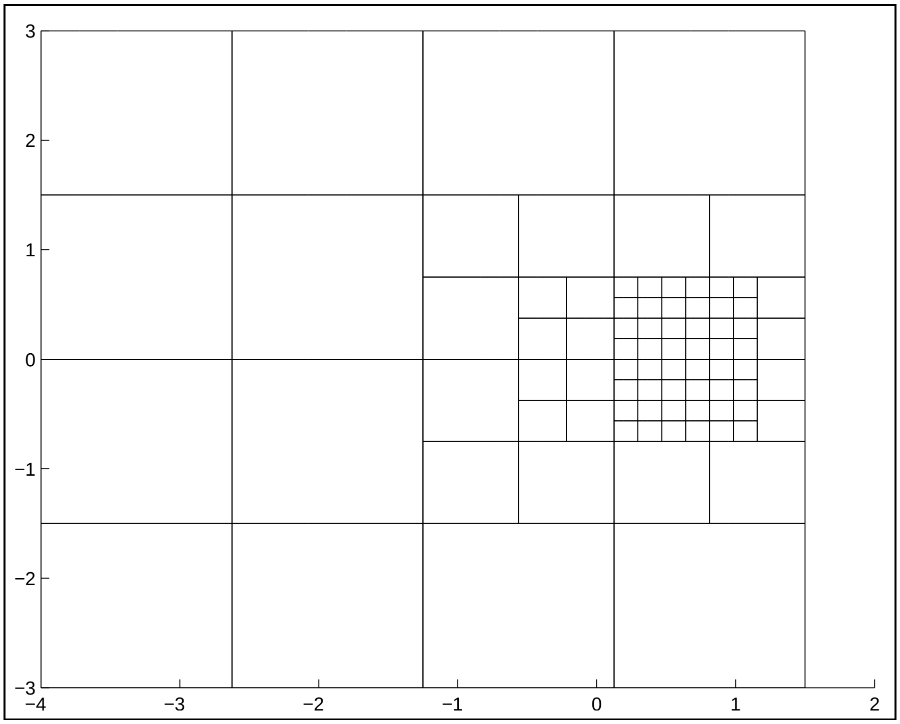

Figure 6.12: Initial grid

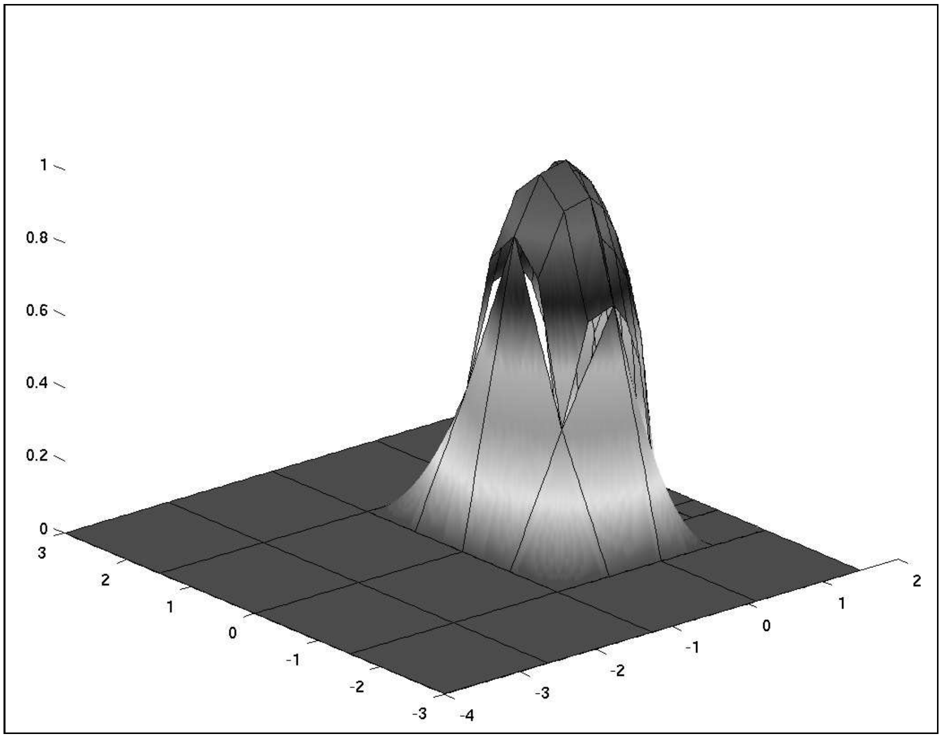

Figure 6.13: Initial pressure profile

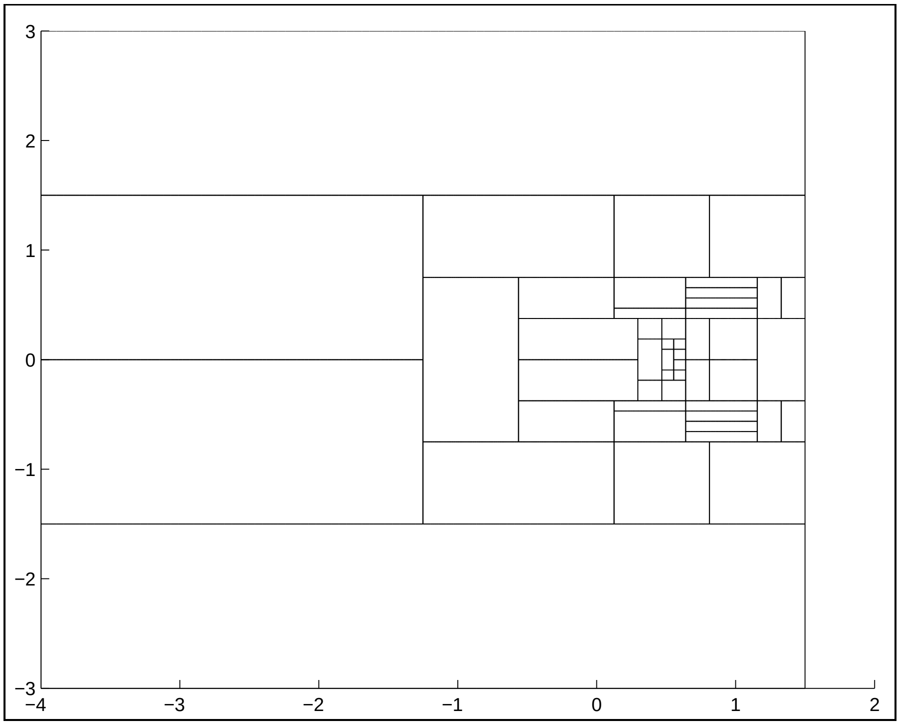

Figure 6.14: Final grid (a): $W = 0.2 \times 10^{-7}$, $U = 0.1 \times 10^{-11}$ and $G = 5000$

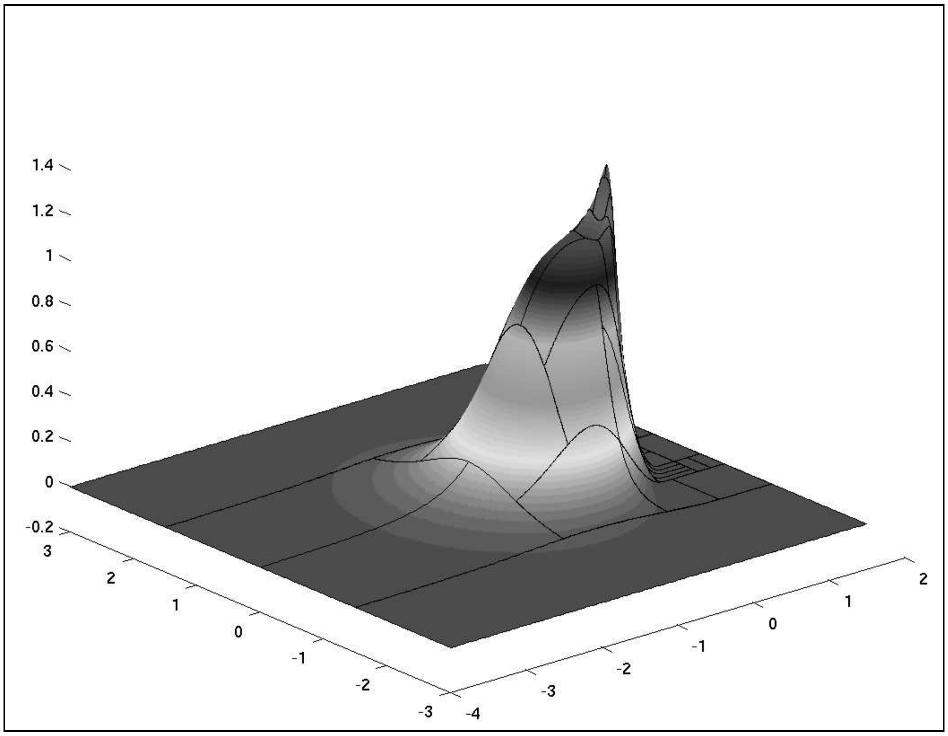

Figure 6.15: Converged pressure profile (a): $W = 0.2 \times 10^{-7}$, $U = 0.1 \times 10^{-11}$ and $G = 5000$

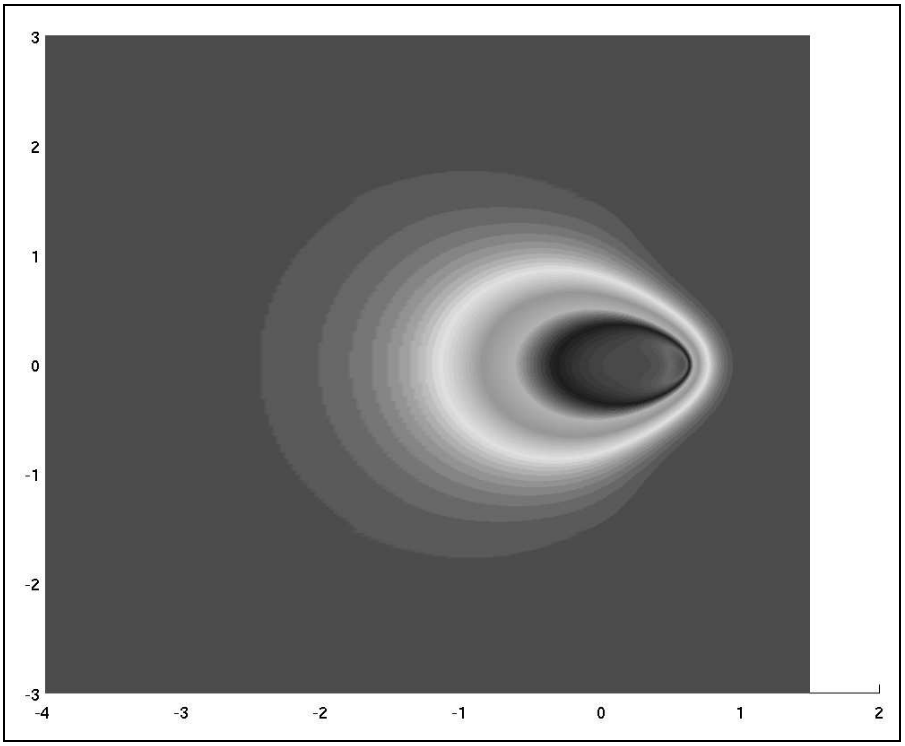

Figure 6.16: Converged pressure profile (a): $W = 0.2 \times 10^{-7}$, $U = 0.1 \times 10^{-11}$ and $G = 5000$

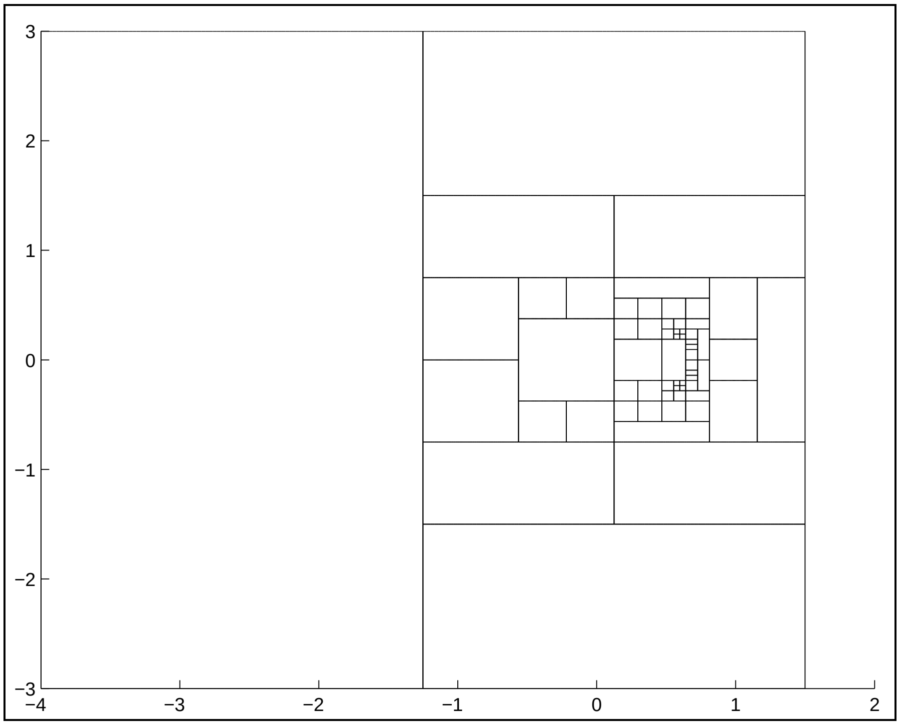

Figure 6.17: Final grid (b): $W = 0.5 \times 10^{-7}$, $U = 0.2 \times 10^{-11}$ and $G = 5000$

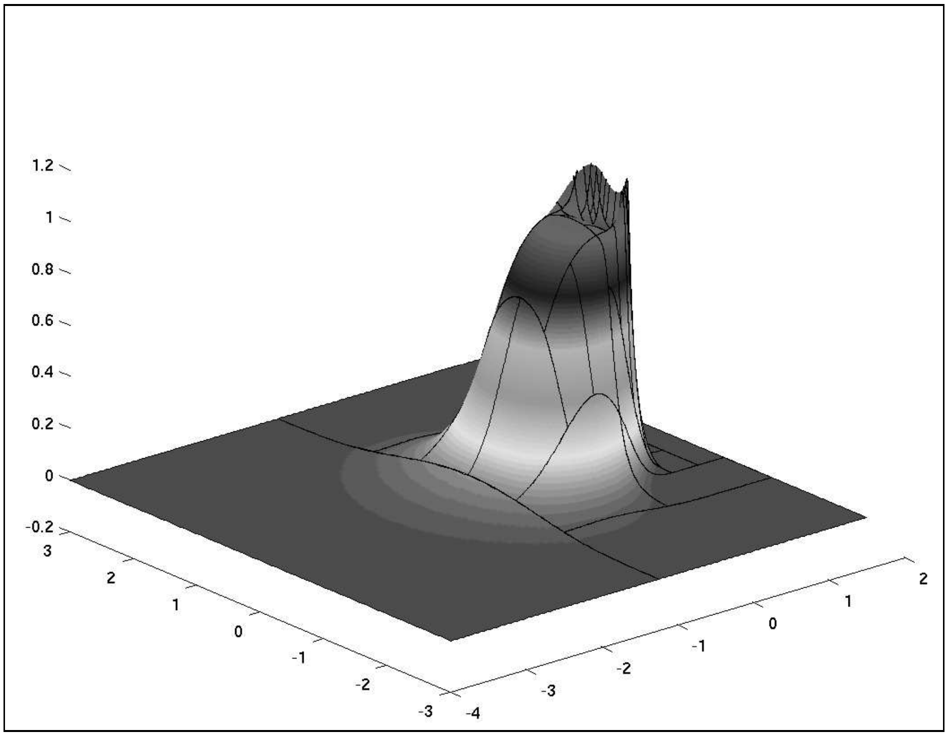

Figure 6.18: Converged pressure profile (b): $W = 0.5 \times 10^{-7}$, $U = 0.2 \times 10^{-11}$ and $G = 5000$

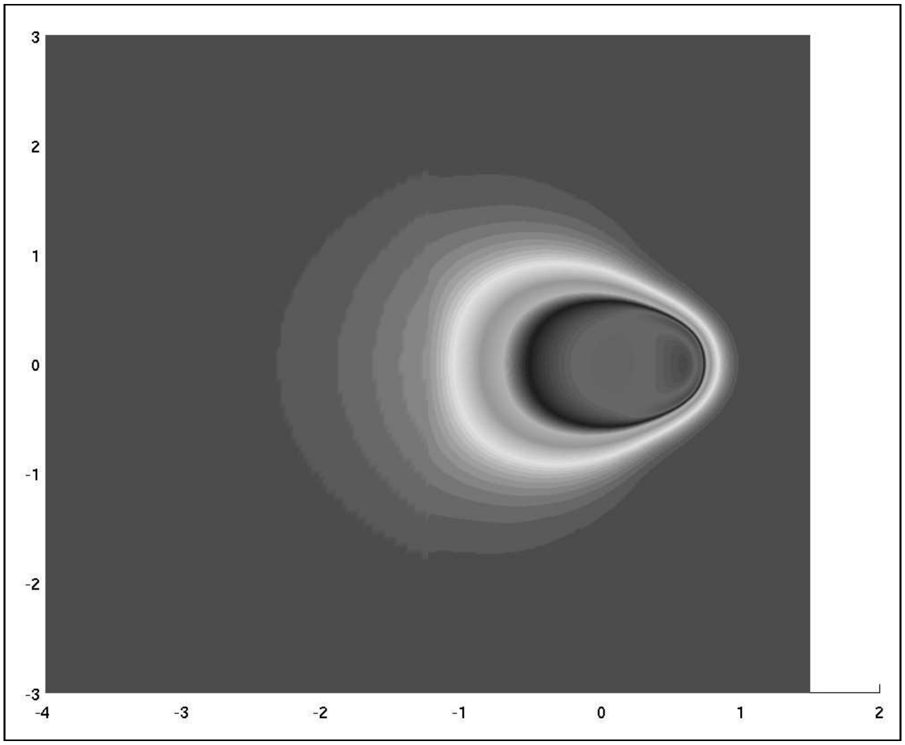

Figure 6.19: Converged pressure profile (b): $W = 0.5 \times 10^{-7}$, $U = 0.2 \times 10^{-11}$ and $G = 5000$

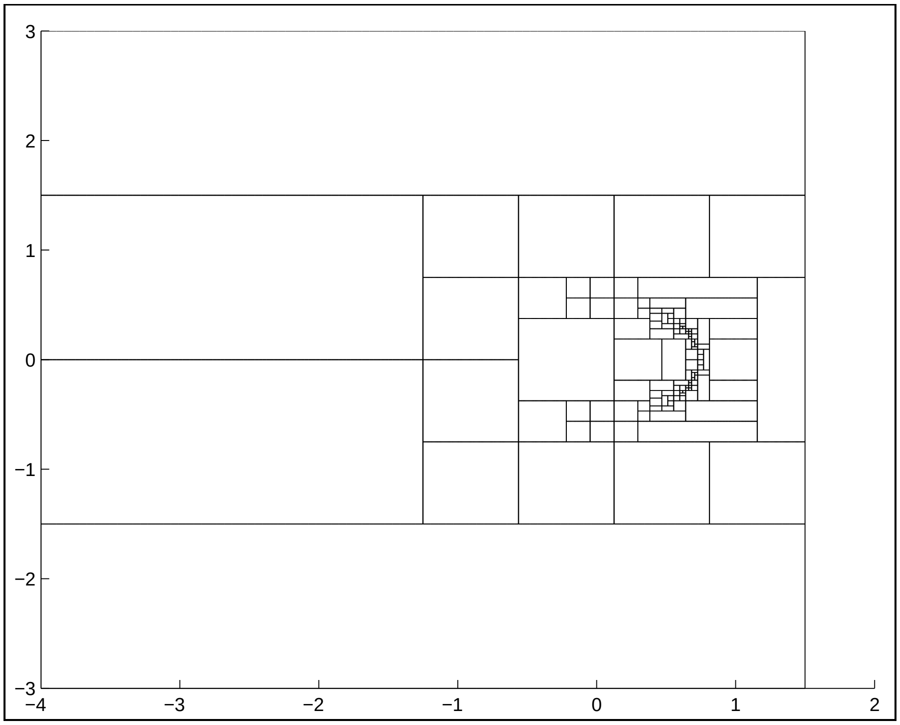

Figure 6.20: Final grid (c): $W = 0.6 \times 10^{-7}$, $U = 0.2 \times 10^{-11}$ and $G = 5000$

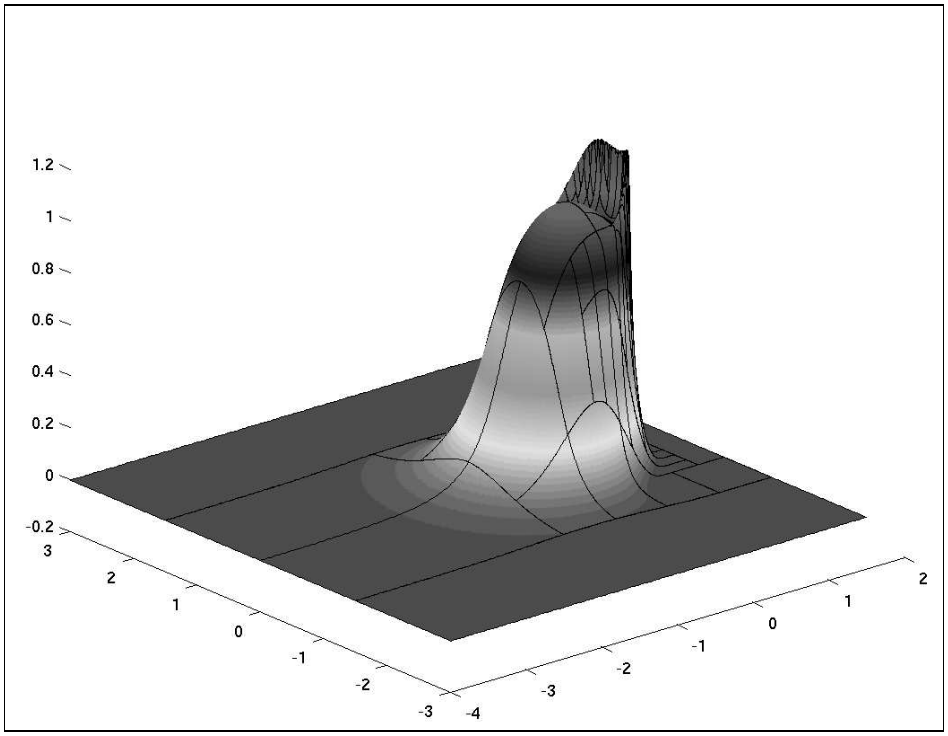

Figure 6.21: Converged pressure profile (c): $W = 0.6 \times 10^{-7}$, $U = 0.2 \times 10^{-11}$ and $G = 5000$

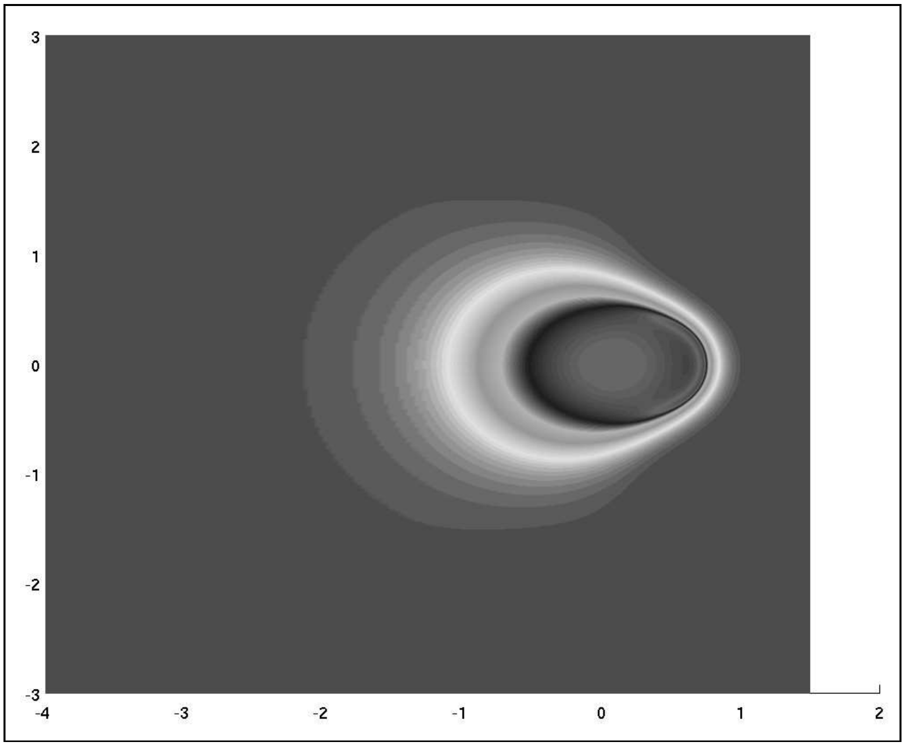

Figure 6.22: Converged pressure profile (c): $W = 0.6 \times 10^{-7}$, $U = 0.2 \times 10^{-11}$ and $G = 5000$

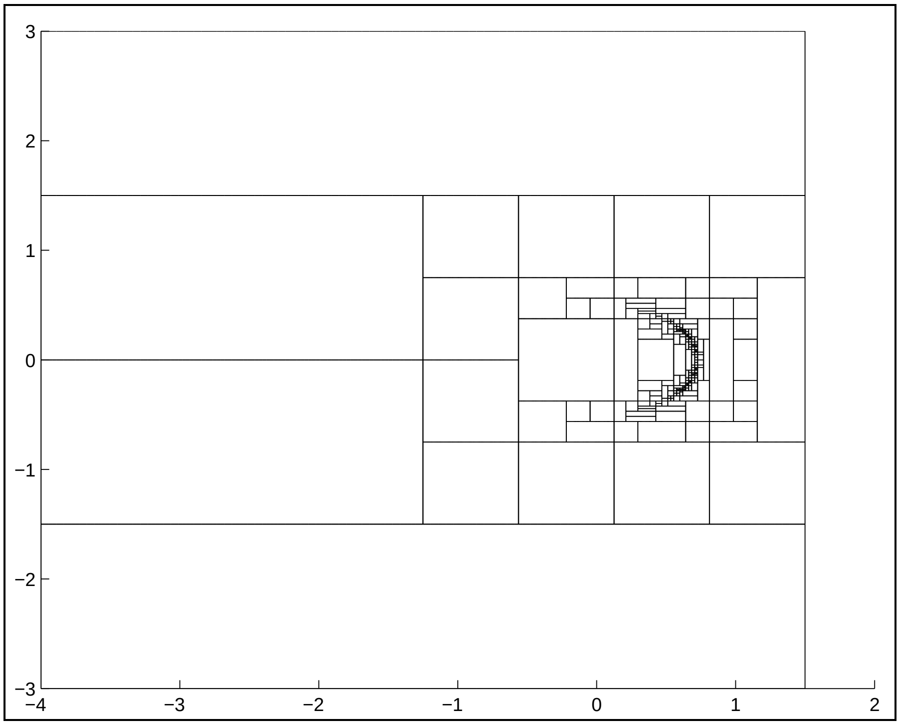

Figure 6.23: Final grid (d): $W = 0.7 \times 10^{-7}$, $U = 0.3 \times 10^{-11}$ and $G = 5000$

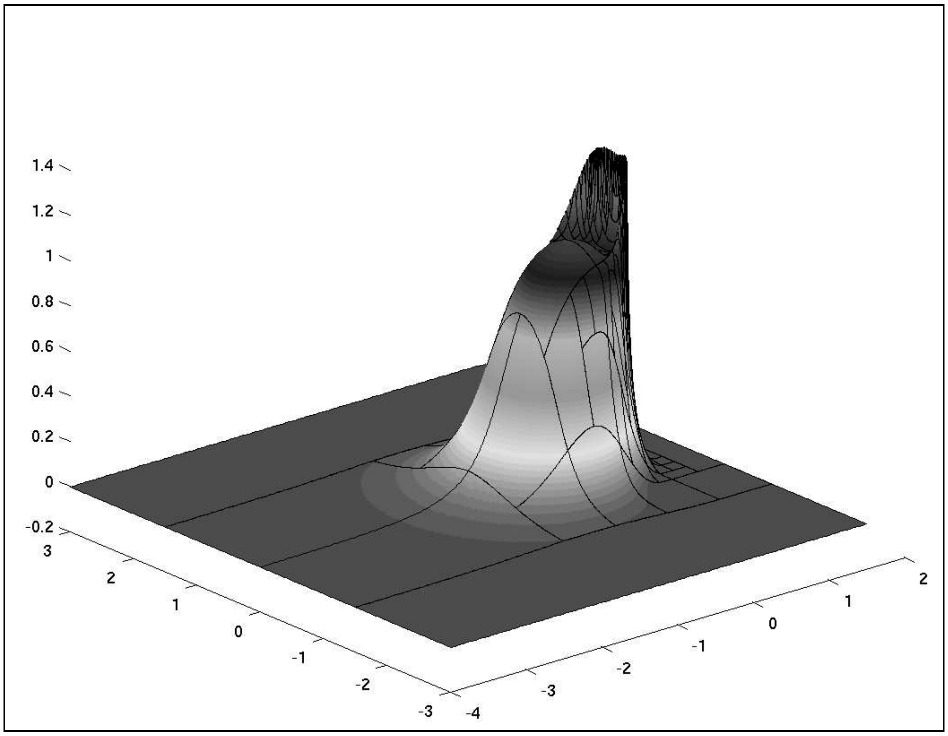

Figure 6.24: Converged pressure profile (d): $W = 0.7 \times 10^{-7}$, $U = 0.3 \times 10^{-11}$ and $G = 5000$

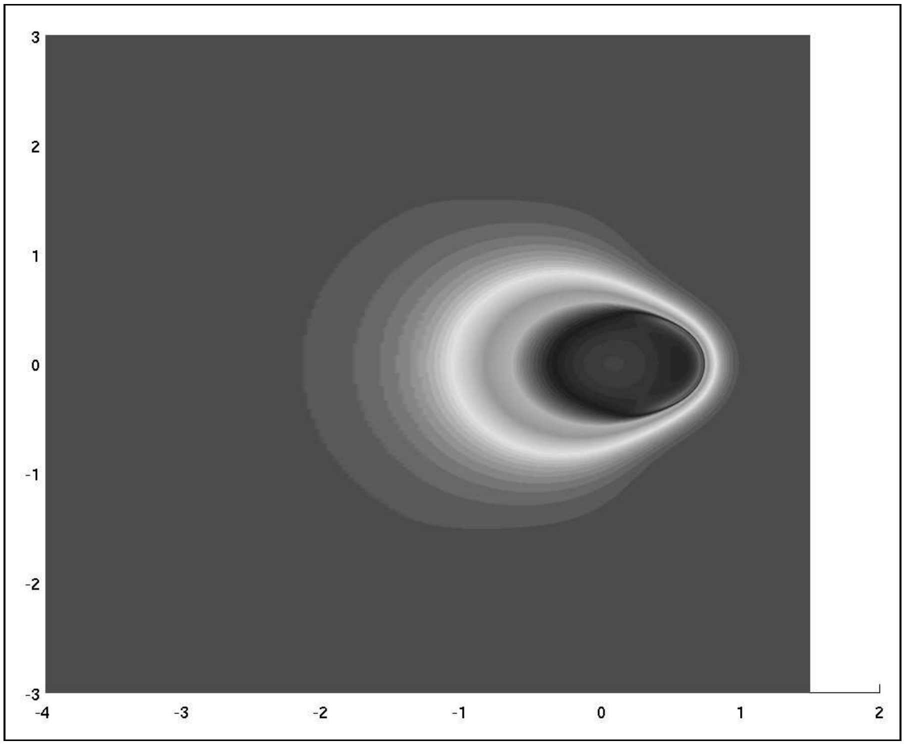

Figure 6.25: Converged pressure profile (d): $W = 0.7 \times 10^{-7}$, $U = 0.3 \times 10^{-11}$ and $G = 5000$

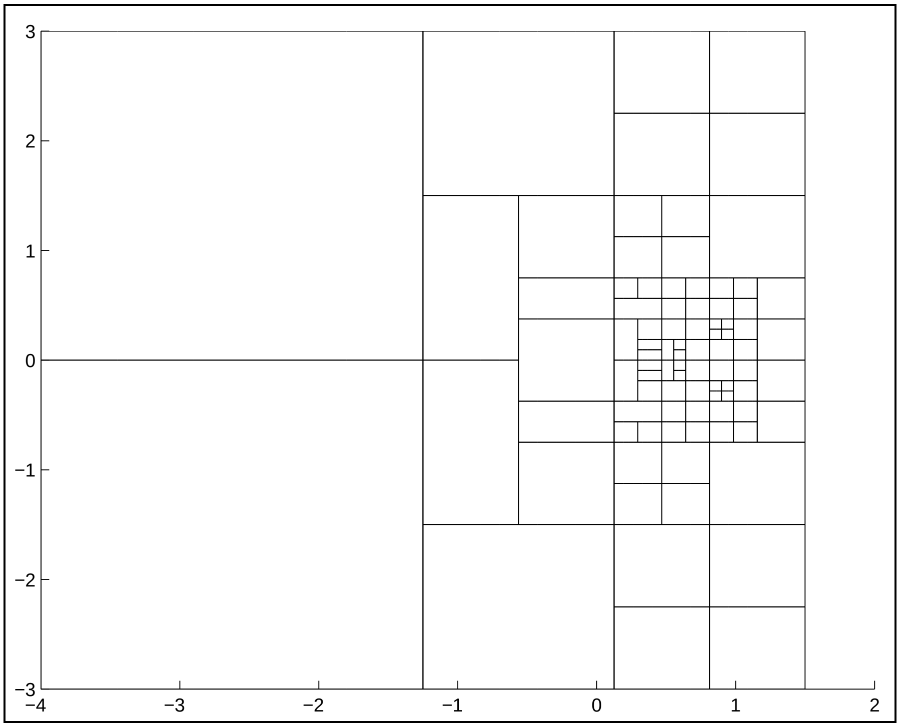

Figure 6.26: Final grid when $Tol_{penalty} = 0.05$ (a): $W = 0.2 \times 10^{-7}$, $U = 0.1 \times 10^{-11}$ and $G = 5000$

Method	Number of Elements	Peak Pressure	Peak Position
Regular penalty method	48	1.32259	(0.57982,0)
$Tol_{penalty} = 0.05$	89	1.31753	(0.57810,0)
$Tol_{penalty} = 0.001$	167	1.31733	(0.57789,0)

Table 6.2: Comparison of Pressure Peak Position and Peak Pressure

all the elements inside which cavitation occurs. This additional h-refinement is performed during the computation until all the pressures on the quadrature points in $e \in \{e_{cavi}\}$ have a maximum pressure magnitude of less than a given tolerance $Tol_{penalty}$. $Tol_{penalty} = 0.05$ and $Tol_{penalty} = 0.001$ are used for this test. The final adaptive grids are shown in Figure 6.26 and 6.27 respectively. Compared to Figure 6.14, the grid structure around the cavitation boundary is significantly different in Figures 6.26 and 6.27 due to the additional h-refinement. Table 6.2 displays the number of elements, the peak pressures and the peak positions when using the regular penalty method and the refined penalty methods. Although the cavitation region is further refined to improve the accuracy of the cavitation boundary, only very small differences can be observed for the peak pressure and the peak position in Table 6.2, which indicates that the regular penalty method is indeed sufficiently accurate. Of course if the cavitation boundary is required to great accuracy this can be resolved through further refining the cavitation region as needed.

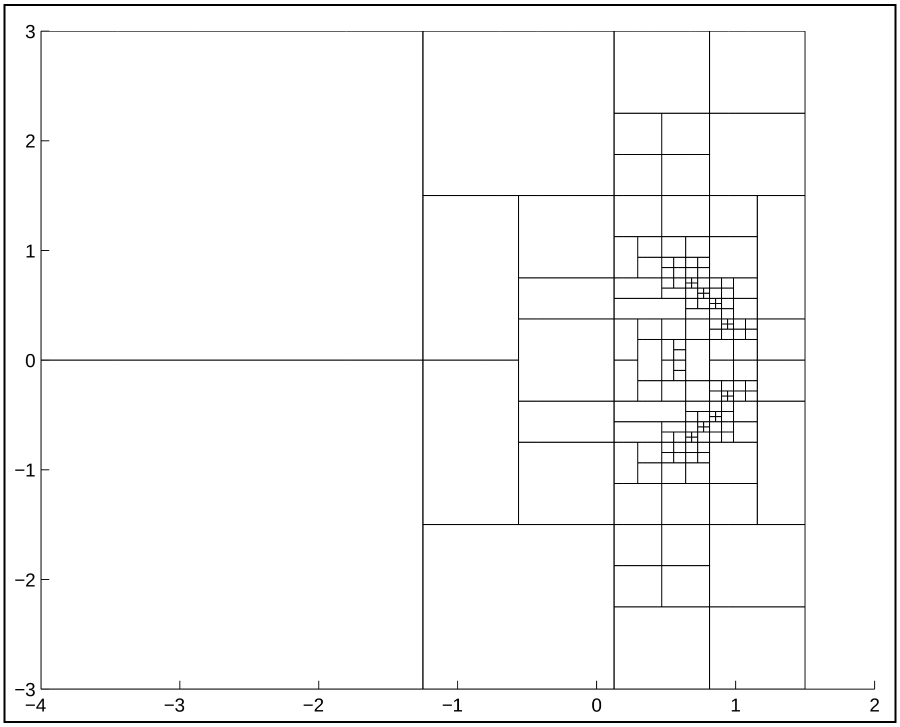

Figure 6.27: Final grid when $Tol_{penalty} = 0.001$ (a): $W = 0.2 \times 10^{-7}$, $U = 0.1 \times 10^{-11}$ and $G = 5000$

6.9 Conclusion

In this chapter, a high-order finite element scheme, based upon the Discontinuous Galerkin method, has been successfully applied to two-dimensional EHL point contact problems. The relaxation method developed here provides a robust smoother for the p-multigrid solver in both the contact and the non-contact regions. In order to capture all details of the EHL solutions, particularly the pressure ridge, an h-adaptivity method has been developed based on the significance of the high-order contributions to the pressure. The penalty method handles the cavitation condition easily and does not affect the accuracy significantly, although it can not provide the exact cavitation position unless further h-refinement is imposed in this region.

Numerical results show that highly accurate solutions can be obtained using a small number of degrees of freedom for a wide range of loaded cases. In particular, the typical pressure ridges that occur in these problems can be precisely resolved.

The cost of the method, in terms of both memory and computation, is dominated by the evaluation of the film thickness, (6.14) and (6.15). This is made tractable due to the precomputation of the kernel functions (6.15) at quadrature points, however the computation of these kernels is still relatively expensive compared to the overall solution time.

For example, for the case (c) it costs 75842 seconds to obtain the fully converged solution and 61546 seconds are spent on the calculation of these kernels. Hence the proposed technique would still benefit from further research work to improve the efficiency of the film thickness calculations. Additional efficiency benefits may be obtained by successfully parallelizing this method, since the high order DG is well suited to parallel implementation [10], and the computation of each of the kernels is independent from all others. It would also be interesting to consider the solution of transient point contact problems, involving variable loads or roughness in the contacting elements. In this chapter, only h-adaptivity is implemented since p-multigrid is used. P-adaptivity and hp-adaptivity could also be applicable. But p-multigrid would have to be "adaptive" and the interpolation between grids would be more complex. An advantage is that the kernels do not need to be updated after p-adaptivity when the hierarchical basis functions are used.

Chapter 7

Conclusion and Future Work

7.1 Conclusion

Elastohydrodynamic Lubrication problems arise when modelling the thin lubricating film between contacts which are under sufficiently high pressure that the elastic deformation of the contacting elements cannot be neglected. Numerical results should satisfy the three governing equations of EHL problems: the Reynolds equation, the film thickness equation and the force balance equation. EHL problems have the following challenges for numerical simulation:

1. The Reynolds equation, which is a second order partial differential equation that is derived via the thin-film approximation from the Navier-Stokes equation, is highly nonlinear.

2. The Reynolds equation may be either convection- or diffusion-dominated in different regions of the domain. When it is convection-dominated, stabilization techniques (for example, upwinding) are required for discretization.

3. EHL problems feature a free boundary, which models where cavitation occurs, and this should be automatically captured as part of the solution process. That is to say, the Reynolds equation is only valid in the pressurised region.

4. In many cases, particularly in highly loaded cases, the solutions of EHL problems are characterized by a very sharp pressure spike or ridge, which can be difficult to

capture accurately.

5. The film thickness equation contains a global integral. This means that the film thickness at any position depends upon all the pressures over the entire computational domain.

6. In order to accelerate the computation of the film thickness, Multilevel Multi-Integration (MLMI) is usually employed. However, MLMI is only applicable on uniform meshes, which makes it difficult to use adaptive meshes to capture some solution details (for example, the pressure spike) and to reduce the complexity.

Over the last few decades, many numerical methods have been developed to solve EHL problems. However, all of these methods use low order discretizations (for example, Finite Difference (FD)), which leads to the fact that it is difficult for some details of the solution (for example, the pressure spike) to be captured accurately unless huge numbers of degrees of freedom are used [27]. Finite element methods have also been used to solve EHL problems [1, 34, 35, 44, 46, 55, 59, 64]. However, they are only stable for incompressible lubricants.

In this thesis, a highly accurate method, based on high-order Discontinuous Galerkin (DG) methods, is introduced to solve isothermal elastohydrodynamic lubrication problems. This method has the following features:

1. The Reynolds equation is discretized using high-order DG, which provides highly accurate solutions.

2. The upwinding for the convection term of the Reynolds equation is easy to implement when using high-order DG, which provides a stable discretization over the entire computational domain whether it is convection-dominated or diffusion-dominated.

3. The high-order DG used is very suitable for h-adaptivity, which can reduce the computational complexity significantly compared to the low-order method (FD say). Hence, all solution details can be captured accurately at a lower expense on adaptive grids.

4. The free boundary condition is handled using the penalty method [64], which does not affect the accuracy significantly though it does not provide the exact cavitation position unless additional local mesh refinement is used.

5. The relaxation method introduced to solve the discrete nonlinear system is sufficiently stable in both the contact and the non-contact regions, even when no multilevel technique is used. This is because the film thickness-pressure relationship is fully considered in the iterative update procedure.

6. In the 2d case, the application of p-multigrid accelerates the convergence and makes the solution procedure more robust.

7.2 Future Work

In this thesis, highly accurate numerical solutions of EHL problems have been obtained using the high-order DG method in both 1d and 2d cases. However, further research about this new numerical approach still needs to be done in the future:

1. Although the introduction of the kernels (see equation (4.15) and (6.15)) provides a convenient way to compute the film thickness, the computation of these kernels is still relatively expensive compared to the overall solution time. Hence the proposed technique would still benefit from further research work to improve the efficiency of the film thickness calculations.

2. DG methods are well suited to parallel implementation. Furthermore, the computation of each kernel for film thickness is independent of all others. Hence we could benefit a lot from parallel computation to improve the solution efficiency, particularly for point contact problems.

3. Once the solution process is sufficiently efficient, it would be possible to numerically simulate transient point contact problems.

4. In this thesis, low-order temporal discretization is employed for line contact transient problems. Some higher-order schemes (for example, some multi-step time-stepping methods) should be considered in the future. Furthermore, it would also be worthwhile to consider using high-order DG in both time and space.

5. Adaptivity in time should also be considered to improve the efficiency. Error estimates can be used to adjust the time step and the order of the time discretization locally.

6. Our spatial adaptivity strategy is based on the magnitude of the discontinuities over element boundaries or the contribution of the high-order components. These are

both easy to implement and it has been shown that they can provide an appropriately spaced grid to capture every detail of the solution. However, a better adaptivity strategy may be based on some more formal or rigorous error estimates [10].

7. In this thesis, only h-adaptivity is implemented. However, DG is also well suited to p-adaptivity and hp-adaptivity. But p-multigrid would need to be "adaptive" and some criteria are required for deciding whether to refine or coarsen in h or p.

8. In this thesis for both line contact and point contact problems, only the isothermal case has been solved. It would be interesting to see if we can benefit from this new approach in thermal cases too.

Bibliography

[1] M. Arenaz, R. Doallo, J. Tourino, and C. Vazquez. Efficient parallel numerical solver for the elastohydrodynamic Reynolds-Hertz problem. *Parallel. Comput.*, 27(13):pp1743–1765, 2001.

[2] C. Barus. Isothermals , isopiestics and isometrics relative to viscosity. *AM J. Sci.*, 45:pp87–96, 1893.

[3] F. Bassi and S. Rebay. A high-order accurate discontinuous finite element method for the numerical solution of the compressible Navier-Stokes equations. *J. Comput. Phys.*, 131(2):pp267–279, 1997.

[4] P. Bastian and V. Reichenberger. Multigrid for higher order discontinuous Galerkin finite elements applied to groundwater flow. Technical report, 2000-37, SFB 359, 2000.

[5] C.E. Baumann and J.T. Oden. A discontinuous hp finite element method for convection-diffusion problems. *Comput. Method. App. M.*, 175(3):pp311–341, 1999.

[6] M. Berzins and R.M. Furzeland. An adaptive theta method for the solution of stiff and nonstiff differential equations. *Appl. Numer. Math.*, 9(1):pp1–9, 1992.

[7] A. Brandt and A.A. Lubrecht. Multilevel matrix multiplication and fast solution of integral equations. *J. Comput. Phys.*, 90:pp348–370, 1990.

[8] W.L. Briggs. *A Multigrid Tutorial, Second Edition*. SIAM, New York, 2000.

[9] L. Chang, T.F. Conry, and C. Cusano. An efficient robust multi-level computational algorithm for elastohydrodynamic lubrication. *J. Tribol-T. ASME*, 111:pp193–199, 1989.

[10] B. Cockburn, G.E. Karniadakis, and C.W. Shu. *Discontinuous Galerkin Methods: Theory, Computation and Applications*. Springer, Berlin, 1999.

[11] B. Cockburn and C.W. Shu. TVB Runge-Kutta local projection discontinuous Galerkin finite element method for scalar conservation laws 2: General framework. *Math. Comput.*, 52:pp411–435, 1989.

[12] B. Cockburn and C.W. Shu. The Runge-Kutta local projection P^1-discontinuous Galerkin method for scalar conservation laws. *RAIRO-Math. Model. Num.*, 25:pp337–361, 1991.

[13] B. Cockburn and C.W. Shu. The local discontinuous Galerkin method for time-dependent convection-diffusion systems. *SIAM J. Numer. Anal.*, 35(6):pp2440–2463, 1998.

[14] B. Cockburn and C.W. Shu. Runge-Kutta discontinuous Galerkin methods for convection-dominated problems. *J. Sci. Comput.*, 16:pp173–261, 2001.

[15] D. Dowson and G.R. Higginson. A numerical solution to the elasto-hydrodynamic problem. *J. Mech. Eng. Sci.*, 1(1):pp6–15, 1959.

[16] D. Dowson and G.R. Higginson. *Elasto-Hydrodynamic Lubrication, The Fundamentals of Roller and Gear Lubrication*. Pergamon Press, Oxford, Great Britain, 1966.

[17] C.D. Elcoate, H.P. Evans, and T.G. Hughes. On the coupling of the elastohydrodynamic problem. In *P. I. Mech. Eng. C-J. Mec.*, volume 212, pages pp307–318, 1998.

[18] C.D. Elcoate, H.P. Evans, T.G. Hughes, and R.W. Snidle. Transient elastohydrodynamic analysis of rough surfaces using a novel coupled differential deflection method. *P. I. Mech. Eng. J-J. Eng.*, 215(4):pp319–337, 2001.

[19] A.M. Ertel. Hydrodynamic lubrication based on new principles. *Akad. Nauk SSSR Prikladnaya Matematica i Mekhanika*, 3(2):pp41–52, 1939.

[20] E. Evans. *Practical Numerical Integration*. Wiley, 1993.

[21] H.P. Evans and T.G. Hughes. Evaluation of deflection in semi-infinite bodies by a differential method. In *P. I. Mech. Eng. C-J. Mec.*, volume 214, pages pp563–584, 2000.

[22] H.P. Evans and R.W. Snidle. Inverse solution of Reynolds equation of lubrication under point-contact elastohydrodynamic conditions. *J. Tribol-T. ASME*, 103:pp539–546, 1981.

[23] H.P. Evans and R.W. Snidle. The elastohydrodynamic lubrication of point contacts at heavy loads. In *P. Roy. Soc. Lond. A. Mat.*, volume 382, pages pp183–199, 1982.

[24] K.J. Fidkowski and D.L. Darmofal. Development of a higher-order solver for aerodynamic applications. In *42nd AIAA Aerospace Sciences Meeting and Exhibit, AIAA Paper 2004-0436*, 2004.

[25] C.E. Goodyer. *Adaptive Numerical Methods for Elastohydrodynamic Lubrication*. PhD thesis, University of Leeds, Leeds, UK, 2001.

[26] C.E. Goodyer and M. Berzins. Parallelization and scalability issues of a multilevel elastohydrodynamic lubrication solver. *Concurrency and Computation: Practice and Experience*, in press.

[27] C.E. Goodyer, R. Fairlie, D.E. Hart, M. Berzins, and L.E. Scales. Calculation of friction in steady-state and transient EHL simulations. In A. Lubrecht and G. Dalmaz, editors, *Transient Processes in Tribology: Proceedings of the 30th Leeds-Lyon Symposium on Tribology, Elsevier*, 2004.

[28] A.N. Grubin and I.E. Vinogradova. *Investigation of the Contact of Machine Components*. Book No 30, DSIR Translation No 337, Central Scientific Research Institute for Technology and Mechanical Engineering (Moscow), 1949.

[29] B.J. Hamrock and D. Dowson. Isothermal elastohydrodynamic lubrication of point contacts, Part 1-theoretical formulation. *J. Tribol-T. ASME*, 98:pp223–229, 1976.

[30] B.J. Hamrock and D. Dowson. Isothermal elastohydrodynamic lubrication of point contacts, Part 3-fully flooded results. *J. Tribol-T. ASME*, 99:pp264–276, 1977.

[31] B.J. Hamrock and B.O. Jacobson. Elastohydrodynamic lubrication of line contacts. *ASLE Trans.*, 27(4):pp275–287, 1984.

[32] D.E. Hart, C.E. Goodyer, M. Berzins, P.K. Jimack, and L.E. Scales. Ajoint error estimation for EHL-like models. *Int. J. Numer. Meth. Fl.*, 47:pp1069–1075, 2005.

[33] L. Houpert and B.J. Hamrock. A fast approach for calculating film thickness and pressure in elastohydrodynamically lubricated contacts at high loads. *J. Tribol-T. ASME*, 108:pp411–420, 1986.

[34] HS.S. Hsiao, B.J. Hamrock, and J.H. Tripp. Finite element system approach to EHL of elliptical contacts: Part 1 - isothermal circular non-Newtonian formulation. *J. Tribol-T. ASME*, 120(4):pp695–704, 1998.

[35] HS.S. Hsiao, B.J. Hamrock, and J.H. Tripp. Finite element system approach to EHL of elliptical contacts: Part 2 - isothermal results and performance formulas. *J. Tribol-T. ASME*, 121(4):pp711–720, 1999.

[36] T.G. Hughes, C.D. Elcoate, and H.P. Evans. A novel method for integrating first and second order differential equations in elastohydrodynamic lubrication for the solution of smooth isothermal, line contact problems. *Int. J. Numer. Meth. Eng.*, 44:pp1099–1113, 1999.

[37] T.G. Hughes, C.D. Elcoate, and H.P. Evans. Coupled solution of the elastohydrodynamic line contact problem using a differential deflection method. In *P. I. Mech. Eng. C-J. Mec.*, volume 214, pages pp585–598, 2000.

[38] C. Johnson and J. Pitkaranta. An analysis of the discontinuous Galerkin method for a scalar hyperbolic equation. *Math. Comp.*, 46(173):pp1–26, 1986.

[39] R. Lesaint and P.A. Raviart. On a finite element method for solving the neutron transport equation. *Mathematical Apects of Finite Elements in Partial Differential Equations*, pages pp89–123, 1974.

[40] H. Lu, M. Berzins, C.E. Goodyer, and P.K. Jimack. High order discontinuous Galerkin method for EHL line contact problems. *Commun. Numer. Meth. En.*, 21:pp643–650, 2005.

[41] A.A Lubrecht. *The Numerical Solution of the Elastohydrodynamically Lubricated Line and Point Contact Problem Using Multigrid Techniques*. PhD thesis, University of Twente, Endschende, The Netherlands, 1987.

[42] A.A. Lubrecht, W.E. ten Napel, and R. Bosma. Multigrid, an alternative method for calculating film thichness and pressure profiles in elastohydrodynamically lubricated line contacts. *J. Tribol-T. ASME*, 108:pp551–556, 1986.

[43] H.M. Martin. Lubrication of gear teeth. *Engineering(London)*, 102:pp199, 1916.

[44] S.H. Nguyen. A higher-order finite element scheme for incompressible lubrication calculations. *Finite. Elem Anal. Des.*, 10(4):pp307–317, 1992.

[45] J.T. Oden, I. Babuska, and C.E. Baumann. A discontinuous hp finite element method for diffusion problems. *J. Comput. Phys.*, 146:pp491–519, 1998.

[46] K.P. Oh and S.M. Rohde. Numerical solution of the point contact problem using the finite element method. *Int. J. Numer. Meth. Eng.*, 11(10):pp1507–1518, 1977.

[47] H. Okamura. A contribution to the numerical analysis of isothermal elastohydrodynamic lubrication. In D. Dowson, C. M. Taylor, M. Godet, and D. Berthe, editors, *Proc. 9th Leeds-Lyon Symp. on Tribology*, pages 313–320, 1982.

[48] G. Payre, M. D. Broissia, and J. Bazinet. An "upwind" finite element method via numerical integration. *Int. J. Numer. Meth. Eng.*, 18(3):pp381–396, 1982.

[49] T. Peterson. A note on the convergence of the discontinuous Galerkin method for a scalar hyperbolic equation. *SIAM J. Numer. Anal.*, 28:pp133–140, 1991.

[50] A.I. Petrusevich. Fundamental conclusions from the contact-hydrodynamic theory of lubrication. *Izv. Akad. Nauk. SSSR (OTN)*, 2(209), 1951.

[51] W.H. Reed and T.R. Hill. Triangular mesh methods for the neutron transport equation. Technical Report LA-UR-73-479, Los Alamos Scientific Laboratory, 1973.

[52] O. Reynolds. On the theory of lubrication and its application to Mr Beauchamp Tower's experiments, including an experimental determination of the viscosity of olive oil. *Phil. Trans. R. Soc.*, 177:pp551–556, 1886.

[53] G.R. Richter. An optimal-order error estimate for the discontinuous Galerkin method. *Math. Comput.*, 50:pp75–88, 1988.

[54] C.J.A. Roelands. *Correlational Aspects of the Viscosity-Temperature-Pressure Relationship of Lubricating Oils*. PhD thesis, Technische Hogeschool Delft, V.R.B., Groningen, The Netherlands, 1966.

[55] S.M. Rohde and K.P. Oh. A unified treatment of thick and thin film elastohydrodynamic problems by using higher order element methods. In *Proc. R. Soc. Lond. A*, volume 343, pages pp315–331, 1975.

[56] Y. Saad and M.H. Schultz. GMRES: a generalized minimal residual algorithm for solving nonsymmetric linear systems. *SIAM J. Sci. Stat. Comp.*, 7:pp856–869, 1986.

[57] T. Strouboulis and J.T. Oden. A posteriori error estimation of finite element approximations in fluid mechanics. *Comput. Method. App. M.*, 78(2):pp201–242, 1990.

[58] B. Szabo and I. Babuska. *Finite Element Analysis*. Wiley, New York, 1991.

[59] C. Taylor and J.F. O'Callaghan. A numerical solution of the elastohydrodynamic lubrication problem using finite elements. *Int. J. Mech. Sci.*, 14(4):pp229–237, 1972.

[60] C.H. Venner. *Multilevel Solution of the EHL Line and Point Contact Problems*. PhD thesis, University of Twente, Endschende, The Netherlands, 1991.

[61] C.H. Venner. Higher-order multilevel solvers for the EHL line and point contact problem. *J. Tribol-T. ASME*, 116:pp741–750, 1994.

[62] C.H. Venner and A.A. Lubrecht. Transient analysis of surface features in an EHL line contact in the case of sliding. *J. Tribol-T. ASME*, 116:pp186–193, 1994.

[63] J. Wang, S.Y. Qu, and P. Yang. Simplified multigrid technique for the numerical solution to the steady-state and transient EHL line contacts and the arbitrary entrainment EHL point contacts. *Tribol. Int.*, 34:pp191–202, 2001.

[64] S.R. Wu. A penalty formulation and numerical approximation of the Reynolds-Hertz problem of elastohydrodynamic lubrication. *Int. J. Eng. Sci.*, 24(6):pp1001–1013, 1986.

[65] P. Yang and S. Wen. A forward iterative numerical method for steady-state elastohydrodynamically lubricated contacts at high loads. *J. Tribol-T. ASME*, 108:pp411–420, 1986.

[66] P. Yang and S. Wen. *Elasto-Hydrodynamic Lubrication*. Tsinghua Press, Beijing, China, 1992.